Technische Universität Graz
Institut für Festigkeitslehre
Kopernikusgasse 24/I
8010 Graz

Benedikt Weger, BSc

Gradient-Extended Damage Mechanics at Small Deformations.

Variational Formulation and Finite Element Implementation

Masterarbeit
zur Erlangung des akademischen Grades eines
Diplom–Ingenieurs

Studienrichtung: Maschinenbau

Technische Universität Graz
Fakultät für Maschinenbau und Wirtschaftswissenschaften

Betreuer: Em.Univ.-Prof. Dipl.–Ing. Dr.techn. Christian C. Celigoj

Graz, Februar 2017

Deutsche Fassung:
Beschluss der Curricula-Kommission für Bachelor-, Master- und Diplomstudien vom 10.11.2008
Genehmigung des Senates am 1.12.2008

EIDESSTATTLICHE ERKLÄRUNG

Ich erkläre an Eides statt, dass ich die vorliegende Arbeit selbstständig verfasst, andere als die angegebenen Quellen/Hilfsmittel nicht benutzt, und die den benutzten Quellen wörtlich und inhaltlich entnommenen Stellen als solche kenntlich gemacht habe.

Graz, am …… ……..
(Unterschrift)

Englische Fassung:

STATUTORY DECLARATION

I declare that I have authored this thesis independently, that I have not used other than the declared sources / resources, and that I have explicitly marked all material which has been quoted either literally or by content from the used sources.

…… ……..
date (signature)

Abstract The loading of strain-softening materials into the inelastic regime is often associated with material instability. This results in unwanted mesh size sensitivity of the numerical solution. In order to overcome this, a non-local variational-based framework is introduced. It relies on a multi-field formulation where – in addition to the macroscopic displacements – microscopic "displacements" describing the microstructural state of the body are introduced. The non-locality of this enhanced theory is taken into account by the gradient of the microscopic "displacements". The constitutive material behavior is then determined by an energy density function and a dissipation function. Exploiting the concept of maximum dissipation, in combination with a penalty-type viscous term, enables the representation of rate-dependent material behavior. The formulation of a time-discrete variational principle yields the governing balance equations for a general gradient-type material. This variational formulation is applied to an isotropic model problem of damage mechanics. Two numerical examples comparing the classical local approach with the enhanced non-local one demonstrate that the gradient-extended model delivers results independent of the mesh size.

Kurzfassung Wenn entfestigende Materialien in den inelastischen Bereich übergehen, ist dies oft mit materieller Instabilität verbunden. Daraus resultiert eine unerwünschte Abhängigkeit der numerischen Lösung von der Feinheit des Rechennetzes. Um dieses Problem zu überwinden, wird ein nichtlokaler variationsbasierter Ansatz eingeführt, der auf einer Mehrfeldformulierung basiert. Zusätzlich zu den makroskopischen Verschiebungen werden mikroskopische "Verschiebungen" eingeführt, welche den mikrostrukturellen Zustand eines Körpers beschreiben. Der Nichtlokalität dieser erweiterten Theorie wird durch den Gradienten des mikroskopischen "Verschiebungsfeldes" Rechnung getragen. Das konstitutive Materialverhalten wird dabei mittels einer Energiedichtefunktion und einer Dissipationsfunktion festgelegt. Das Prinzip der maximalen Dissipation wird, in Kombination mit einem viskosen Strafterm, ausgenutzt, um ratenabhängiges Materialverhalten abzubilden. Die Formulierung eines zeitdiskreten Variationsprinzips liefert jene Bilanzgleichungen, die das Verhalten eines allgemeinen auf Gradientenerweiterung basierenden Materials beschreiben. Dieses Variationsprinzip wird auf ein isotropes Schädigungsmodell angewandt. Anhand von zwei numerischen Beispielen wird die klassische lokale Theorie mit der gradientenerweiterten Theorie verglichen. Es zeigt sich, dass die gradientenerweiterte Theorie von der Netzfeinheit unabhängige Ergebnisse liefert.

Contents

List of Figures

List of Tables

1. Introduction

The aim of this thesis is the description of a gradient-extended model problem of damage mechanics proposed by Welschinger [25] and its numerical treatment. In the following, a short overview of the covered topics is given.

Chapter 2 deals with the mathematical preliminaries needed for the description of variational formulations, namely the concept of the directional derivative, the Newton-Raphson method and the definition of stationary points.

In the third chapter, the fundamental physical quantities used in continuum mechanics are specified. Furthermore, the physical balance principles which must be fulfilled by any given material at all times are outlined.

In Chapter 4, the concept of solids with microstructure is introduced. In addition to the classical macroscopic displacements, microscopic displacements are introduced which describe the microstructural state of a body. The constitutive response of the material is described by two functions, where the first one represents the energy storage mechanisms, and the second one depicts the dissipative behavior of the continuum. The gradient-extended framework presented is characterized by the dependency of these two functions on the gradient of the microscopic displacements. The governing balance equations are obtained as the Euler equations of a time-discrete incremental variational principle.

The fifth chapter gives a short overview on the finite element method (FEM) and numerical integration. Moreover, an algorithm for solving the governing equations of generalized solids is described.

In the sixth chapter the stability behavior of strain-softening materials is investigated. Additionally, effects of localization and mesh size dependency of numerical solutions are examined. After a short introduction to damage mechanics in general, the variational framework described previously is applied to an isotropic gradient-type damage model. Furthermore, the discretization of the governing balance equations using a standard displacement-driven FEM approach is depicted.

Chapter 7 uses two numerical examples to compare the gradient-extended approach with a classical local one. It is shown that the proposed material model delivers solutions independent of the size of the finite element mesh.

2. Mathematical Preliminaries

This section shall give a short overview of the mathematical preliminaries needed for finding the stationary points of a highly nonlinear potential function. The main source is the book by Bonet & Wood [5, p. 47ff].

2.1. The Newton-Raphson Method and the Directional Derivative

The Newton-Raphson method (also known as Newton's method) is an iterative procedure often used for finding the root of a set of nonlinear equations

$$\boldsymbol{f}(\boldsymbol{x}) = \mathbf{0}\,, \tag{2.1}$$

where $\boldsymbol{x} = [x_1, x_2, \ldots, x_n]^T \in \mathbb{R}^n$ are the unknowns and $\boldsymbol{f} = [f_1, f_2, \ldots, f_n]^T \in \mathbb{R}^n$ are the respective function values. Starting from an initial guess $\boldsymbol{x}_0$, a linearization is performed, and the resulting linear system of equations is solved for the incremental solution update $\Delta\boldsymbol{x}_0 \coloneqq \boldsymbol{x}_1 - \boldsymbol{x}_0$. How this linearization is obtained is nontrivial and shall be shown hereafter.

Initially, an auxiliary function $\mathbf{f}(\epsilon)$ depending on a scalar parameter $\epsilon \in \mathbb{R}$ is introduced, which represents the change of $\boldsymbol{f}(\boldsymbol{x}_0)$ in an arbitrary, at the moment unknown direction $\Delta\boldsymbol{x}_0$.

$$\mathbf{f}(\epsilon) \coloneqq \boldsymbol{f}(\boldsymbol{x}_0 + \epsilon\Delta\boldsymbol{x}_0) \tag{2.2}$$

This function can be linearized as usual by truncating its Taylor series expansion after the linear term.

$$\mathbf{f}(\epsilon) = \mathbf{f}(0) + \epsilon \left.\frac{d\mathbf{f}}{d\epsilon}\right|_{\epsilon=0} + \frac{\epsilon^2}{2} \left.\frac{d^2\mathbf{f}}{d\epsilon^2}\right|_{\epsilon=0} + \ldots \tag{2.3}$$

$$\mathbf{f}(\epsilon) \approx \mathbf{f}(0) + \epsilon \left.\frac{d\mathbf{f}}{d\epsilon}\right|_{\epsilon=0} \tag{2.4}$$

Inserting the definition of $\mathbf{f}(\epsilon)$ into (2.4) leads to the linearized version of the original set of nonlinear equations $\boldsymbol{f}(\boldsymbol{x})$.

$$\boldsymbol{f}(\boldsymbol{x}_0 + \epsilon\Delta\boldsymbol{x}_0) \approx \boldsymbol{f}(\boldsymbol{x}_0) + \epsilon \left.\frac{d}{d\epsilon}\right|_{\epsilon=0} \boldsymbol{f}(\boldsymbol{x}_0 + \epsilon\Delta\boldsymbol{x}_0) \tag{2.5}$$

Since ϵ is an auxiliary parameter chosen at will, it is set to 1. The general linearization for the set of nonlinear Equations (2.1) remains as

$$\boldsymbol{f}(\boldsymbol{x}_0 + \Delta\boldsymbol{x}_0) \approx \boldsymbol{f}(\boldsymbol{x}_0) + \left.\frac{d}{d\epsilon}\right|_{\epsilon=0} \boldsymbol{f}(\boldsymbol{x}_0 + \epsilon\Delta\boldsymbol{x}_0)\,. \tag{2.6}$$

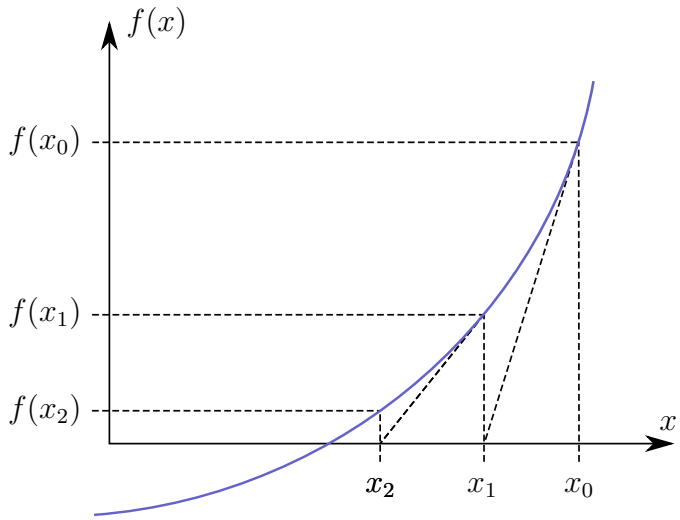

Figure 2.1.: Geometric interpretation of the one-dimensional Newton-Raphson method

The second term on the right-hand side of (2.6) is called the *directional derivative* of $\boldsymbol{f}(\boldsymbol{x})$ at $\boldsymbol{x}_0$ in the direction of $\Delta\boldsymbol{x}_0$ and is written as

$$D\boldsymbol{f}(\boldsymbol{x}_0)[\Delta\boldsymbol{x}_0] \coloneqq \left.\frac{d}{d\epsilon}\right|_{\epsilon=0} \boldsymbol{f}(\boldsymbol{x}_0 + \epsilon\Delta\boldsymbol{x}_0) \tag{2.7}$$

By applying the chain rule on (2.7), the directional derivative of a system of nonlinear equations can be displayed as

$$\begin{aligned} D\boldsymbol{f}(\boldsymbol{x}_0)[\Delta\boldsymbol{x}_0] &= \left.\frac{\partial \boldsymbol{f}}{\partial \boldsymbol{x}}\right|_{\boldsymbol{x}=\boldsymbol{x}_0} \frac{\boldsymbol{x}_0 + \epsilon\Delta\boldsymbol{x}_0}{d\epsilon} \\ &= \left.\frac{\partial \boldsymbol{f}}{\partial \boldsymbol{x}}\right|_{\boldsymbol{x}=\boldsymbol{x}_0} \Delta\boldsymbol{x}_0 \\ &= \mathbf{K}(\boldsymbol{x}_0)\Delta\boldsymbol{x}_0 \,. \end{aligned} \tag{2.8}$$

Since we want $\Delta\boldsymbol{x}_0$ to be a direction that brings us closer to the root of (2.1), a set of linear equations, from which $\Delta\boldsymbol{x}_0$ can be obtained, is constructed as follows:

$$\boldsymbol{f}(\boldsymbol{x}_0) + D\boldsymbol{f}(\boldsymbol{x}_0)[\Delta\boldsymbol{x}_0] \stackrel{!}{=} \mathbf{0} \tag{2.9}$$

Inserting (2.8) and rearranging the preceding equation yields the incremental solution update.

$$\begin{aligned} \Delta\boldsymbol{x}_0 &= -\left[\mathbf{K}(\boldsymbol{x}_0)\right]^{-1}\boldsymbol{f}(\boldsymbol{x}_0) \\ \text{or} \quad \boldsymbol{x}_1 &= \boldsymbol{x}_0 - \left[\mathbf{K}(\boldsymbol{x}_0)\right]^{-1}\boldsymbol{f}(\boldsymbol{x}_0) \end{aligned} \tag{2.10}$$

If the initial guess $\boldsymbol{x}_0$ was close enough to the exact solution, the relationship $\| \boldsymbol{f}(\boldsymbol{x}_1) \| < \| \boldsymbol{f}(\boldsymbol{x}_0) \|$ will hold, with $\| (\cdot) \|$ being an appropriate vector norm. The whole procedure is repeated iteratively, until a solution $\boldsymbol{x}_k$ is found, for which $\| \boldsymbol{f}(\boldsymbol{x}_k) \|$ falls below a desired tolerance.

In case that (2.1) consists of one function $f(x)$ only, equation (2.10), evaluated at the k-th iteration step, simplifies to

$$x_k = x_{k-1} - \frac{f(x_{k-1})}{f'(x_{k-1})}\,. \tag{2.11}$$

This one-dimensional Newton method has a very simple geometric interpretation which is illustrated in Figure 2.1.

One big advantage of the Newton-Raphson method is the fact that if $\boldsymbol{x}_0$ is chosen close enough to the exact solution, it converges quadratically. This means that for each iteration step, the difference between the root and the approximated solution is squared. There are, however, some cases in which the Newton-Raphson method fails to converge. One possibility to overcome this unpleasantness is to introduce a step length parameter α_k with $0 < \alpha_k \leq 1$ which reduces the solution increment and thereby increases the radius of convergence of the procedure. The linearization then becomes

$$\boldsymbol{f}(\boldsymbol{x}_k) + \alpha_k D\boldsymbol{f}(\boldsymbol{x}_k)[\Delta\boldsymbol{x}_k] = \boldsymbol{0}\,. \tag{2.12}$$

If this algorithm still fails to converge, it has to be combined with other root finding methods, which usually are more stable but have a slower rate of convergence. For more information on this topic, see Cosmol [8, p. 84ff].

The great power of the directional derivative lies within its universality. A more general definition than (2.7) reads

$$D\boldsymbol{\mathcal{F}}(\boldsymbol{x})[\Delta\boldsymbol{x}] \coloneqq \left.\frac{d}{d\epsilon}\right|_{\epsilon=0} \boldsymbol{\mathcal{F}}(\boldsymbol{x} + \epsilon\Delta\boldsymbol{x}) \tag{2.13}$$

where $\boldsymbol{\mathcal{F}}(\boldsymbol{x})$ can be chosen from a vast variety of mathematical entities, such as systems of nonlinear differential equations, systems of algebraic equations or geometric objects like tensors.

2.2. Stationary points and the variational principle

The directional derivative can also be used to find a stationary point of a functional.

Consider, for example, a scalar real-valued potential $\Pi(\boldsymbol{x})$ depending on a set of unknowns $\boldsymbol{x} = [x_1, x_2, \ldots, x_n]^T \in \mathbb{R}^n$. A stationary point of this potential is defined as a point

$$\{\,\boldsymbol{x}\,\} = \arg\left\{\operatorname*{stat}_{\boldsymbol{x}} \Pi(\boldsymbol{x})\right\} \coloneqq \{\,\boldsymbol{x}_S \in \mathbb{R}^n \mid D\Pi(\boldsymbol{x}_S)[\delta\boldsymbol{x}] = 0 \;\forall\; \delta\boldsymbol{x} \in \mathbb{R}^n\,\}\,, \tag{2.14}$$

which means that at this point the change of the potential in any arbitrary direction is equal to zero. Stationary points can be local maxima, local minima or saddle points. A representation of a two-dimensional potential with a local maximum can be found in Figure 2.2.

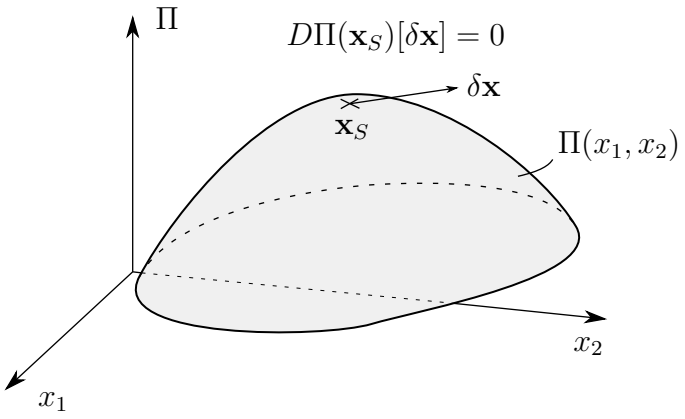

Figure 2.2.: Representation of a potential the domain of which is a subset of $\mathbb{R}^2$.

In order to obtain a stationary point, the directional derivative in direction of a set of vectors forming a base of the potential's domain has to be built. This way, a system of n equations is found which can be solved for the stationary points. The simplest way is to choose the Cartesian basis vectors of $\mathbb{R}^n$ as variational vectors. This way, the resulting system of equations to be solved takes the form

$$\frac{\partial \Pi(\boldsymbol{x})}{\partial x_i} = 0 \qquad i = 1, \ldots, n\,. \tag{2.15}$$

In case that (2.15) is a nonlinear system of equations, it can be solved with the Newton-Raphson method explained in Section 2.1.

In a more general view, the variational principle can be used to find the stationary point of a potential depending on a function $\boldsymbol{f}(\boldsymbol{x})$. The stationary points of the potential then are characterized by the equation

$$D\Pi\big(\boldsymbol{f}(\boldsymbol{x})\big)[\delta\boldsymbol{f}(\boldsymbol{x})] = 0\,. \tag{2.16}$$

3. Fundamentals of Local Continuum Mechanics at Small Deformations

The first section of this chapter mainly bases on the books by Sokolnikoff [22, p. 35ff] and Marsden & Hughes [16, p. 2f]. It introduces the fundamental quantities used for the description of continua.

Section 3.2 describes the physical balance equations of continuum mechanics. It uses Başar & Weichert [2, p. 123ff] and Welschinger [25, p. 19ff] as main references.

3.1. Fundamental Quantities

3.1.1. Geometry and Kinematics

Consider a physical body B represented by the closure of an open subset of the three-dimensional Euclidean space $\mathcal{B} \subset \mathbb{R}^3$ with piece-wise smooth boundary $\partial\mathcal{B}$. The continuum hypothesis states that B consists of an infinite amount of material points P leaving no empty space between each other, where each of these points can be represented by a position vector $\boldsymbol{x} \in \mathcal{B}$. The motion of the body is observed in a finite time interval $\mathcal{T} = [0, T] \subset \mathbb{R}_0^+$ and is described by the displacement field

$$\boldsymbol{u}(\boldsymbol{x}, t) : \begin{cases} \mathcal{B} \times \mathcal{T} & \to \mathbb{R}^3 \\ (\boldsymbol{x}, t) & \mapsto \boldsymbol{u}(\boldsymbol{x}, t) \end{cases} . \tag{3.1}$$

Along with the displacement field, the velocity and the acceleration field are defined as the first and second partial time derivative, respectively.

$$\boldsymbol{v}(\boldsymbol{x}, t) \coloneqq \frac{\partial}{\partial t}\boldsymbol{u}(\boldsymbol{x}, t) \qquad \boldsymbol{a}(\boldsymbol{x}, t) \coloneqq \frac{\partial}{\partial t}\boldsymbol{v}(\boldsymbol{x}, t) = \frac{\partial^2}{\partial t^2}\boldsymbol{u}(\boldsymbol{x}, t) \tag{3.2}$$

3.1.2. Stress and Heat Flux

Consider a solid body B and a cut section dividing it into two parts, namely part I and part II. See Figure 3.1 for a visualization of this matter. Under any arbitrary external loading, each part must remain at equilibrium. In order to preserve this balance, a traction field acting on the cut section of part I is introduced, which replaces the influence of part II. According two Newton's third law of motion, the same traction field must act

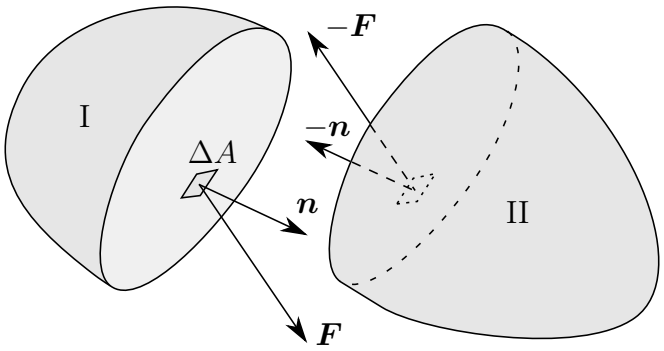

Figure 3.1.: A solid body cut in two parts along an internal cut surface. The impact of the respective other part is replaced by a traction field visualized for an arbitrary area element ΔA with normal vector $\boldsymbol{n}$

on the cut section of part II, but in opposite direction. If $\boldsymbol{F}$ is the force acting on an area element ΔA of the cut surface, the traction vector can be defined as

$$\boldsymbol{t} \coloneqq \lim_{\Delta A \to 0} \frac{\boldsymbol{F}}{\Delta A} \,. \tag{3.3}$$

Note that $\boldsymbol{t}$ does not only depend on the location of ΔA, but also its magnitude and its direction change for varying $\boldsymbol{n}$. Cauchy's theorem states that the normal vector can be mapped linearly onto the traction vector using a second order tensor called the *Cauchy Stress Tensor* $\boldsymbol{\sigma}$ such that

$$\boldsymbol{t}(\boldsymbol{x}, t, \boldsymbol{n}) = \boldsymbol{\sigma}(\boldsymbol{x}, t)\boldsymbol{n} \,. \tag{3.4}$$

In an analogous manner, consider the scalar valued heat flux q entering the body at the infinitesimal area element ΔA. Stokes' heat flux theorem postulates that the normal vector $\boldsymbol{n}$ can be mapped linearly onto q via the *Cauchy heat flux vector* $\boldsymbol{q}$ such that

$$q(\boldsymbol{x}, t, \boldsymbol{n}) = -\boldsymbol{q}(\boldsymbol{x}, t) \cdot \boldsymbol{n} \,. \tag{3.5}$$

The minus sign is introduced so that a heat flux vector pointing in the same direction as the normal vector results in heat leaving the body.

3.2. Physical Balance Principles

In this section, the physical balance principles of continuum mechanics, which must be fulfilled for any given material and at all times, are presented.

They are formulated for an arbitrary subset $\mathcal{V} \subset \mathcal{B}$ of a body B, called the control volume. The boundary of this volume $\partial\mathcal{V}$ is assumed to be piece-wise smooth. The arbitrariness of $\mathcal{V}$ allows a local formulation of the balance principles by using Gauß' theorem

$$\int_{\partial\mathcal{V}} \boldsymbol{A}\boldsymbol{n} \, dA = \int_{\mathcal{V}} \boldsymbol{\nabla}\boldsymbol{A} \, dV \,, \tag{3.6}$$

with $\boldsymbol{\nabla}$ being the nabla-operator. Note that $\boldsymbol{A}$ has to be continuously differentiable for (3.6) to be applicable.

It should also be mentioned that in a more general framework, where large deformations are taken into account, one has to differentiate between two possible control volume manifestations. The first is a time-independent spatial volume fixed in space with particles traversing its surface. The second one is a material control volume always containing the same set of particles, and therefore changing over time. In the scope of this thesis, only small deformations are considered, which allow using a time-independent control volume which contains the same particles at all times. This is important because it permits the interchange of differentiation with respect to time and integration over the volume.

3.2.1. Conservation of Mass

In a first step, the mass density ρ is defined as

$$\rho \coloneqq \lim_{\Delta V \to 0} \frac{\Delta m}{\Delta V} \,, \tag{3.7}$$

with ΔV being an arbitrary volume element and Δm the mass of the particles this very element contains. Accordingly, the mass of an infinitesimal volume element can be written as $dm = \rho \, dV$.

The principle of conservation of mass states that the mass inside the volume $\mathcal{V}$ cannot change over time

$$\frac{d}{dt} m = \frac{d}{dt} \int\limits_{\mathcal{V}} dm = \frac{d}{dt} \int\limits_{\mathcal{V}} \rho(\boldsymbol{x}, t) \, dV = 0 \,. \tag{3.8}$$

Interchanging differentiaton and integration leads to the local formulation

$$\dot{\rho}(\boldsymbol{x}, t) = 0 \,, \tag{3.9}$$

which leads to the conclusion that the mass density cannot be a function of time.

3.2.2. Balance of Linear Momentum

For a single particle contained in an infinitesimal volume element, the linear momentum is defined as $d\boldsymbol{I} \coloneqq \boldsymbol{v} \, dm$. Hence for the control volume under consideration, the linear momentum reads

$$\boldsymbol{I} = \int\limits_{\mathcal{V}} \boldsymbol{v} \, dm = \int\limits_{\mathcal{V}} \rho \boldsymbol{v} \, dV \,, \tag{3.10}$$

The balance of linear momentum states that the change with respect to time of the linear momentum of a body equals the resulting external force $\boldsymbol{F}_{ext}$ acting on that body

$$\frac{d}{dt} \boldsymbol{I} = \boldsymbol{F}_{ext} \tag{3.11}$$

with the velocity $\boldsymbol{v}$ introduced in (3.2). $\boldsymbol{F}_{ext}$ can be decomposed into two parts. The first one represents the volume force $\boldsymbol{\gamma} = \rho\boldsymbol{b}$ with $\boldsymbol{b}$ being a prescribed acceleration field. An example therefore would be the gravitational field $\boldsymbol{g}$, but also electromagnetic forces can be taken into account. The second part consists of a prescribed surface traction $\boldsymbol{t}$, which is defined in the same manner as in section 3.1.2 and can be expressed in terms of the stress tensor by using (3.4). The resulting external force then takes the form

$$\boldsymbol{F}_{ext} = \int_{\mathcal{V}} \boldsymbol{\gamma}\, dV + \int_{\partial\mathcal{V}} \boldsymbol{t}\, dA = \int_{\mathcal{V}} \boldsymbol{\gamma}\, dV + \int_{\partial\mathcal{V}} \boldsymbol{\sigma}\boldsymbol{n}\, dA\,. \tag{3.12}$$

Inserting (3.10) and (3.12) into (3.11), considering (3.9) and applying Gauß' theorem on the term describing the traction forces yields the local form of the principle of balance of linear momentum

$$\rho\boldsymbol{a} = \boldsymbol{\gamma} + \boldsymbol{\nabla}\boldsymbol{\sigma}\,. \tag{3.13}$$

3.2.3. Balance of Angular Momentum

The angular momentum with respect to a fixed coordinate system's origin o of a particle contained in an infinitesimal volume element is defined as $d\boldsymbol{D}^o := \boldsymbol{x} \times d\boldsymbol{I}$, with $\boldsymbol{x}$ being its position vector and $d\boldsymbol{I}$ its linear momentum. The angular momentum for the control volume $\mathcal{V}$ therefore reads

$$\boldsymbol{D}^o = \int_{\mathcal{V}} \boldsymbol{x} \times\, d\boldsymbol{I} = \int_{\mathcal{V}} \boldsymbol{x} \times \rho\boldsymbol{v}\, dV \tag{3.14}$$

The balance of angular momentum postulates that the change of $\boldsymbol{D}^o$ with respect to time is equal to the resulting external torque $\boldsymbol{M}^o_{ext}$ acting on the control volume with respect to o

$$\frac{d}{dt}\boldsymbol{D}^o = \boldsymbol{M}^o_{ext}\,. \tag{3.15}$$

The external torque can be decomposed into two parts in the same manner as $\boldsymbol{F}_{ext}$ in the previous section, yielding

$$\boldsymbol{M}^o_{ext} = \int_{\mathcal{V}} \boldsymbol{x} \times \boldsymbol{\gamma}\, dV + \int_{\partial\mathcal{V}} \boldsymbol{x} \times \boldsymbol{t}\, dA = \int_{\mathcal{V}} \boldsymbol{x} \times \boldsymbol{\gamma}\, dV + \int_{\partial\mathcal{V}} \boldsymbol{x} \times \boldsymbol{\sigma}\boldsymbol{n}\, dA\,. \tag{3.16}$$

By rearranging (3.15) and considering the balance of linear momentum (3.11), it can be shown that Cauchy's stress tensor is symmetric, and the local form of the balance of angular momentum then simply reads

$$\boldsymbol{\sigma} = \boldsymbol{\sigma}^T\,. \tag{3.17}$$

For an elaborate derivation of this circumstance, the reader is referred to Başar & Weichert [2, p. 128f].

3.2.4. First Law of Thermodynamics

The total energy of a single particle contained in an infinitesimal volume element is given by $d\mathcal{E}_{tot} \coloneqq e\,dm$, where e is called the specific energy per unit mass. The total energy of the control volume $\mathcal{V}$ is

$$\mathcal{E}_{tot} = \int_{\mathcal{V}} e\,dm = \int_{\mathcal{V}} \rho e\,dV\,. \tag{3.18}$$

The first law of thermodynamics states that the change of $\mathcal{E}_{tot}$ with respect to time equals the sum of the of external mechanical power $\mathcal{P}_{ext}$ and the external thermal power $\mathcal{Q}_{ext}$

$$\frac{d}{dt}\mathcal{E}_{tot} = \mathcal{P}_{ext} + \mathcal{Q}_{ext}\,. \tag{3.19}$$

The external mechanical power results from the external volume and surface forces and is written as

$$\mathcal{P}_{ext} = \int_{\mathcal{V}} \boldsymbol{v}\cdot\boldsymbol{\gamma}\,dV + \int_{\partial\mathcal{V}} \boldsymbol{v}\cdot\boldsymbol{t}\,dA = \int_{\mathcal{V}} \boldsymbol{v}\cdot\boldsymbol{\gamma}\,dV + \int_{\partial\mathcal{V}} \boldsymbol{v}\cdot\boldsymbol{\sigma}\boldsymbol{n}\,dA \tag{3.20}$$

The external thermal power $\mathcal{Q}_{ext}$ can be decomposed into two parts in a similar manner. The first part consists of the heat power produced by a *heat source per unit mass* r, which can, for example, be used for describing heat produced by chemical processes or electromagnetic induction. The second part describes the influence of heat fluxes introduced in section 3.1.2.

$$\mathcal{Q}_{ext} = \int_{\mathcal{V}} r\,dm + \int_{\partial\mathcal{V}} q\,dA = \int_{\mathcal{V}} \rho r\,dV - \int_{\partial\mathcal{V}} \boldsymbol{q}\cdot\boldsymbol{n}\,dA \tag{3.21}$$

For obtaining the local form, the following relationship is considered:

$$\int_{\partial\mathcal{V}} \boldsymbol{v}\cdot\boldsymbol{\sigma}\boldsymbol{n}\,dA = \int_{\partial\mathcal{V}} \boldsymbol{\sigma}^T\boldsymbol{v}\cdot\boldsymbol{n}\,dA = \int_{\partial\mathcal{V}} \boldsymbol{\sigma}\boldsymbol{v}\cdot\boldsymbol{n}\,dA = \int_{\mathcal{V}} \boldsymbol{\nabla}\cdot\boldsymbol{\sigma}\boldsymbol{v}\,dV \tag{3.22}$$

Inserting (3.20) and (3.21) into (3.19), applying Gauß' theorem and considering (3.22) finally yields

$$\rho\dot{e} = \boldsymbol{v}\cdot\boldsymbol{\gamma} + \rho r + \boldsymbol{\nabla}\cdot(\boldsymbol{\sigma}\boldsymbol{v} - \boldsymbol{q})\,. \tag{3.23}$$

3.2.5. Second Law of Thermodynamics

The Second law of thermodynamics takes a special position among the balance principles, because it postulates an inequality. The physical quantity of interest is the entropy, which can be loosely defined as a measure of disorganization of a system. With increasing entropy, a system comes closer to the state of thermodynamic equilibrium. The entropy of a single particle contained in an infinitesimal volume element is defined is $d\mathcal{H} = \eta\,dm$, with η being the *local entropy per unit mass*.

The entropy inequality principle postulates that the *entropy production* $\mathcal{G}$ inside the control volume $\mathcal{V}$, defined as the temporal change of entropy minus the *rate of entropy input* $\mathcal{Q}$, must be positive

$$\mathcal{G} = \frac{d}{dt}\mathcal{H} - \mathcal{Q} \geq 0\,. \tag{3.24}$$

It is explicitly recalled that the entropy of a system can decrease over time, because the entropy contained in a heat flux leaving the system can be greater than the entropy produced by internal dissipative processes.

The entropy production $\mathcal{G}$ is defined in terms of the local entropy production per unit mass γ

$$\mathcal{G} \coloneqq \int_{\mathcal{V}} \gamma \, dm = \int_{\mathcal{V}} \rho\gamma \, dV\,. \tag{3.25}$$

The rate of entropy input $\mathcal{Q}$ is defined in terms of the heat source r, the heat flux q (both introduced in the previous section) and the *total temperature* θ

$$\mathcal{Q} \coloneqq \int_{\mathcal{V}} \rho\frac{r}{\theta} \, dV + \int_{\partial\mathcal{V}} \frac{q}{\theta} \, dA\,. \tag{3.26}$$

Inserting (3.25) and (3.26) into (3.24) and applying Gauß' theorem yields the local form of the second law of thermodynamics

$$\rho\gamma = \rho\dot{\eta} - \rho\frac{r}{\theta} + \frac{1}{\theta}\boldsymbol{\nabla}\cdot\boldsymbol{q} - \frac{1}{\theta^2}\boldsymbol{q}\cdot\boldsymbol{\nabla}\theta \geq 0 \tag{3.27}$$

The previous equation is also known as the *Clausius-Duhem inequality*.

4. Continuum Mechanics of Gradient-Type Dissipative Continua at Small Deformations

This chapter summarizes the considerations of Welschinger [25, p. 25ff] for small deformations and supplements them at some points. Especially regarding Section 4.2, the contributions by Nguyen & Andrieux [19] , Biot [4] and Gurtin et al. [11] should be mentioned.

Additional to the macroscopic displacement field described in the previous chapter, global fields describing the microscopic behavior of the material are introduced. The notation used points out the duality between these *order parameter fields* and the classical macroscopic fields. In order to depict microstructural material interactions, the formulation of the constitutive response of the presented class of materials also takes into account the gradients of the order parameter fields. The radius of influence of these interactions is governed by a model parameter called the *length scale parameter* l.

4.1. Generalized Quantities of Solids with Microstructure

In order to distinguish between the macro- and the microscopic scale while attaining a compact notation, all occurring macrostructural quantities are labeled with a bar $\bar{(\cdot)}(\boldsymbol{x},t)$, while for the microstructural fields the notation $\check{(\cdot)}(\boldsymbol{x},t)$ is introduced.

4.1.1. Extended Geometric and Kinematic Setting

The geometric setup essentially stays the same as in Section 3.1.1. The body B under consideration is represented by the closure of an open subset of the three-dimensional Euclidean space $\mathcal{B} \subset \mathbb{R}^3$ with piece-wise smooth boundary $\partial\mathcal{B}$. Each point P of the body can be addressed with the position vector $\boldsymbol{x} \in \mathcal{B}$, with the observed time interval being $\mathcal{T} = [0,T] \subset \mathbb{R}_0^+$.

The displacement of each point P is described by the macroscopic deformation map

$$\bar{\boldsymbol{u}}(\boldsymbol{x},t) : \begin{cases} \mathcal{B}\times\mathcal{T} & \to \mathbb{R}^3 \\ (\boldsymbol{x},t) & \mapsto \bar{\boldsymbol{u}}(\boldsymbol{x},t) \end{cases} . \tag{4.1}$$

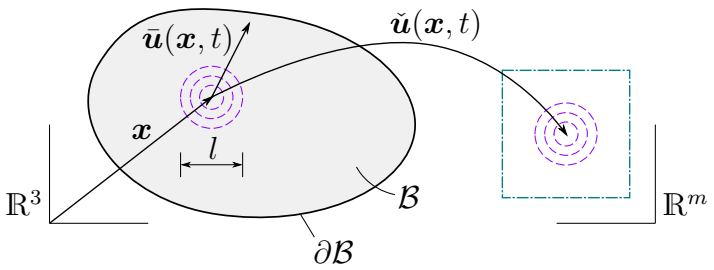

Figure 4.1.: Geometric setup of a body with microstructure

Again, the surface of the body is separated into a part $\partial\mathcal{B}_{\bar{\boldsymbol{u}}} \subset \partial\mathcal{B}$ where displacements are prescribed in the form of Dirichlet boundary conditions $\bar{\boldsymbol{u}}(\boldsymbol{x},t) = \bar{\boldsymbol{u}}_D(\boldsymbol{x},t)$, and a part $\partial\mathcal{B}_{\bar{\boldsymbol{t}}} \subset \partial\mathcal{B}$ where the macroscopic traction vector $\bar{\boldsymbol{t}}_N$ is given in the form of Neumann boundary conditions. It is important to note that in order for the boundary value problem to have a unique solution, these two types of boundary conditions must not be applied on the same part of the surface, meaning $\partial\mathcal{B}_{\bar{\boldsymbol{u}}} \cap \partial\mathcal{B}_{\bar{\boldsymbol{t}}} = \emptyset$.

Regarding the microstructure of the body, a *microscopic deformation map* $\check{\boldsymbol{u}}(\boldsymbol{x},t)$ is introduced analogously to the macroscopic one, describing the microstructural state of each point P at any given time $t \in \mathcal{T}$

$$\check{\boldsymbol{u}}(\boldsymbol{x},t) : \begin{cases} \mathcal{B}\times\mathcal{T} & \to \mathbb{R}^m \\ (\boldsymbol{x},t) & \mapsto \check{\boldsymbol{u}}(\boldsymbol{x},t) \end{cases} . \tag{4.2}$$

Note that, since the microstructural information does not live in the physical three-dimensional euclidean space $\mathbb{R}^3$, the target set of $\check{\boldsymbol{u}}(\boldsymbol{x},t)$ is an abstract euclidean space $\mathbb{R}^m$, with its dimension m being a parameter depending on the material model under consideration.

The boundary conditions are described in full analogy to the macroscopic deformation map. The surface is decomposed into a part $\partial\mathcal{B}_{\check{\boldsymbol{u}}} \subset \partial\mathcal{B}$ where Dirichlet boundary conditions $\check{\boldsymbol{u}}(\boldsymbol{x},t) = \check{\boldsymbol{u}}_D(\boldsymbol{x},t)$ are prescribed, and a part $\partial\mathcal{B}_{\check{\boldsymbol{t}}} \subset \partial\mathcal{B}$ where Neumann boundary conditions are applied via the microscopic surface traction vector $\check{\boldsymbol{t}}_N$ introduced in the next section. Again, the relationship $\partial\mathcal{B}_{\check{\boldsymbol{u}}} \cap \partial\mathcal{B}_{\check{\boldsymbol{t}}} = \emptyset$ has to hold.

Note that for the governing system of partial differential equations, Neumann type boundary conditions are natural, meaning they appear only in the assembly process. Hence, on parts of the surface where no boundary conditions are formulated explicitly, in fact zero traction vectors are prescribed.

In order to complete the geometric description of bodies with microstructure, the length scale parameter l is introduced. It will be associated with the gradient of the microscopic order parameter fields and therefore influences the exchange of microstructural information.

A visualization of the geometric setup is given in Figure 4.1.

4.1.2. Generalized Stresses and External Loading

Cauchy's theorem for macroscopic stresses (3.4) can be extended for the generalized two-scale setting under consideration. In complete analogy to the macroscopic traction vector $\bar{\boldsymbol{t}}$, a m-dimensional microscopic traction vector $\check{\boldsymbol{t}}$ is introduced.

A generalized Cauchy stress theorem is formulated, which postulates a linear relationship between the normal vector of a cut surface and the microscopic traction vector at every point of the body. This linearity is expressed via the the microscopic Cauchy stress tensor $\check{\boldsymbol{\sigma}}$, yielding

$$\check{\boldsymbol{t}} = \check{\boldsymbol{\sigma}}\boldsymbol{n}\,. \tag{4.3}$$

Furthermore, the external volumetric loading of the continuum described in Section 3.2.2 is extended by an abstract microscopic loading per unit volume $\check{\boldsymbol{\gamma}}$.

With $\check{\boldsymbol{\gamma}}$ and the microscopic traction vectors $\check{\boldsymbol{t}}_N$ prescribed on $\partial\mathcal{B}_{\check{\boldsymbol{t}}}$ at hand, the external mechanical power introduced in Equation (3.20) can be generalized, taking the form

$$\mathcal{P}_{ext} = \bar{\mathcal{P}}_{ext} + \check{\mathcal{P}}_{ext}\,, \tag{4.4}$$

with

$$\bar{\mathcal{P}}_{ext} = \int_{\mathcal{B}} \dot{\bar{\boldsymbol{u}}} \cdot \bar{\boldsymbol{\gamma}}\, dV + \int_{\partial\mathcal{B}_{\bar{\boldsymbol{t}}}} \dot{\bar{\boldsymbol{u}}} \cdot \bar{\boldsymbol{t}}_N\, dA = \int_{\mathcal{B}} \bar{\boldsymbol{v}} \cdot \bar{\boldsymbol{\gamma}}\, dV + \int_{\partial\mathcal{B}_{\bar{\boldsymbol{t}}}} \bar{\boldsymbol{v}} \cdot \bar{\boldsymbol{\sigma}}\boldsymbol{n}\, dA \tag{4.5}$$

and

$$\check{\mathcal{P}}_{ext} = \int_{\mathcal{B}} \dot{\check{\boldsymbol{u}}} \cdot \check{\boldsymbol{\gamma}}\, dV + \int_{\partial\mathcal{B}_{\check{\boldsymbol{t}}}} \dot{\check{\boldsymbol{u}}} \cdot \check{\boldsymbol{t}}_N\, dA = \int_{\mathcal{B}} \check{\boldsymbol{v}} \cdot \check{\boldsymbol{\gamma}}\, dV + \int_{\partial\mathcal{B}_{\check{\boldsymbol{t}}}} \check{\boldsymbol{v}} \cdot \check{\boldsymbol{\sigma}}\boldsymbol{n}\, dA\,. \tag{4.6}$$

4.2. Constitutive Response of Materials with Microstructure

In this section, the equations governing the behavior of materials the microstructure of which is described using order parameter fields are derived. Initially, the constitutive state of a body will be defined. Subsequently, energy storage and dissipation functionals are introduced. They will, together with the generalized external mechanical power, be used to exploit the principle of virtual power. Finally, a three-field formulation allowing the description of rate-dependent behavior will be introduced.

4.2.1. Constitutive State and Frame Invariance

As already mentioned in the introduction to this chapter, the current state of a material with microstructure can be expressed in terms of the macro- and microscopic displacements and their gradients. These quantities are summarized in the *constitutive state*

$$\mathfrak{c}_0 \coloneqq \{\bar{\boldsymbol{u}}, \boldsymbol{\nabla}\bar{\boldsymbol{u}}, \check{\boldsymbol{u}}, \boldsymbol{\nabla}\check{\boldsymbol{u}}\}\,. \tag{4.7}$$

The *principle of material frame-indifference*, introduced by Truesdell & Noll [24] and elaborately treated in Gurtin et al. [11, p.146 ff], states that the constitutive functions

defining the behavior of a material must not depend on rigid body motions imposed on the body under considerations, i.e.

$$\Phi\left(\mathfrak{c}_0^+\right) = \Phi\left(\mathfrak{c}_0\right) \tag{4.8}$$

with Φ being a constitutive function of the material model in use and $\mathfrak{c}_0^+$ being the transformed constitutive state characterized by the transformed macroscopic displacement field

$$\bar{\boldsymbol{u}}^+(\boldsymbol{x},t) = \bar{\boldsymbol{u}}(\boldsymbol{x},t) + \boldsymbol{\Omega}(t)\boldsymbol{x} + \boldsymbol{c}(t)\,. \tag{4.9}$$

The vector $\boldsymbol{c}(t)$ embodies a time-dependent translation, while the second-order tensor $\boldsymbol{\Omega}(t)$ represents a rotation of the body and hence is skew-symmetric, i.e. the relationship $\boldsymbol{\Omega} = -\boldsymbol{\Omega}^T$ holds at all times. Clearly, any constitutive function must not depend on the macroscopic displacement $\bar{\boldsymbol{u}}$, as this would violate the principle of frame-indifference.

Since the microstructural state of the body is not influenced by a rigid body motion, the microscopic displacement field, and in association its gradient, do not change

$$\check{\boldsymbol{u}}^+(\boldsymbol{x},t) = \check{\boldsymbol{u}}(\boldsymbol{x},t) \tag{4.10}$$

$$\boldsymbol{\nabla}\check{\boldsymbol{u}}^+(\boldsymbol{x},t) = \boldsymbol{\nabla}\check{\boldsymbol{u}}(\boldsymbol{x},t)\,. \tag{4.11}$$

For further investigations, the gradient of the macroscopic displacement gradient is split into a symmetric and a skew-symmetric part

$$\boldsymbol{\nabla}\bar{\boldsymbol{u}}^+(\boldsymbol{x},t) = \underbrace{\frac{1}{2}\left(\boldsymbol{\nabla}\bar{\boldsymbol{u}}^+ + \left[\boldsymbol{\nabla}\bar{\boldsymbol{u}}^+\right]^T\right)}_{:=\boldsymbol{\nabla}^S\bar{\boldsymbol{u}}^+} + \underbrace{\frac{1}{2}\left(\boldsymbol{\nabla}\bar{\boldsymbol{u}}^+ - \left[\boldsymbol{\nabla}\bar{\boldsymbol{u}}^+\right]^T\right)}_{:=\boldsymbol{\nabla}^A\bar{\boldsymbol{u}}^+}\,. \tag{4.12}$$

Inserting Equation (4.9) into the respective terms of Equation (4.12), while considering the skew symmetry of $\boldsymbol{\Omega}$, yields

$$\boldsymbol{\nabla}^S\bar{\boldsymbol{u}}^+ = \frac{1}{2}\left(\boldsymbol{\nabla}\bar{\boldsymbol{u}} + \boldsymbol{\Omega} + \left[\boldsymbol{\nabla}\bar{\boldsymbol{u}}\right]^T + \boldsymbol{\Omega}^T\right) = \boldsymbol{\nabla}^S\bar{\boldsymbol{u}} \tag{4.13}$$

$$\boldsymbol{\nabla}^A\bar{\boldsymbol{u}}^+ = \frac{1}{2}\left(\boldsymbol{\nabla}\bar{\boldsymbol{u}} + \boldsymbol{\Omega} - \left[\boldsymbol{\nabla}\bar{\boldsymbol{u}}\right]^T - \boldsymbol{\Omega}^T\right) = \boldsymbol{\nabla}^A\bar{\boldsymbol{u}} + \boldsymbol{\Omega}\,. \tag{4.14}$$

Hence, the constitutive state cannot depend on the skew symmetric macroscopic displacement gradient, but only on the symmetric one.

With the *infinitesimal strain tensor*

$$\boldsymbol{\varepsilon} \coloneqq \boldsymbol{\nabla}^S\bar{\boldsymbol{u}} = \frac{1}{2}\left(\boldsymbol{\nabla}\bar{\boldsymbol{u}} + \left[\boldsymbol{\nabla}\bar{\boldsymbol{u}}\right]^T\right) \tag{4.15}$$

at hand, the *objective constitutive state* is defined as

$$\mathfrak{c} \coloneqq \left\{\boldsymbol{\varepsilon}, \check{\boldsymbol{u}}, \boldsymbol{\nabla}\check{\boldsymbol{u}}\right\}. \tag{4.16}$$

The time derivative of a constitutive function $\Phi(\mathfrak{c})$, which will be needed later, can be obtained by applying the chain rule, yielding

$$\frac{d}{dt}\Phi(\mathfrak{c}) = \partial_{\mathfrak{c}}\Phi \cdot \dot{\mathfrak{c}} = \partial_{\boldsymbol{\varepsilon}}\Phi : \dot{\boldsymbol{\varepsilon}} + \partial_{\check{\boldsymbol{u}}}\Phi \cdot \dot{\check{\boldsymbol{u}}} + \partial_{\boldsymbol{\nabla}\check{\boldsymbol{u}}}\Phi : \boldsymbol{\nabla}\dot{\check{\boldsymbol{u}}}\,. \tag{4.17}$$

4.2.2. Energy Storage and Dissipation

Considering gradient-type dissipative solids, the constitutive behavior of a material is defined by two local, scalar functions, namely the *energy storage function* $\psi(\mathfrak{c})$ depending on the constitutive state, and the *dissipation function* $\phi(\dot{\mathfrak{c}}, \mathfrak{c})$ depending on both the constitutive state and its first time derivative.

A first step towards the derivation of the governing balance equations is the introduction of the *energy storage* E and the *dissipation* D, both being scalar, linear functionals obtained by integrating the constitutive functions ψ and ϕ over the entire body.

$$E(\bar{\boldsymbol{u}}, \check{\boldsymbol{u}}) \coloneqq \int_{\mathcal{B}} \psi(\mathfrak{c})\, dV \quad \text{and} \quad D(\dot{\bar{\boldsymbol{u}}}, \dot{\check{\boldsymbol{u}}}, \bar{\boldsymbol{u}}, \check{\boldsymbol{u}}) \coloneqq \int_{\mathcal{B}} \phi(\dot{\mathfrak{c}}, \mathfrak{c})\, dV \tag{4.18}$$

The energy stored inside the body B due to its macro- and microscopic state is represented by the energy storage E. The dissipation D represents the dissipative processes taking place inside the body, e.g. plasticity or damage, and thus not only depends on the current state of the continuum, but also the temporal change of its state.

Furthermore, the *power of energy storage mechanisms* is defined as the temporal change of the energy storage. Note that the following reformulations require the interchange of the time derivative with the volume integral and, in some places, the nabla operator. This is permitted because of the integrands continuity. Moreover, the chain rule is applied and Gauß' theorem is exploited.

$$\begin{aligned}
\mathcal{E}(\dot{\bar{\boldsymbol{u}}}, \dot{\check{\boldsymbol{u}}}, \bar{\boldsymbol{u}}, \check{\boldsymbol{u}}) \coloneqq \frac{d}{dt} E &= \int_{\mathcal{B}} \partial_{\mathfrak{c}} \psi \cdot \dot{\mathfrak{c}}\, dV \\
&= \int_{\mathcal{B}} \left(\partial_{\boldsymbol{\varepsilon}} \psi : \dot{\boldsymbol{\varepsilon}} + \partial_{\check{\boldsymbol{u}}} \psi \cdot \dot{\check{\boldsymbol{u}}} + \partial_{\boldsymbol{\nabla} \check{\boldsymbol{u}}} \psi : \boldsymbol{\nabla} \dot{\check{\boldsymbol{u}}} \right) dV \\
&= \int_{\mathcal{B}} \left(-\boldsymbol{\nabla} \partial_{\boldsymbol{\varepsilon}} \psi \cdot \dot{\bar{\boldsymbol{u}}} + \partial_{\check{\boldsymbol{u}}} \psi \cdot \dot{\check{\boldsymbol{u}}} - \boldsymbol{\nabla} \partial_{\boldsymbol{\nabla} \check{\boldsymbol{u}}} \psi \cdot \dot{\check{\boldsymbol{u}}} \right) dV \\
&\quad + \int_{\partial \mathcal{B}_{\bar{t}}} \partial_{\boldsymbol{\varepsilon}} \psi \boldsymbol{n} \cdot \dot{\bar{\boldsymbol{u}}}\, dA + \int_{\partial \mathcal{B}_{\check{t}}} \partial_{\boldsymbol{\nabla} \check{\boldsymbol{u}}} \psi \boldsymbol{n} \cdot \dot{\check{\boldsymbol{u}}}\, dA
\end{aligned} \tag{4.19}$$

In a similar way, the dissipation functional $\mathcal{D}$ is introduced. Note that it is not defined as the time derivative of $(4.18)_2$, but rather as

$$\begin{aligned}
\mathcal{D}(\dot{\bar{\boldsymbol{u}}}, \dot{\check{\boldsymbol{u}}}, \bar{\boldsymbol{u}}, \check{\boldsymbol{u}}) &\coloneqq \int_{\mathcal{B}} \partial_{\dot{\mathfrak{c}}} \phi \cdot \dot{\mathfrak{c}}\, dV \\
&= \int_{\mathcal{B}} \left(-\boldsymbol{\nabla} \partial_{\dot{\boldsymbol{\varepsilon}}} \phi \cdot \dot{\bar{\boldsymbol{u}}} + \partial_{\dot{\check{\boldsymbol{u}}}} \phi \cdot \dot{\check{\boldsymbol{u}}} - \boldsymbol{\nabla} \partial_{\boldsymbol{\nabla} \dot{\check{\boldsymbol{u}}}} \phi \cdot \dot{\check{\boldsymbol{u}}} \right) dV \\
&\quad + \int_{\partial \mathcal{B}_{\bar{t}}} \partial_{\dot{\boldsymbol{\varepsilon}}} \phi \boldsymbol{n} \cdot \dot{\bar{\boldsymbol{u}}}\, dA + \int_{\partial \mathcal{B}_{\check{t}}} \partial_{\boldsymbol{\nabla} \dot{\check{\boldsymbol{u}}}} \phi \boldsymbol{n} \cdot \dot{\check{\boldsymbol{u}}}\, dA
\end{aligned} \tag{4.20}$$

4.2.3. Requirements on the dissipation function

There are some requirements on the dissipation function, which arise from the fact that, according to the second law of thermodynamics, all dissipative processes have to irreversible. For the model in use, this results in the postulate that the dissipation functional has to be positive at all times

$$\mathcal{D} \geq 0\,. \tag{4.21}$$

A sufficient condition therefore is the positiveness of the integrand in Equation (4.20). This is guaranteed if the dissipation function ϕ satisfies the conditions

$$\phi(\mathbf{0}, \mathfrak{c}) = 0 \quad \text{and} \quad \phi(\dot{\mathfrak{c}}, \mathfrak{c}) \geq 0\,. \tag{4.22}$$

Furthermore, ϕ has to be convex with respect to the temporal change of the constitutive state

$$\alpha\phi(\dot{\mathfrak{c}}_1, \mathfrak{c}) + (1-\alpha)\phi(\dot{\mathfrak{c}}_2, \mathfrak{c}) > \phi(\alpha\dot{\mathfrak{c}}_1 + (1-\alpha)\dot{\mathfrak{c}}_2, \mathfrak{c})\,. \tag{4.23}$$

For a more elaborate discussion of this topic, the reader is referred to Miehe [17, p. 903].

4.2.4. Principle of Virtual Power

In the following, only quasistatic motions are considered. This means that inertia effects are neglected, and the time-dependency of the solution is caused by Dirichlet and Neumann boundary conditions, which may not be constant in time, only.

In this case, the principle of virtual power states that the internal power induced by energy storage and dissipation mechanisms $\mathcal{P}_{int} = \mathcal{E} + \mathcal{D}$ and the external power $\mathcal{P}_{ext}$ caused by volume forces and surface tractions must be in balance for all admissible rates of the macro- and microscopic displacements $\dot{\boldsymbol{u}}$ and $\dot{\check{\boldsymbol{u}}}$ at all times

$$0 = \mathcal{E}(\dot{\boldsymbol{u}}, \dot{\check{\boldsymbol{u}}}, \bar{\boldsymbol{u}}, \check{\boldsymbol{u}}) + \mathcal{D}(\dot{\boldsymbol{u}}, \dot{\check{\boldsymbol{u}}}, \bar{\boldsymbol{u}}, \check{\boldsymbol{u}}) - \mathcal{P}_{ext}(\dot{\boldsymbol{u}}, \dot{\check{\boldsymbol{u}}})\,. \tag{4.24}$$

Inserting Equations (4.4), (4.19) and (4.20) yields

$$\begin{aligned} 0 = &\int_{\mathcal{B}} (\boldsymbol{\nabla}\partial_{\boldsymbol{\varepsilon}}\psi + \boldsymbol{\nabla}\partial_{\dot{\boldsymbol{\varepsilon}}}\phi + \bar{\boldsymbol{\gamma}}) \cdot \dot{\boldsymbol{u}}\, dV \\ &+ \int_{\mathcal{B}} (\boldsymbol{\nabla}\partial_{\boldsymbol{\nabla}\check{\boldsymbol{u}}}\psi + \boldsymbol{\nabla}\partial_{\boldsymbol{\nabla}\dot{\check{\boldsymbol{u}}}}\phi - \partial_{\check{\boldsymbol{u}}}\psi - \partial_{\dot{\check{\boldsymbol{u}}}}\phi + \check{\boldsymbol{\gamma}}) \cdot \dot{\check{\boldsymbol{u}}}\, dV \\ &+ \int_{\mathcal{B}_{\bar{\boldsymbol{t}}}} [(\partial_{\boldsymbol{\varepsilon}}\psi + \partial_{\dot{\boldsymbol{\varepsilon}}}\phi) \cdot \boldsymbol{n} - \bar{\boldsymbol{t}}_N] \cdot \dot{\boldsymbol{u}}\, dA + \int_{\mathcal{B}_{\check{\boldsymbol{t}}}} \left[(\partial_{\boldsymbol{\nabla}\check{\boldsymbol{u}}}\psi + \partial_{\boldsymbol{\nabla}\dot{\check{\boldsymbol{u}}}}\phi) \cdot \boldsymbol{n} - \check{\boldsymbol{t}}_N\right] \cdot \dot{\check{\boldsymbol{u}}}\, dA \end{aligned} \tag{4.25}$$

In order for Equation (4.25) to have a unique solution, the displacement rates must fulfill the homogenous Dirichlet boundary conditions and come from appropriate function spaces, written as

$$\begin{aligned} \dot{\boldsymbol{u}} &\in \mathcal{W}^0_{\bar{\boldsymbol{u}}} \coloneqq \{\, \boldsymbol{w} \in \mathcal{H}^1(\mathcal{B}) \mid \boldsymbol{w} = 0 \quad \text{on} \quad \partial\mathcal{B}_{\bar{\boldsymbol{u}}} \,\} \\ \dot{\check{\boldsymbol{u}}} &\in \mathcal{W}^0_{\check{\boldsymbol{u}}} \coloneqq \{\, \boldsymbol{w} \in \mathcal{H}^1(\mathcal{B}) \mid \boldsymbol{w} = 0 \quad \text{on} \quad \partial\mathcal{B}_{\check{\boldsymbol{u}}} \,\}\,, \end{aligned} \tag{4.26}$$

Table 4.1.: Governing balance equations for a two-field formulation

Macroscopic Balance Equations:

$$\begin{aligned} \boldsymbol{\nabla}\left(\partial_{\boldsymbol{\varepsilon}}\psi + \partial_{\dot{\boldsymbol{\varepsilon}}}\phi\right) + \bar{\boldsymbol{\gamma}} &= \mathbf{0} && \text{in } \mathcal{B} \\ \bar{\boldsymbol{u}} &= \bar{\boldsymbol{u}}_D && \text{on } \partial\mathcal{B}_{\bar{\boldsymbol{u}}} \\ \left(\partial_{\boldsymbol{\varepsilon}}\psi + \partial_{\dot{\boldsymbol{\varepsilon}}}\phi\right)\cdot\boldsymbol{n} &= \bar{\boldsymbol{t}}_N && \text{on } \partial\mathcal{B}_{\bar{\boldsymbol{t}}} \end{aligned}$$

Microscopic Balance Equations:

$$\begin{aligned} \boldsymbol{\nabla}\left(\partial_{\boldsymbol{\nabla}\check{\boldsymbol{u}}}\psi + \partial_{\boldsymbol{\nabla}\dot{\check{\boldsymbol{u}}}}\phi\right) - \left(\partial_{\check{\boldsymbol{u}}}\psi + \partial_{\dot{\check{\boldsymbol{u}}}}\phi\right) + \check{\boldsymbol{\gamma}} &= \mathbf{0} && \text{in } \mathcal{B} \\ \check{\boldsymbol{u}} &= \check{\boldsymbol{u}}_D && \text{on } \partial\mathcal{B}_{\check{\boldsymbol{u}}} \\ \left(\partial_{\boldsymbol{\nabla}\check{\boldsymbol{u}}}\psi + \partial_{\boldsymbol{\nabla}\dot{\check{\boldsymbol{u}}}}\phi\right)\cdot\boldsymbol{n} &= \check{\boldsymbol{t}}_N && \text{on } \partial\mathcal{B}_{\check{\boldsymbol{t}}} \end{aligned}$$

with $\mathcal{H}^1(\mathcal{B})$ being the Sobolev space of first order on the domain $\mathcal{B} \subset \mathbb{R}^3$ of the body under consideration. The displacement functions $\bar{\boldsymbol{u}}$ and $\check{\boldsymbol{u}}$, on the other hand, come from the function spaces

$$\begin{aligned} \bar{\boldsymbol{u}} &\in \mathcal{W}_{\bar{\boldsymbol{u}}} := \{\, \boldsymbol{w} \in \mathcal{H}^1(\mathcal{B}) \mid \boldsymbol{w} = \bar{\boldsymbol{u}}_D \quad \text{on} \quad \partial\mathcal{B}_{\bar{\boldsymbol{u}}} \,\} \\ \check{\boldsymbol{u}} &\in \mathcal{W}_{\check{\boldsymbol{u}}} := \{\, \boldsymbol{w} \in \mathcal{H}^1(\mathcal{B}) \mid \boldsymbol{w} = \check{\boldsymbol{u}}_D \quad \text{on} \quad \partial\mathcal{B}_{\check{\boldsymbol{u}}} \,\}\,. \end{aligned} \tag{4.27}$$

See Appendix A for a more detailed discussion of this topic.

From equation (4.25) the governing macro- and microscopic balance equations of a two-field formulation for gradient-type dissipative solids can be read directly. They are summarized in Table 4.1.

4.2.5. Three-field Rate-Dependent Formulation of Dissipation

In order to depict rate-dependent behavior of the material, an alternative three-field formulation is introduced, which redefines the dissipation functional $\mathcal{D}$ as

$$\mathcal{D} := \int_{\mathcal{B}} \mathfrak{f}\cdot\dot{\mathfrak{c}}\, dV = \int_{\mathcal{B}} \left(\bar{\boldsymbol{\mathcal{F}}} : \dot{\boldsymbol{\varepsilon}} + \check{\boldsymbol{f}}\cdot\dot{\check{\boldsymbol{u}}} + \check{\boldsymbol{\mathcal{F}}} : \boldsymbol{\nabla}\dot{\check{\boldsymbol{u}}}\right)\, dV\,, \tag{4.28}$$

where the *thermodynamic dissipative driving forces* $\mathfrak{f}$, defined as

$$\mathfrak{f} := \left\{\bar{\boldsymbol{\mathcal{F}}}, \check{\boldsymbol{f}}, \check{\boldsymbol{\mathcal{F}}}\right\}\,, \tag{4.29}$$

have been introduced. As viewable in Equation (4.28), they are dual to the temporal change of the constitutive state $\dot{\mathfrak{c}}$. Comparing (4.28) with (4.20) indicates that $\mathfrak{f}$ can be obtained by a partial Legendre-Fenchel transformation in the rate slots.

A more practical approach, however, is the exploitation of the *concept of maximum dissipation*

$$\phi(\dot{\mathfrak{c}}, \mathfrak{c}) = \sup_{\mathfrak{f}\in\mathbb{E}} \left[\, \mathfrak{f}\cdot\dot{\mathfrak{c}} \,\right] \quad \text{with} \quad \mathbb{E} := \{\mathfrak{f} \mid \varphi(\mathfrak{f}, \mathfrak{c}) \le 0\}\,, \tag{4.30}$$

Table 4.2.: Governing balance equations for a three-field rate-dependent formulation

Macroscopic Balance Equations:

$$\begin{aligned} \boldsymbol{\nabla}\left(\partial_{\boldsymbol{\varepsilon}}\psi + \bar{\boldsymbol{\mathcal{F}}}\right) + \bar{\boldsymbol{\gamma}} &= \mathbf{0} && \text{in } \mathcal{B} \\ \bar{\boldsymbol{u}} &= \bar{\boldsymbol{u}}_D && \text{on } \partial\mathcal{B}_{\bar{\boldsymbol{u}}} \\ \left(\partial_{\boldsymbol{\varepsilon}}\psi + \bar{\boldsymbol{\mathcal{F}}}\right)\cdot\boldsymbol{n} &= \bar{\boldsymbol{t}}_N && \text{on } \partial\mathcal{B}_{\bar{\boldsymbol{t}}} \end{aligned}$$

Microscopic Balance Equations:

$$\begin{aligned} \boldsymbol{\nabla}\left(\partial_{\boldsymbol{\nabla}\check{\boldsymbol{u}}}\psi + \check{\boldsymbol{\mathcal{F}}}\right) - \left(\partial_{\check{\boldsymbol{u}}}\psi + \check{\boldsymbol{f}}\right) + \check{\boldsymbol{\gamma}} &= \mathbf{0} && \text{in } \mathcal{B} \\ \check{\boldsymbol{u}} &= \check{\boldsymbol{u}}_D && \text{on } \partial\mathcal{B}_{\check{\boldsymbol{u}}} \\ \left(\partial_{\boldsymbol{\nabla}\check{\boldsymbol{u}}}\psi + \check{\boldsymbol{\mathcal{F}}}\right)\cdot\boldsymbol{n} &= \check{\boldsymbol{t}}_N && \text{on } \partial\mathcal{B}_{\check{\boldsymbol{t}}} \end{aligned}$$

Inverse definition of the thermodynamic dissipative driving forces:

$$\begin{aligned} \tfrac{1}{\eta}\left\langle\varphi(\mathfrak{f},\mathfrak{c})\right\rangle_+ \partial_{\mathfrak{f}}\varphi &= \dot{\mathfrak{c}} && \text{in } \mathcal{B} \\ \mathfrak{c}(\boldsymbol{x}, t = t_0) &= \mathfrak{c}_0 && \text{in } \mathcal{B} \end{aligned}$$

where the thermodynamic driving forces always have to remain inside the *elastic domain* $\mathbb{E}$ defined in terms of the *yield function* $\varphi(\mathfrak{f},\mathfrak{c})$. Using this strategy, $\varphi(\mathfrak{f},\mathfrak{c})$ replaces the dissipation function $\phi(\dot{\mathfrak{c}},\mathfrak{c})$ in the description of the constitutive behavior of the material.

This formulation provides the basis for a rate-dependent approach, which does not prohibit thermodynamic driving forces outside the elastic domain, but takes them into account with a very large penalty-term. The so-called viscous regularization of the concept of maximum dissipation (4.30) then takes the form

$$\phi(\dot{\mathfrak{c}},\mathfrak{c}) = \sup_{\mathfrak{f}}\left[\mathfrak{f}\cdot\dot{\mathfrak{c}} - \frac{1}{2\eta}\left\langle\varphi(\mathfrak{f},\mathfrak{c})\right\rangle_+^2\right], \tag{4.31}$$

where the ramp function $\langle(\cdot)\rangle_+ := \frac{|(\cdot)|+(\cdot)}{2}$ has been introduced. In order for the penalty term to be of large size, the *viscosity* η introduced in (4.31) has to be very small and positive.

The regularized principle of maximum dissipation is evaluated by differentiation with respect to $\mathfrak{f}$, yielding the evolution equation for the constitutive state

$$\dot{\mathfrak{c}} = \frac{1}{\eta}\left\langle\varphi(\mathfrak{f},\mathfrak{c})\right\rangle_+ \partial_{\mathfrak{f}}\varphi(\mathfrak{f},\mathfrak{c})\,. \tag{4.32}$$

Again, the principle of virtual power can be used in the same manner as in Section 4.2.4 to obtain the nonlinear balance equations for rate-dependent gradient-type dissipative solids. The results of this procedure are summarized in Table 4.2.

Note that, because the rate-dependent balance equations contain a first order time-derivative of the constitutive state vector, an appropriate initial condition has to be provided.

4.3. Incremental Variational Principle

In this section, the incremental variational principle, which represents a method to solve the time-dependent balance equations obtained earlier, is introduced.

In a first step, the time interval under consideration will be discretized into multiple time steps. An energy potential describing the accumulated energy within one time increment, caused by internal mechanisms and external loading, will be defined. The incremental stationary principle will be applied to this potential, yielding the governing time-discrete equations for a rate-dependent three-field formulation of gradient-type dissipative solids.

4.3.1. Time Discretization

The strong form of the initial-boundary value problem formulated in Section 4.2.5 is observed in the time interval $\mathcal{T} = [t_0, t_m] \in \mathbb{R}_0^+$. A first step towards its solution is the time discretization of $\mathcal{T}$, meaning that all time-dependent quantities are evaluated at discrete points $t_0, t_1, \dots, t_n, t_{n+1}, \dots, t_m$ only. The time increment is defined as

$$\tau_{n+1} \coloneqq t_{n+1} - t_n \,. \tag{4.33}$$

In the simplest case, a constant time increment $\tau = \{\tau_n\}_{n=0,\dots,m-1}$ is chosen, which divides $\mathcal{T}$ into m equidistant time steps.

For the discretization of the occurring time derivatives, a simple backward orientated difference quotient will be used. Hence, all quantities at the current time t_n are assumed to be known and are written as

$$(\cdot)_n \coloneqq (\cdot)(\boldsymbol{x}, t_n) \,. \tag{4.34}$$

The unknown quantities at the subsequent point in time t_{n+1} are, for the sake of a simple notation, written without an index, thus yielding

$$(\cdot) \coloneqq (\cdot)_{n+1} = (\cdot)(\boldsymbol{x}, t_{n+1}) \,. \tag{4.35}$$

The time derivative of the constitutive state vector appearing in the balance equations formulated in Section 4.2.5 is approximated as

$$\dot{\mathfrak{c}} = \frac{\mathfrak{c} - \mathfrak{c}_n}{\tau} \,. \tag{4.36}$$

This notation indicates that the rate of the constitutive state is constant with respect to time within each increment.

4.3.2. Incremental Energy Storage, Dissipation and External Loading Functionals

The energy stored inside the body within one time increment can be obtained by integrating the power of energy storage mechanisms defined in Equation (4.19) over time,

using the according boundaries. This results in the incremental energy storage E^τ, which is reformulated considering Equation$(4.18)_1$

$$E^\tau(\bar{\boldsymbol{u}}, \check{\boldsymbol{u}}) \coloneqq \int_{t_n}^{t_{n+1}} \mathcal{E}\, dt = E - E_n = \int_{\mathcal{B}} \big(\psi(\mathfrak{c}) - \psi(\mathfrak{c}_n)\big)\, dV\,. \tag{4.37}$$

Note that since the integrand is continuous, the integration over time can be interchanged with the volume integral. This applies to the following integrals in this section as well.

In a similar manner, the incremental dissipation potential D^τ is defined using Equation $(4.18)_2$, yielding

$$D^\tau(\bar{\boldsymbol{u}}, \check{\boldsymbol{u}}) \coloneqq \int_{t_n}^{t_{n+1}} D\, dt = \int_{\mathcal{B}} \tau\phi\left({}^{(\mathfrak{c}-\mathfrak{c}_n)}/_{\tau}, \mathfrak{c}_n\right)\, dV \tag{4.38}$$

for a canonical two-field setting.

Using the notation introduced in Section 4.2.5, an alternative extended dissipation potential $D^{*\tau}$ can be defined as

$$D_\eta^{*\tau}(\bar{\boldsymbol{u}}, \check{\boldsymbol{u}}) \coloneqq \int_{\mathcal{B}} \left[\mathfrak{f}\cdot(\mathfrak{c}-\mathfrak{c}_n) - \frac{\tau}{2\eta}\left\langle\varphi(\mathfrak{f}, \mathfrak{c}_n)\right\rangle_+^2\right] dV\,, \tag{4.39}$$

enabling the treatment of rate-dependent behavior.

The energy brought into the system by the external loading described in Section 4.1.2 within one time increment can be obtained by simply integrating the external mechanical power over time, again using the according boundaries

$$\begin{aligned} W^\tau(\bar{\boldsymbol{u}}, \check{\boldsymbol{u}}) \coloneqq \int_{t_n}^{t_{n+1}} \mathcal{P}_{ext}\, dt = &\int_{\mathcal{B}} \bar{\boldsymbol{\gamma}}\cdot(\bar{\boldsymbol{u}}-\bar{\boldsymbol{u}}_n)\, dV + \int_{\partial\mathcal{B}_{\bar{\boldsymbol{t}}}} \bar{\boldsymbol{t}}_N\cdot(\bar{\boldsymbol{u}}-\bar{\boldsymbol{u}}_n)\, dA \\ &+ \int_{\mathcal{B}} \check{\boldsymbol{\gamma}}\cdot(\check{\boldsymbol{u}}-\check{\boldsymbol{u}}_n)\, dV + \int_{\partial\mathcal{B}_{\check{\boldsymbol{t}}}} \check{\boldsymbol{t}}_N\cdot(\check{\boldsymbol{u}}-\check{\boldsymbol{u}}_n)\, dA\,. \end{aligned} \tag{4.40}$$

In order to obtain a more compact notation, the generalized deformation vector

$$\mathfrak{u} \coloneqq \{\bar{\boldsymbol{u}}, \check{\boldsymbol{u}}\} \tag{4.41}$$

is introduced, which contains both the macroscopic and the microscopic deformation maps. Additionally, the generalized volume force vector

$$\mathfrak{g} \coloneqq \{\bar{\boldsymbol{\gamma}}, \check{\boldsymbol{\gamma}}\} \tag{4.42}$$

is defined as the union of the macroscopic and the microscopic forces per unit volume. Finally, the generalized surface traction vector

$$\mathfrak{t}_N \coloneqq \{\bar{\boldsymbol{t}}_N, \check{\boldsymbol{t}}_N\} \tag{4.43}$$

holds the macro- and microscopic surface traction vectors defined on the respective parts of the surface on which Neumann boundary conditions are applied. These subsets of the boundary are summarized as $\partial\mathcal{B}_{\mathfrak{t}} \coloneqq \{\partial\mathcal{B}_{\bar{\boldsymbol{t}}_N}, \partial\mathcal{B}_{\check{\boldsymbol{t}}_N}\}$.

With these definitions at hand, the incremental external work (4.40) can be rewritten as

$$W^{\tau}(\bar{\boldsymbol{u}}, \check{\boldsymbol{u}}) = \int_{\mathcal{B}} \mathfrak{g} \cdot (\mathfrak{u} - \mathfrak{u}_N)\, dV + \int_{\partial\mathcal{B}_{\mathfrak{t}}} \mathfrak{t} \cdot (\mathfrak{u} - \mathfrak{u}_N)\, dA \tag{4.44}$$

4.3.3. Rate-Dependent Incremental Variational Principle

The governing quantity for a variational based formulation of rate-dependent gradient-type dissipative solids is the *extended incremental potential* $\Pi_{\eta}^{*\tau}$. It subsumes the incremental energy storage, the extended dissipation potential and the incremental external work, all introduced in the previous section. Its definition reads

$$\Pi_{\eta}^{*\tau}(\bar{\boldsymbol{u}}, \check{\boldsymbol{u}}, \mathfrak{f}) \coloneqq E^{\tau}(\bar{\boldsymbol{u}}, \check{\boldsymbol{u}}) + D^{*\tau}(\bar{\boldsymbol{u}}, \check{\boldsymbol{u}}, \mathfrak{f}) - W^{\tau}(\bar{\boldsymbol{u}}, \check{\boldsymbol{u}})\,. \tag{4.45}$$

The generalized deformation vector introduced in Equation (4.41) and the constitutive state are complemented by the thermodynamic driving forces $\mathfrak{f}$, yielding the extended deformation vector $\mathfrak{u}^*$ and extended constitutive state $\mathfrak{c}^*$

$$\mathfrak{u}^* \coloneqq \{\bar{\boldsymbol{u}}, \check{\boldsymbol{u}}, \mathfrak{f}\} \quad \mathfrak{c}^* \coloneqq \{\boldsymbol{\varepsilon}, \check{\boldsymbol{u}}, \boldsymbol{\nabla}\check{\boldsymbol{u}}, \mathfrak{f}\}\,. \tag{4.46}$$

As a final step towards a compact and clear notation, the *extended incremental internal work density* is introduced as

$$\pi_{\eta}^{*\tau}(\mathfrak{c}^*, \mathfrak{c}_n^*) \coloneqq \psi(\mathfrak{c}) - \psi(\mathfrak{c}_n) + \mathfrak{f} \cdot (\mathfrak{c} - \mathfrak{c}_n) - \frac{\tau}{2\eta} \left\langle \varphi(\mathfrak{f}, \mathfrak{c}_n) \right\rangle_+^2 . \tag{4.47}$$

The incremental potential can then be rewritten by inserting Equations (4.37), (4.39) and (4.44) into (4.45), yielding its final form

$$\Pi_{\eta}^{*\tau}(\mathfrak{u}^*) = \int_{\mathcal{B}} \left[\pi_{\eta}^{*\tau}(\mathfrak{c}^*, \mathfrak{c}_n^*) - \mathfrak{g} \cdot (\mathfrak{u} - \mathfrak{u}_n)\right] dV - \int_{\partial\mathcal{B}_{\mathfrak{t}}} \mathfrak{t}_N \cdot (\mathfrak{u} - \mathfrak{u}_n)\, dA\,. \tag{4.48}$$

The *extended rate-dependent incremental stationary principle* states that the unknown generalized deformation vector can be obtained by solving the saddle point problem

$$\{\bar{\boldsymbol{u}}, \check{\boldsymbol{u}}, \mathfrak{f}\} = \arg \left\{ \inf_{\bar{\boldsymbol{u}}} \inf_{\check{\boldsymbol{u}}} \sup_{\mathfrak{f}} \Pi_{\eta}^{*\tau}(\bar{\boldsymbol{u}}, \check{\boldsymbol{u}}\, \mathfrak{f}) \right\} . \tag{4.49}$$

As described in Section 2.2, a saddle point is a type of stationary point, and therefore can be obtained by setting the directional derivative with respect to a set of test functions $\delta\mathfrak{u}^*$ to zero

$$D\Pi_{\eta}^{*\tau}[\delta\mathfrak{u}^*] = D\Pi_{\eta}^{*\tau}[\delta\bar{\boldsymbol{u}}] + D\Pi_{\eta}^{*\tau}[\delta\check{\boldsymbol{u}}] + D\Pi_{\eta}^{*\tau}[\delta\mathfrak{f}] = 0\,, \tag{4.50}$$

with the test functions $\delta\bar{\boldsymbol{u}} \in \mathcal{W}^0_{\bar{\boldsymbol{u}}}$, $\delta\check{\boldsymbol{u}} \in \mathcal{W}^0_{\check{\boldsymbol{u}}}$ and $\delta\mathfrak{f} \in \mathcal{L}_2$ coming from the function spaces introduced in Equation (4.26) and closer examined in Appendix A. The solution fields $\bar{\boldsymbol{u}} \in \mathcal{W}_{\bar{\boldsymbol{u}}}$, $\check{\boldsymbol{u}} \in \mathcal{W}_{\check{\boldsymbol{u}}}$ and $\delta\mathfrak{f} \in \mathcal{L}_2$, on the other hand, come from the function spaces introduced in (4.27).

The individual terms of Equation (4.50) can be identified by inserting (4.47) into (4.48) and building the respective directional derivatives, yielding

$$\begin{aligned}
D\Pi^{*\tau}_\eta[\delta\bar{\boldsymbol{u}}] &= \int_{\mathcal{B}} \left[\left(\partial_{\boldsymbol{\varepsilon}}\psi + \bar{\boldsymbol{\mathcal{F}}}\right) : \delta\boldsymbol{\varepsilon} - \bar{\boldsymbol{\gamma}} \cdot \delta\bar{\boldsymbol{u}}\right] dV - \int_{\partial\mathcal{B}_{\bar{\boldsymbol{t}}}} \bar{\boldsymbol{t}}_N \cdot \delta\bar{\boldsymbol{u}}\, dA \\
D\Pi^{*\tau}_\eta[\delta\check{\boldsymbol{u}}] &= \int_{\mathcal{B}} \left[\left(\partial_{\boldsymbol{\nabla}\check{\boldsymbol{u}}}\psi + \check{\boldsymbol{\mathcal{F}}}\right) : \boldsymbol{\nabla}\delta\check{\boldsymbol{u}} + \left(\partial_{\check{\boldsymbol{u}}}\psi + \check{\boldsymbol{f}} - \check{\boldsymbol{\gamma}}\right) \cdot \delta\bar{\boldsymbol{u}}\right] dV - \int_{\partial\mathcal{B}_{\check{\boldsymbol{t}}}} \check{\boldsymbol{t}}_N \cdot \delta\check{\boldsymbol{u}}\, dA \\
D\Pi^{*\tau}_\eta[\delta\mathfrak{f}] &= \int_{\mathcal{B}} \left[\mathfrak{c} - \mathfrak{c}_n - \frac{\tau}{\eta} \langle\varphi\rangle_+ \partial_{\mathfrak{f}}\varphi\right] \cdot \delta\mathfrak{f}\, dV\,.
\end{aligned} \tag{4.51}$$

The Euler equations which can be gained from this set of equations are the same as the ones in Table 4.2, except that the rate of the constitutive state has been replaced by its approximation given in Equation (4.36). This strongly substantiates the procedure introduced in this section.

5. Finite Element Method

In general, the partial differential equations describing physical phenomena can only be solved analytically, if severe simplifications are applied during the modeling process. An analytic solution of problems in structural mechanics, for example, may be obtained only if both the material model under consideration and the boundary conditions do not exceed a certain degree of complexity.

In order to solve more complicate problems, numerical techniques, which deliver approximated solutions, have been developed. The standard method, at least regarding the mechanics of solids, is the *finite element method*.

While Section 5.1 gives a general overview of the finite element method, Section 5.2 deals with its application to the variational formulation describing the behavior of gradient-type dissipative continua introduced in the previous chapter.

5.1. General Description

In this section, the finite element method is outlined on a general basis. The main source for the first four subsections are the books by Hughes [13] and Bathe [3]. Section 5.1.5 mainly basis on Zienkiewicz & Taylor [26, p.208ff], and Section 5.1.6 uses Szabò & Babuška [23, p.321ff] as main reference.

5.1.1. Discretization

The first step of the procedure is the discretization of the domain $\mathcal{B}$ under consideration. The discretized domain $\mathcal{B}^h$, which is parametrized by a characteristic length scale h, is called *mesh*. $\mathcal{B}^h$ is represented by an assemblage of subdomains $\mathcal{B}^e$ called *elements*, which are interconnected at their nodal points. This assembly process can be written as

$$\mathcal{B}^h = \mathop{\mathsf{A}}_{e=1}^{n_{el}} \mathcal{B}^e \,, \tag{5.1}$$

and is represented by the symbol $\mathsf{A}_{e=1}^{n_{el}}$, with n_{el} being the total number of elements the mesh consists of. In two dimensions, the elements can be of triangular or quadrilateral shape. There exist some requirements on the discretization, which are beyond the scope of this thesis and are explained extensively in the literature. See, for example, Braess [6, p. 61] for a more detailed explanation. A visualization of two possible two-dimensional meshes using quadrilaterals and triangles is given in Figure 5.1. Standard elements in three dimensions are, among others, tetrahedra and hexahedra. Along

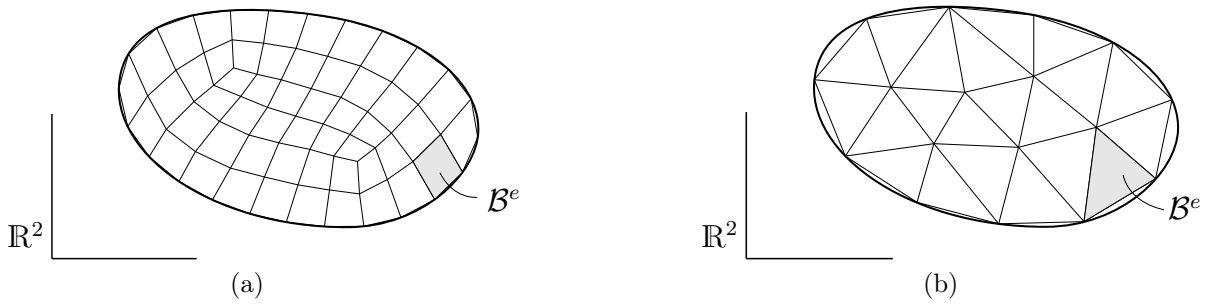

Figure 5.1.: Discretization of a two-dimensional continuous domain using (a) quadrilateral, and (b) triangular finite elements.

with the discretization of the domain, finite-dimensional approximations of the function spaces $\mathcal{W}$ and $\mathcal{W}_0$ defined in Section 4.2.4 are introduced as

$$\begin{aligned} \mathcal{W}^h &\subset \mathcal{W} \\ \mathcal{W}_0^h &\subset \mathcal{W}_0 \,. \end{aligned} \tag{5.2}$$

This notation indicates that $\mathcal{W}^h$ and $\mathcal{W}_0^h$ are subsets of the function spaces they approximate. $\mathcal{W}^h$ consists of all linear combinations of a set of given functions $\widetilde{N}_i : \mathcal{B} \mapsto \mathbb{R}$, where $i = 1, \ldots, N$.

Hence, each function $\boldsymbol{u}^h \in \mathcal{W}^h$ can be written as

$$\boldsymbol{u}^h(\boldsymbol{x}, t) = \sum_{i=1}^{N} \widetilde{N}_i(\boldsymbol{x}) \hat{\boldsymbol{u}}_i(t), \tag{5.3}$$

with $\hat{\boldsymbol{u}}_i$ being the function value of $\boldsymbol{u}^h$ at the i^{th} node of the mesh. The functions $\{\widetilde{N}_i\}_{i=1,\ldots,N}$ are called *shape*, *basis* or *interpolation functions*. It is obvious that the accuracy of a numerical solution highly depends on choosing a function space $\mathcal{W}^h$ which is able to approximate the exact solution $\boldsymbol{u}$ well.

The most widely used class of shape functions are polynomials. It has been shown that defining shape functions on a global level and trying to achieve high accuracy by increasing their polynomial degree has some severe drawbacks. Instead, piecewise polynomials are used which are nonzero only in the domain of one element. The required accuracy is achieved by choosing a sufficiently fine discretization $\mathcal{B}^h$ of the domain under consideration.

5.1.2. Reference Element and Mapping

If an element-wise interpolation was performed directly, the shape functions would have to be defined on each cell of the mesh. Additionally, the quadrature points needed for the numerical integration of the integrals appearing in the variational formulation would have to be determined on each element, which can be tedious and error prone.

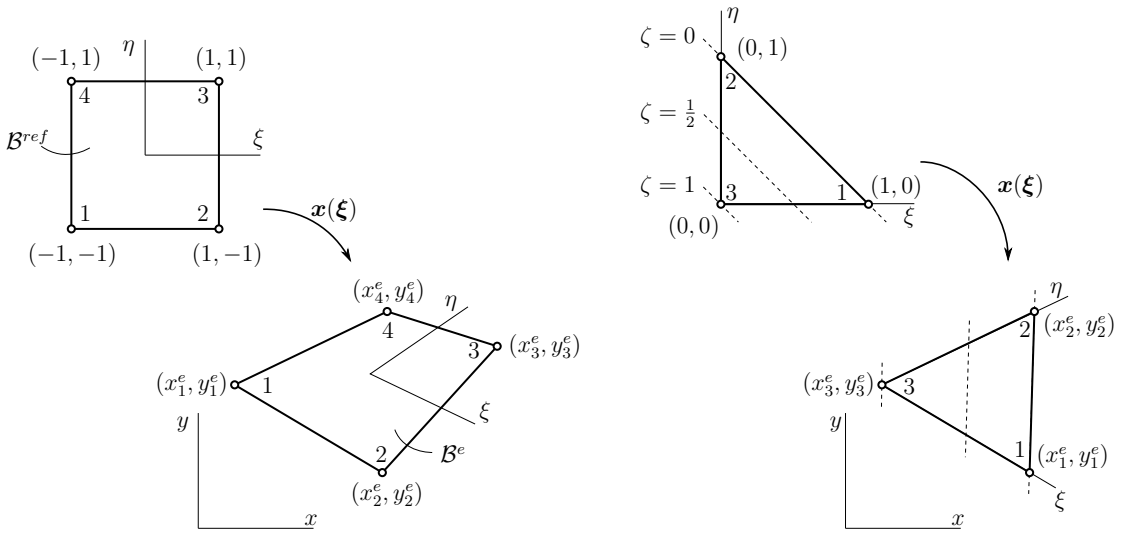

Figure 5.2.: Subfigure (a) shows the reference cell for a discretization using quadrilaterals. The mapping onto the real cell is performed via a coordinate transformation. For the triangular reference cell shown in Subfigure (b), an additional coordinate $\zeta := 1 - \xi - \eta$ is introduced.

A more convenient approach is to define all quantities of interest on a *reference element* using a set of new coordinates $\boldsymbol{\xi}$, called the *natural coordinates*. The domain taken by this element is denoted by $\mathcal{B}^{ref}$. All quantities on the real cell can be obtained by mapping them to the previously used coordinates $\boldsymbol{x}$, i.e. carrying out a coordinate transformation of the form

$$\boldsymbol{x}(\boldsymbol{\xi}) = \sum_{i=1}^{n} N_i(\boldsymbol{\xi}) \boldsymbol{x}_i^e \,, \tag{5.4}$$

with n being the number of nodes of the element and $\boldsymbol{x}_i^e$ the global nodal coordinates. The reference cell and the mapping of two-dimensional quadrilateral and triangular elements are depicted in Figure 5.2.

As already mentioned in the previous section, the solution variable $\boldsymbol{u}$ is discretized on element level too. If the shape functions are the same as for $\boldsymbol{x}$ in Equation (5.4), the finite element is called *isoparametric*, and the interpolation reads

$$\boldsymbol{u}(\boldsymbol{\xi}) = \sum_{i=1}^{n} N_i(\boldsymbol{\xi}) \hat{\boldsymbol{u}}_i^e \,. \tag{5.5}$$

In the following, standard shape functions for isoparametric elements shall be discussed.

5.1.3. Standard Shape Functions

Finite element shape functions are constructed in such a way that the approximate solution converges to the exact solution as the mesh is refined. The basic convergence criteria which are *sufficient* for such a behavior are that the shape functions be

i) continuously differentiable on each element interior $\mathcal{B}^e$,

ii) continuous across each element boundary $\partial\mathcal{B}^e$, and

iii) complete.

According to HUGHES [13, p. 111], a set of complete shape functions is defined as follows:

> Completeness requires that the element interpolation function is capable of exactly representing an arbitrary linear polynomial when the nodal degrees of freedom are assigned values in accordance with it.

A more elaborate discussion of this difficult to interpret definition can be found in the cited book.

Note that, on the one hand, the formulated conditions are not necessary for convergence, and therefore finite elements can be constructed which do not fulfill them, but still exhibit convergent behavior.

On the other hand, there exist elements which have stronger continuity requirements due to the fact that derivatives of higher order than one appear in integrands of the variational formulation, e.g. the Bernoulli-Euler beam theory. In general, if the variational formulation involves derivatives of order m, conditions i) and ii) can be reformulated such that the shape functions shall be m–times continuously differentiable in $\mathcal{B}^e$ and $(m-1)$–times continuously differentiable across each element boundary $\partial\mathcal{B}^e$. A finite element which fulfills these conditions is called *conforming* or *compatible*.

Lagrange Polynomials

A desirable property of shape functions is that their value is zero at all nodes of the cell but one, and the value at the remaining node is one. This can be written as

$$N_i(\boldsymbol{\xi}_j) = \delta_{ij} = \begin{cases} 1 & | \quad i = j \\ 0 & | \quad i \neq j \end{cases} \quad i, j = 1, \ldots, n\,. \tag{5.6}$$

In one dimension, this behavior is achieved by the *Lagrange polynomials* defined as

$$l_i^{n-1} := \prod_{\substack{j=1 \\ j\neq i}}^{n} \frac{(\xi - \xi_j)}{(\xi_i - \xi_j)} = \frac{(\xi - \xi_1)\cdots(\xi - \xi_{i-1})(\xi - \xi_{i+1})\cdots(\xi - \xi_n)}{(\xi_i - \xi_1)\cdots(\xi_i - \xi_{i-1})(\xi_i - \xi_{i+1})\cdots(\xi_i - \xi_n)}\,. \tag{5.7}$$

The Lagrange polynomials, interpreted as shape functions of an one-dimensional element with two, three and four equally spaced nodes are shown in Figure 5.3.

Fulfilling all three convergence criteria of finite element shape functions and being easy to construct, Lagrange polynomials form the basis for a lot of two- and three-dimensional interpolation functions, some of which shall be outlined hereafter.

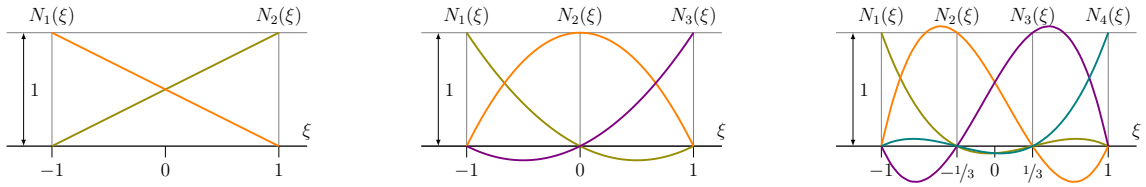

Figure 5.3.: Lagrange polynomials interpreted as shape functions for a one-dimensional element with (a) two, (b) three and (c) four equally spaced nodes.

Quadrilateral Lagrange Elements

The shape functions of quadrilateral Lagrange elements of order m with $n = m^2$ nodes are formed by the tensorial product of the according Lagrange polynomials, yielding

$$N_i(\xi, \eta) = l_a^m(\xi) l_b^m(\eta)\,, \tag{5.8}$$

with a and b being the local node indices in direction of the ξ and η axis, respectively. The relationship between the indices i, a and b has to be given in an adjacency table. In Figure 5.4a, a table is given exemplarily for a quadrilateral Lagrange element of order two.

The pascal triangle showing the monomials forming the basis of quadrilateral Lagrange elements of arbitrary order m is depicted in Figure 5.5a.

Triangular Elements

The reference element shown in Figure 5.2b is used to describe the shape functions of triangular finite elements. In addition to the natural coordinates ξ and η used so far, a third parameter ζ defined as

$$\zeta(\xi, \eta) := 1 - \xi - \eta \tag{5.9}$$

is introduced. ξ, η and ζ are called the *triangular coordinates*. They allow a general formulation of shape functions of arbitrary order basing on Lagrange polynomials. These interpolation functions are given as

$$N_i(\xi, \eta, \zeta) = T_a(\xi) T_b(\eta) T_c(\zeta)\,, \tag{5.10}$$

with

$$T_a(\xi) = \begin{cases} l_a^{a-1}\left(\frac{2\xi}{\xi_a - 1}\right) & | \quad a \neq 1 \\ 1 & | \quad a = 1\,. \end{cases} \tag{5.11}$$

$T_b(\eta)$ and $T_c(\zeta)$ are defined analogously. Again, the indices a, b and c are the local node indices in direction of ξ, η and ζ, respectively. As with quadrilateral Lagrange elements, an adjacency table, which gives the relationship between i, a, b and c has to be provided. This is done exemplarily for a triangular Lagrange element of order two in Figure 5.4b.

Figure 5.5b shows the monomials forming the basis of triangular Lagrange elements of arbitrary order m.

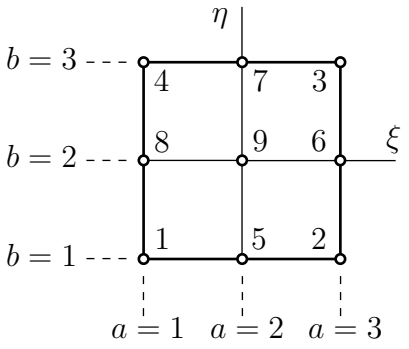

$\boldsymbol{i}$	1	2	3	4	5	6	7	8	9
$\boldsymbol{a}$	1	3	3	1	2	3	2	1	2
$\boldsymbol{b}$	1	1	3	3	1	2	3	2	2

(a)

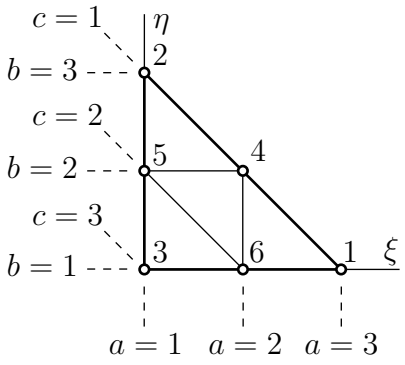

$\boldsymbol{i}$	1	2	3	4	5	6
$\boldsymbol{a}$	3	1	1	2	1	2
$\boldsymbol{b}$	1	3	1	2	2	1
$\boldsymbol{c}$	1	1	3	1	2	2

(b)

Figure 5.4.: The relationship between the indices a, b and c and the local node index is given exemplarily in adjacency tables for a second order (a) nine node quadrilateral, (b) six node triangular Lagrange element.

5.1.4. Further Finite Element Descriptions

The standard two-dimensional elements presented in the previous section can easily be extended by adding nodes both inside the reference element as well as on its boundary using Lagrange polynomials. How this is done is explained extensively in the literature. See, for example, Hughes [13, p.132ff]

Until now, only two-dimensional finite elements have been considered. Three-dimensional ones can be described analogously, which is discussed elaborately in a lot of books on finite elements.

Furthermore, some types of non-standard finite elements make direct use of the variational problems physical context. Their formulation usually is very application-specific and hard to outline in a general way. An example would be the structural elements used for the treatment of beams, plates and shells described by Bathe [3]

5.1.5. Differentiation and Integration Mapping

The following section deals with the mapping from the reference cell onto the real cell. All relationships are given for the general three-dimensional case, using the set of local

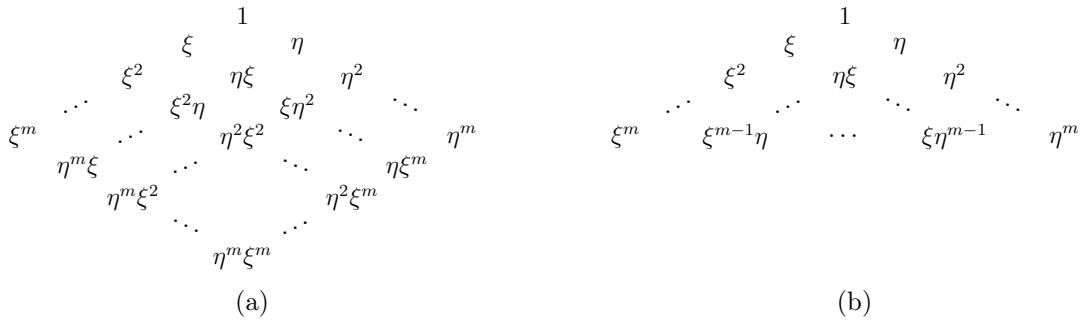

Figure 5.5.: Pascal triangles showing the monomials forming the basis for (a) quadrilateral, (b) triangular Lagrange elements

coordinates $\{\xi, \eta, \zeta\}$, and the set of global coordinates $\{x, y, z\}$. All considerations can be adopted to lower dimensions easily.

Jacobian Matrix

The mapping process actually is nothing else than a coordinate transformation, the mathematical representation of which is denoted in Equation (5.4). For the variational formulation, derivatives of the interpolation functions are needed. By applying the chain rule, these quantities can be obtained as

$$\begin{pmatrix} \frac{\partial N_i}{\partial \xi} \\ \frac{\partial N_i}{\partial \eta} \\ \frac{\partial N_i}{\partial \zeta} \end{pmatrix} = \underbrace{\begin{pmatrix} \frac{\partial x}{\partial \xi} & \frac{\partial y}{\partial \xi} & \frac{\partial z}{\partial \xi} \\ \frac{\partial x}{\partial \eta} & \frac{\partial y}{\partial \eta} & \frac{\partial z}{\partial \eta} \\ \frac{\partial x}{\partial \zeta} & \frac{\partial y}{\partial \zeta} & \frac{\partial z}{\partial \zeta} \end{pmatrix}}_{\boldsymbol{J}} \begin{pmatrix} \frac{\partial N_i}{\partial x} \\ \frac{\partial N_i}{\partial y} \\ \frac{\partial N_i}{\partial z} \end{pmatrix}, \tag{5.12}$$

where the *Jacobian matrix* $\boldsymbol{J}$ has been introduced. Since the shape functions are defined on the reference cell, the left-hand side of the above equation can be considered known. The Jacobian matrix can be found with help of the transformation rule given in Equation (5.4).

Hence, the global derivatives of the interpolation functions can be calculated as

$$\begin{pmatrix} \frac{\partial N_i}{\partial x} \\ \frac{\partial N_i}{\partial y} \\ \frac{\partial N_i}{\partial z} \end{pmatrix} = \boldsymbol{J}^{-1} \begin{pmatrix} \frac{\partial N_i}{\partial \xi} \\ \frac{\partial N_i}{\partial \eta} \\ \frac{\partial N_i}{\partial \zeta} \end{pmatrix}. \tag{5.13}$$

Volume and Surface Integration

As already mentioned, evaluating the integrals occurring in the variational formulation on the reference element has some advantages.

The integral of an arbitrary function $f(x, y, z)$ over the domain of any real cell can be transformed onto the reference cell by exploiting the multi-dimensional substitution rule, yielding

$$\int_{\mathcal{B}^e} f(x,y,z)\,dx\,dy\,dz = \int_{\mathcal{B}^{ref}} f\big(x(\xi,\eta,\zeta), y(\xi,\eta,\zeta), z(\xi,\eta,\zeta)\big)\,\det\big(\boldsymbol{J}(\xi,\eta,\zeta)\big)\,d\xi\,d\eta\,d\zeta \tag{5.14}$$

$$\int_{\mathcal{B}^e} f(\boldsymbol{x})\,dx\,dy\,dz = \int_{\mathcal{B}^{ref}} f\big(\boldsymbol{x}(\boldsymbol{\xi})\big)\,\det\big(\boldsymbol{J}(\boldsymbol{\xi})\big)\,d\xi\,d\eta\,d\zeta \tag{5.15}$$

A proof of this rule can be found in numerous standard textbooks on analysis, for example the book by Burg et al. [7, p.545].

Surface integrals are transformed in a similar manner. Generally, one of the local coordinates is constant on the surface of an element. Without loss of generality, in the following this coordinate is assumed to be ζ. The infinitesimal area element dA expressed in terms of the global coordinates, interpreted as a vector coincident with the surfaces normal vector $\boldsymbol{n}$, can then be written as

$$d\boldsymbol{A} = \boldsymbol{n}\,dA = \begin{pmatrix} \frac{\partial x}{\partial \xi} \\ \frac{\partial y}{\partial \xi} \\ \frac{\partial z}{\partial \xi} \end{pmatrix} \times \begin{pmatrix} \frac{\partial x}{\partial \eta} \\ \frac{\partial y}{\partial \eta} \\ \frac{\partial z}{\partial \eta} \end{pmatrix} d\xi\,d\eta\,. \tag{5.16}$$

The integration limit of any surface integral has to be changed from $\partial\mathcal{B}^e$ to $\partial\mathcal{B}^{ref}$.

5.1.6. Numerical Integration

In general, the integrals occurring in the variational formulation are computed numerically on the reference cell. An example for a numerical integration scheme is the Newton-Cotes quadrature. It interpolates the integrand using Lagrange polynomials at (n+1) equidistant quadrature points ξ_0, ξ_1,..., ξ_n. It integrates polynomials of degree up to n exactly. For a large n, however, this procedure can suffer from instabilities, known as Runge's phenomenon. A more elaborate approach is the *Gauß quadrature*. It delivers decent results for most applications and shall be shortly described in the following.

Gauß Quadrature in One Dimension

The integration of an arbitrary function $f(\xi)$ over the domain of the one-dimensional reference element is evaluated as the sum

$$\int_{-1}^{1} f(\xi)\,d\xi = \sum_{i=1}^{n} w_i f(\xi_i) + R_n\,, \tag{5.17}$$

where w_i are the integration weights, ξ_i are the quadrature points and R_n is the error term. The node ξ_i is the i^{th} zero of the Legendre polynomial P_n. These type of

Table 5.1.: Integration weights and node positions for Gauß quadrature with n integration nodes.

n	$\pm\xi_i$	w_i
1	0.000 000 000 000 000	2.000 000 000 000 000
2	0.577 350 269 189 626	1.000 000 000 000 000
3	0.000 000 000 000 000	0.888 888 888 888 889
	0.774 596 669 241 483	0.555 555 555 555 556
4	0.339 981 043 584 856	0.652 145 154 862 546
	0.861 136 311 594 053	0.347 854 845 137 454
5	0.000 000 000 000 000	0.568 888 888 888 889
	0.538 469 310 105 683	0.478 628 670 499 366
	0.906 179 845 938 664	0.236 926 885 056 189
6	0.238 619 186 083 197	0.467 913 934 572 691
	0.661 209 386 466 265	0.360 761 573 048 139
	0.932 469 514 203 152	0.171 324 492 379 170
7	0.000 000 000 000 000	0.417 959 183 673 469
	0.405 845 151 377 397	0.381 830 050 505 119
	0.741 531 185 599 394	0.279 705 391 489 277
	0.949 107 912 342 759	0.129 484 966 168 870

polynomials can be defined recursively as

$$\begin{aligned} P_0(\xi) &= 1 \\ P_1(\xi) &= \xi \\ P_n(\xi) &= \frac{2n-1}{n}\xi P_{n-1}(\xi) - \frac{n-1}{n}P_{n-2}(\xi) \qquad n \geq 2\,. \end{aligned} \tag{5.18}$$

The weights are calculated as

$$w_i = \frac{2}{(1-\xi_i^2)\big(P_n'(\xi)\big)^2}\,. \tag{5.19}$$

Both node positions and integration weights from $n = 1$ up to $n = 7$ are listed in Table 5.1.

It can be shown that a value χ inside the domain to be integrated over exists, for which the error term takes the form

$$R_n = \frac{2^{2n+1}(n!)^4}{(2n+1)\big((2n)!\big)^3} f^{(2n)}(\chi) \qquad -1 < \chi < 1\,. \tag{5.20}$$

This indicates that Gauß quadrature is able to integrate polynomials of degree up to $(2n-1)$ exactly. Furthermore, it can be shown that if $f(\xi)$ is a continuous function, the sum in Equation (5.17) converges to the actual value of the integral.

Gauß Quadrature in Two and Three Dimensions

The Gauß quadrature can easily be extended to the two-dimensional quadrilateral reference cell simply by splitting the area integral into to sums, yielding

$$\int_{-1}^{1}\int_{-1}^{1} f(\xi,\eta)\,d\xi\,d\eta = \sum_{i=1}^{n_\xi}\sum_{j=1}^{n_\eta} w_i w_j f(\xi_i,\eta_j)\,. \tag{5.21}$$

n_ξ and n_η are the number of quadrature points along the ξ and η axis, respectively. For the three-dimensional hexahedral reference element, the scheme takes the form

$$\int_{-1}^{1}\int_{-1}^{1}\int_{-1}^{1} f(\xi,\eta,\zeta)\,d\xi\,d\eta\,d\zeta = \sum_{i=1}^{n_\xi}\sum_{j=1}^{n_\eta}\sum_{k=1}^{n_\zeta} w_i w_j w_k f(\xi_i,\eta_j,\zeta_k)\,. \tag{5.22}$$

Formulations for elements other than the quadrilateral and the hexahedral ones can be obtained analogously.

5.2. Application to Gradient-Type Dissipative Continua

The following section deals with the application of the finite element method to the variational formulation describing gradient-type dissipative continua presented in Section 4.3.3.

First, the components of the generalized deformation vector $\mathbf{u}^*$ have to be interpolated. This is done element-wise using isoparametric shape functions and is written as

$$\bar{\boldsymbol{u}}^{he} = \sum_{i=1}^{n} \bar{N}_i(\boldsymbol{\xi})\bar{\boldsymbol{d}}_i^e \qquad \check{\boldsymbol{u}}^{he} = \sum_{i=1}^{n} \check{N}_i(\boldsymbol{\xi})\check{\boldsymbol{d}}_i^e \qquad \mathfrak{f}^{he} = \sum_{i=1}^{n} M_i(\boldsymbol{\xi})\boldsymbol{f}_i^e\,. \tag{5.23}$$

The resulting quantities are summarized in the vector $\mathbf{u}^{*h} \coloneqq \begin{bmatrix}\bar{\boldsymbol{u}}^{hT} & \check{\boldsymbol{u}}^{hT} & \mathfrak{f}^{hT}\end{bmatrix}^T$. The vector $\mathfrak{d}^* \coloneqq \begin{bmatrix}\bar{\boldsymbol{d}}^T & \check{\boldsymbol{d}}^T & \boldsymbol{f}^T\end{bmatrix}^T$ contains the nodal values of the solution variables. A compact notation of the interpolation reads

$$\mathbf{u}^{*h} = \mathop{\mathsf{A}}_{e=1}^{n_{el}} \sum_{i=1}^{n} \begin{bmatrix}\bar{\boldsymbol{N}}_i & \mathbf{0} & \mathbf{0}\\ \mathbf{0} & \check{\boldsymbol{N}}_i & \mathbf{0}\\ \mathbf{0} & \mathbf{0} & \boldsymbol{M}_i\end{bmatrix} \begin{bmatrix}\bar{\boldsymbol{d}}_i^e\\ \check{\boldsymbol{d}}_i^e\\ \boldsymbol{f}_i^e\end{bmatrix} = \mathfrak{N}^*(\boldsymbol{x})\mathfrak{d}^*\,, \tag{5.24}$$

where the extended global interpolation matrix $\mathfrak{N}^*$ has been introduced. In accordance with this approach, the extended constitutive state is interpolated as

$$\mathfrak{c}^{*h} = \mathop{\mathbf{A}}_{e=1}^{n_{el}} \sum_{i=1}^{n} \begin{bmatrix} \bar{\boldsymbol{B}}_i & \mathbf{0} & \mathbf{0} \\ \mathbf{0} & \check{\boldsymbol{B}}_i & \mathbf{0} \\ \mathbf{0} & \mathbf{0} & \boldsymbol{M}_i \end{bmatrix} \begin{bmatrix} \bar{\boldsymbol{d}}_i^e \\ \check{\boldsymbol{d}}_i^e \\ \boldsymbol{f}_i^e \end{bmatrix} = \mathfrak{B}^*(\boldsymbol{x})\mathfrak{d}^* \,, \tag{5.25}$$

using the vector $\mathfrak{c}^{*h} \coloneqq \begin{bmatrix} \boldsymbol{\varepsilon}^{hT} & \check{\boldsymbol{u}}^{hT} & \boldsymbol{\nabla}\check{\boldsymbol{u}}^{hT} & \mathfrak{f}^{hT} \end{bmatrix}^T$ in Voigt notation and the global matrix $\mathfrak{B}^*$.

Inserting the interpolated quantities into Equation (4.48) yields the discretized incremental potential

$$\Pi_\eta^{*\tau h}(\mathfrak{d}^*) = \int_{\mathcal{B}^h} \left[\pi_\eta^{*\tau h}(\mathfrak{c}^{*h}, \mathfrak{c}_n^{*h}) - \mathfrak{g} \cdot \mathfrak{N}(\mathfrak{d} - \mathfrak{d}_n)\right] \, dV - \int_{\partial\mathcal{B}_\mathfrak{t}^h} \mathfrak{t}_N \cdot \mathfrak{N}(\mathfrak{d} - \mathfrak{d}_N) \, dA \,. \tag{5.26}$$

Next, the stationary principle given in Equation (4.50) is applied

$$D\Pi_\eta^{*\tau h}[\delta\mathfrak{d}^*] = \partial_{\mathfrak{d}^*}\Pi_\eta^{*\tau h} \cdot \delta\mathfrak{d}^* = 0 \,. \tag{5.27}$$

Since $\delta\mathfrak{d}^*$ denotes an arbitrary variation of the solution variables, the nonlinear system of equations to be solved can be formulated as

$$\partial_{\mathfrak{d}^*}\Pi_\eta^{*\tau h} = \int_{\mathcal{B}^h} \left(\mathfrak{B}^{*T}\boldsymbol{S} - \mathfrak{N}^T\mathfrak{g}\right) \, dV - \int_{\partial\mathcal{B}_\mathfrak{t}^h} \mathfrak{N}^T\mathfrak{t}_N \, dA = 0 \,, \tag{5.28}$$

introducing the vector of generalized stresses $\boldsymbol{S} = \partial_{\mathfrak{c}^{*h}}\pi_\eta^{*\tau h}$. Equation (5.28) is solved with the Newton-Raphson method explained in Section 2.1. At the beginning of each time step, an initial guess $\mathfrak{d}_0^*$ has to be chosen. At the k-th iteration, the solution is calculated as

$$\mathfrak{d}_k^* = \mathfrak{d}_{k-1}^* - \left[\partial^2_{\mathfrak{d}^*\mathfrak{d}^*}\Pi_\eta^{*\tau h}(\mathfrak{d}_{k-1}^*)\right]^{-1} \partial_{\mathfrak{d}^*}\Pi_\eta^{*\tau h}(\mathfrak{d}_{k-1}^*) \,. \tag{5.29}$$

The symmetric tangent matrix is computed as

$$\partial^2_{\mathfrak{d}^*\mathfrak{d}^*}\Pi_\eta^{*\tau h} = \int_{\mathcal{B}^h} \mathfrak{B}^{*T}\boldsymbol{C}^*\mathfrak{B}^* \, dV \tag{5.30}$$

and makes use of the extended generalized moduli $\boldsymbol{C}^* = \partial^2_{\mathfrak{c}^{*h}\mathfrak{c}^{*h}}\pi_\eta^{*\tau h}$. When the convergence criterion

$$\left\| \partial_{\mathfrak{d}^*}\Pi_\eta^{*\tau h}(\mathfrak{d}_k^*) \right\| \leq \mathrm{TOL} \tag{5.31}$$

is fulfilled, the procedure is terminated and the next time step is treated.

A proper choice of the initial guess $\mathfrak{d}_0^*$ is crucial for fast convergence of the Newton-Raphson method. The converged solution of the previous time step is an appropriate choice for each time step except the first one. At time $t = 0$ the body is not subject to any deformations, therefore $\mathfrak{d}_0^* = \mathbf{0}$ is chosen.

6. Application to Gradient-Type Damage Mechanics

The aim of this chapter is the application of the variational framework developed in Chapter 4 to an isotropic gradient-type damage model.

The first section elaborates on the theory of stability and the phenomenon of localization. It points out the drawbacks of a local formulation and provides the continuum-mechanical basis for a gradient-type extension.

Section 6.2 discusses the theoretical background of continuum damage mechanics. After a short description of physical damage mechanisms, a precise definition of damage in a continuum-mechanical sense is given. Furthermore, the concept of effective state variables is described. It represents the prerequisite for the inclusion of a damage model into a variational framework.

In the third section, the constitutive functions for an isotropic, gradient-extended damage model are derived. In a next step, a variational formulation using the framework treated in Chapter 4 is developed. Finally, an algorithm for solving the emerging system of nonlinear differential equations using the finite element method is presented.

6.1. Stability and Localization

Consider a solid consisting of a inelastic, strain-softening material. When such a solid is loaded into the inelastic regime, deformations are often concentrated inside small regions of the body. This effect is known as *localization* and is a consequence of material instability. It is often associated with the loss of uniqueness of the solution of the boundary value problem, referred to as *bifurcation*. Solving such a boundary value problem with the finite element method leads to a solution depending on the mesh size. This behavior is clearly nonphysical, and therefore undesirable.

Section 6.1.1 gives an overview of the theory of bifurcations and under which conditions they occur. It uses the papers by Hill [12] and Neilsen & Schreyer [18] as main references.

The major sources of Section 6.1.2 are De Borst [9], De Borst [10, p.344ff], and Schreyer & Chen [20]. It elaborates on mesh sensitivity and localization by the example of a one-dimensional bar consisting of a strain-softening material.

6.1.1. Theoretical Background on Bifurcations

Bifurcations can be divided into two groups, namely diffuse and discontinuous ones. Which of these two types emerges depends on the material model used.

The former is characterized by kinematic incompatibility. The zone of localization is described as a domain of measure zero, e.g. as a point or surface. Changes in the deformation field always occur smoothly, hence the name diffuse bifurcation.

Regarding discontinuous bifurcations, no kinematic incompatibilities with the surrounding material occur. The mode is associated with a jump in the strain rate within a band over the strain rate in the surrounding material. The localization zone is not of measure zero, but covers a finite domain. Evolution of this domain must be controlled by additional constraints. The gradient-type constitutive theory treated in this thesis provides such constraints.

This section uses the notation introduced by Neilsen & Schreyer [18].

General and Limit Point Bifurcations

The most general stability criterion considers the external loading acting on the material. If the work done by the external loading is positive, and the net work done by it over a cycle of application and removal is greater than zero, the material remains stable. The net work can only be non-zero, if inelastic deformation is created during the cycle. These considerations lead to the stability criterion

$$\dot{\boldsymbol{\varepsilon}} : \dot{\boldsymbol{\sigma}} = 0 \,. \tag{6.1}$$

Using the tangent modulus tensor $\mathbb{C}$, the relationship between the stress rate $\dot{\boldsymbol{\sigma}}$ and the strain rate $\dot{\boldsymbol{\varepsilon}}$ can be expressed as

$$\dot{\boldsymbol{\sigma}} = \mathbb{C} : \dot{\boldsymbol{\varepsilon}} \,. \tag{6.2}$$

Equation (6.1) represents a necessary condition for any type of bifurcation. By inserting Equation (6.2) and exploiting the symmetry of $\dot{\boldsymbol{\sigma}}$ and $\dot{\boldsymbol{\varepsilon}}$, the *general bifurcation criterion* can be formulated as

$$\dot{\boldsymbol{\varepsilon}} : \mathbb{C}^S : \dot{\boldsymbol{\varepsilon}} = 0 \,. \tag{6.3}$$

$\mathbb{C}^S$ is the symmetric part of the tangent modulus tensor. Its components read $\mathbb{C}^S_{ijkl} = \frac{1}{2}\left(\mathbb{C}^S_{ijkl} + \mathbb{C}^S_{klij}\right)$.

If the constitutive model provides no constraints, a necessary and sufficient condition for loss of material stability is a zero stress rate. With Equation (6.2), the *limit point criterion* can be written as

$$\mathbb{C} : \dot{\boldsymbol{\varepsilon}} = \mathbf{0} \quad \text{or} \quad \det\left(\mathbb{C}\right) = 0 \,. \tag{6.4}$$

If constraints are provided, instability does not necessarily occur at the limit point. The discontinuous bifurcation criteria which need to be evaluated in this case are described in the following.

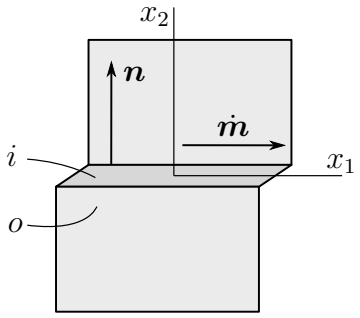

$$\boldsymbol{n} = \begin{bmatrix} 0 \\ 1 \\ 0 \end{bmatrix} \qquad \dot{\boldsymbol{m}} = \begin{bmatrix} \alpha \\ 0 \\ 0 \end{bmatrix} \,,\ \alpha \in \mathbb{R}$$

Figure 6.1.: Geometric setup of a discontinuous bifurcation with kinematically compatible mode. The vector $\boldsymbol{n}$ represents the orientation of the planes separating the localization zone from the rest of the body. The direction of their movement is given by $\dot{\boldsymbol{m}}$.

Discontinuous Bifurcations and Loss of Strong Ellipticity

Discontinuous bifurcations are characterized by discontinuity of strain rates across parallel planes which separate a zone of localization from the rest of the body. The vector $\boldsymbol{n}$ denotes the orientation of these planes, and the vector $\dot{\boldsymbol{m}}$ indicates the direction of their movement due to the proceeding localization. Both vectors are shown exemplarily for the shearing mode of a discontinuous bifurcation in Figure 6.1. Maxwell's condition for kinematic compatibility reads

$$\dot{\boldsymbol{\varepsilon}}^i = \dot{\boldsymbol{\varepsilon}}^o + \dot{\boldsymbol{\varepsilon}}^k \quad \text{with} \quad \dot{\boldsymbol{\varepsilon}}^k = \frac{1}{2}\left(\dot{\boldsymbol{m}} \otimes \boldsymbol{n} + \boldsymbol{n} \otimes \dot{\boldsymbol{m}}\right) , \tag{6.5}$$

where $\dot{\boldsymbol{\varepsilon}}^i$ and $\dot{\boldsymbol{\varepsilon}}^o$ are the strain rates inside and outside the localized zone, respectively. $\dot{\boldsymbol{\varepsilon}}^k$ depicts the kinematically admissible discontinuity between these two zones.

In contrary to the strain rate, the stress rate must remain continuous across the boundary of the localized zone at all times. This equilibrium condition is written as

$$\dot{\boldsymbol{t}}^i = \dot{\boldsymbol{t}}^o \quad \text{or} \quad \boldsymbol{n} \cdot \left(\dot{\boldsymbol{\sigma}}^i - \dot{\boldsymbol{\sigma}}^o\right) = \boldsymbol{0} \,. \tag{6.6}$$

Inserting Equations (6.2) and (6.5), along with exploiting the minor symmetry $\mathbb{C}_{ijkl} = \mathbb{C}_{ijlk}$ of the tangent modulus tensor, yields

$$\boldsymbol{n} \cdot \left(\mathbb{C}^i - \mathbb{C}^o\right) : \dot{\boldsymbol{\varepsilon}}^o + \underbrace{\left(\boldsymbol{n} \cdot \mathbb{C}\boldsymbol{n}\right)}_{\mathbb{Q}} \cdot \dot{\boldsymbol{m}} = \boldsymbol{0} \,. \tag{6.7}$$

The *acoustic tensor* $\mathbb{Q} \coloneqq \boldsymbol{n} \cdot \mathbb{C}\boldsymbol{n}$ introduced in the previous equation plays an essential role in the description of discontinuous bifurcations. Assuming that the relationship $\mathbb{C}^i = \mathbb{C}^o$ holds during the initiation of the localized zone, the *classical discontinuous bifurcation criterion* reads

$$\mathbb{Q}\dot{\boldsymbol{m}} = \boldsymbol{0} \quad \text{or} \quad \det\left(\mathbb{Q}\right) = 0 \,. \tag{6.8}$$

It is equivalent to the acoustic tensor having a zero eigenvalue.

Table 6.1.: Bifurcation criteria and modes

Criterion	Equation
General bifurcation	$0 = \dot{\boldsymbol{\varepsilon}} : \mathbb{C}^S : \dot{\boldsymbol{\varepsilon}}$
Limit point	$\mathbf{0} = \mathbb{C} : \dot{\boldsymbol{\varepsilon}}$
Loss of strong ellipticity	$0 = \dot{\boldsymbol{m}} \cdot \mathbb{Q}^S \dot{\boldsymbol{m}}$
Classical discontinuous bifurcation	$\mathbf{0} = \mathbb{Q} \dot{\boldsymbol{m}}$

A more general stability criterion can be formulated if two assumptions are discarded. The first one is the special form of $\dot{\boldsymbol{\varepsilon}}^k$ given in Equation (6.5), the second one is the equality of $\mathbb{C}^i$ and $\mathbb{C}^o$ at the initiation of localization. A general necessary condition for a discontinuous bifurcation with a kinematically compatible mode $\dot{\boldsymbol{\varepsilon}}^k$ can then be formulated as the *loss of strong ellipticity criterion*

$$\dot{\boldsymbol{\varepsilon}}^k : \mathbb{C}^S : \dot{\boldsymbol{\varepsilon}}^k = 0 \implies \dot{\boldsymbol{m}} \cdot \mathbb{Q}^S \dot{\boldsymbol{m}} = 0 \,. \tag{6.9}$$

A summary of the various bifurcation criteria presented in this section can be found in Table 6.1.

6.1.2. Localization and Mesh Sensitivity

The previous section extensively discussed various bifurcation criteria which lead to localization. In the following, the localization behavior of strain-softening materials in the post-critical regime, i.e. after loss of stability, shall be examined by the example of a one-dimensional solid.

Consider a bar of overall length $L = a + b$ with unit cross-sectional area under uniaxial loading σ, as depicted in Figure 6.2a. It consists of two segments labeled A and B. They are described by the same constitutive law, except that the limit stress σ_0 of region B is infinitesimally smaller than that of region A.

In the elastic domain $0 < \varepsilon < \varepsilon_0$ Hooke's law is applied using Young's modulus E. The post-critical region $\varepsilon > \varepsilon_0$ is described by a linear softening law with constant slope hE. The constitutive behavior of the material is shown in Figure 6.3a.

The first part of this section demonstrates the difficulties which may arise when strain-softening materials are treated with a local continuum theory. Furthermore, the mesh-size dependency of the finite element solution is examined. In the second part, a non-local formulation is introduced which will be mesh invariant.

Local Approach

For given strains ε_a and ε_b of regions A and B, the elongations of the respective domains can be written as

$$\delta_a = a\varepsilon_a \quad \text{and} \quad \delta_b = b\varepsilon_b \,. \tag{6.10}$$

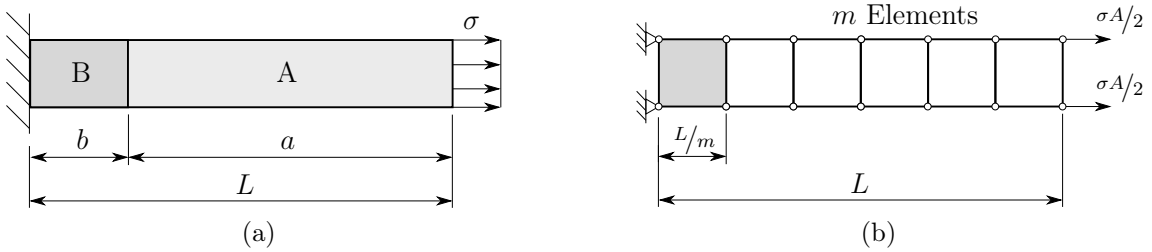

Figure 6.2.: (a) A bar of length $L = a + b$ with unit cross-sectional area under uni-axial loading. Region B has a slightly lower yield stress then region A. (b) A finite element discretization of the bar, where the weakest element is colored gray.

The composite strain of the entire bar then results in

$$\delta = \delta_a + \delta_b \implies \varepsilon = \frac{\delta}{L} = \frac{a}{L}\varepsilon_a + \frac{b}{L}\varepsilon_b \,. \tag{6.11}$$

In order to obtain the composite constitutive behavior of the bar, the relationship between an incremental stress $\Delta\sigma$ and the resulting incremental overall strain $\Delta\varepsilon$ is investigated. Inside the elastic domain, the constitutive response of segments A and B is identical. In the post-critical domain, however, this is no longer true. For a given incremental strain of domain B, the resulting stress can be calculated as

$$\Delta\sigma = hE\Delta\varepsilon_b \,. \tag{6.12}$$

As a consequence of equilibrium, the incremental stress is constant throughout the bar. While the material inside region B is subject to strain-softening, elastic unloading occurs in region A. The incremental strain of region A can therefore be written as

$$\Delta\varepsilon_a = \frac{\Delta\sigma}{E} = h\Delta\varepsilon_b \,. \tag{6.13}$$

Inserting this relationship into Equation (6.11) yields

$$\Delta\varepsilon = \frac{b + ah}{L}\Delta\varepsilon_b \,. \tag{6.14}$$

Combining Equations (6.14) and (6.12) results in the composite constitutive law of the bar

$$\Delta\sigma = \eta E\Delta\varepsilon \quad \text{with} \quad \eta = \frac{hL}{hL + b(1-h)} \,, \tag{6.15}$$

where the relationship $a = L - b$ has been exploited.

Equation (6.15) shows that the global constitutive response of the bar depends on b, which is unknown. Hence, an infinite amount of solutions is obtained. This circumstance is illustrated in Figure 6.3. As already mentioned, it is assumed that only the weakest region of the entire domain, here B, undergoes softening. All stronger regions are subject to elastic unloading.

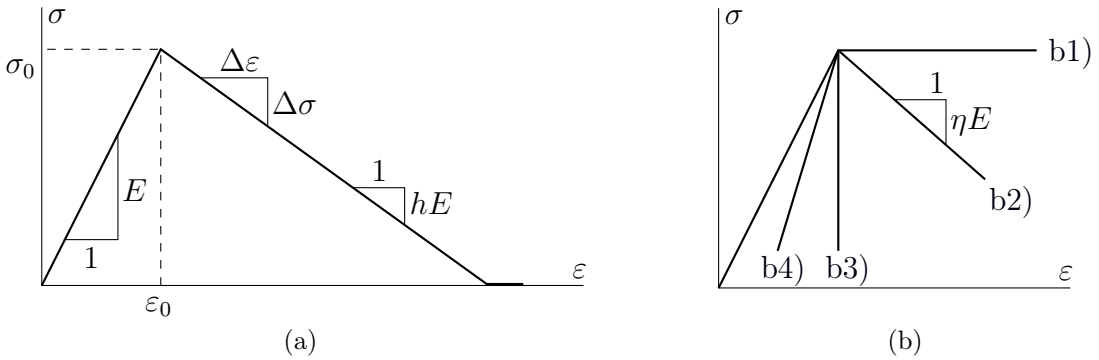

Figure 6.3.: (a) The local constitutive behavior of the material. (b) The global response of the bar for b1) $\eta = 0$, b2) $-\infty < \eta < 0$, b3) $\eta \to \infty$, and b4) $1 < \eta < \infty$.

Since the segment B may be arbitrarily small, the limit case $b \to 0$ shall be investigated. Following Equation (6.15), b approaching zero implies $\eta \to 1$. The softening branch for this scenario approaches the linear-elastic line $\sigma = E\varepsilon$, see Figure 6.3. However, this behavior is clearly nonphysical, since the energy dissipation associated with localization zones of vanishingly low size decreases to unrealistic values.

Another problem regarding the numerical treatment of strain-softening materials arises. Consider the finite element mesh depicted in Figure 6.2b which discretizes the bar. Localization is limited to the element in which loss of stability occurs for the first time. The size of one element is therefore equivalent to the value of b in Equation (6.15). For a constant length L, b can be calculated as $b = {}^{L}/_{m}$, with m being the number of elements. Consequently, the solution depends on the mesh size, which definitively is unwanted behavior.

From a mathematical point of view, the loss of stability is associated with the loss of ellipticity of the governing partial differential equations. The resulting loss of well-posedness of the problem leads to the loss of uniqueness of its solution. See Section 6.1.1 for further information.

The non-local approach described hereafter shall provide a remedy to the downsides of a local formulation.

Gradient-Extended Approach

The same bar as in the previous section is examined. As before, the material is characterized by linear-elastic behavior in the elastic domain and a post-critical linear softening law, as shown in Figure 6.3a. This time, however, the domain is not divided into two regions A and B, but the weakest point P_1 and its surrounding are investigated. The setup is shown in Figure 6.4a.

In a first step, the total strain is decomposed into a an elastic and an inelastic component

$$\varepsilon = \varepsilon^e + \varepsilon^p \,. \tag{6.16}$$

Since the plastic strain ε^p does not produce any stress, Hooke's law can be rewritten as

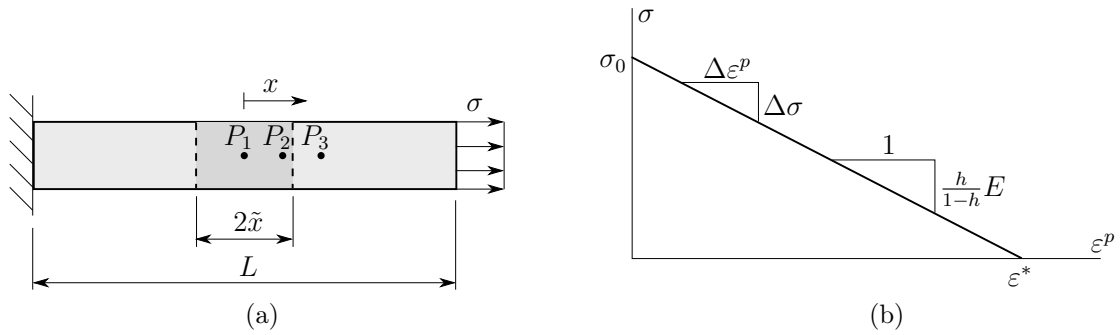

Figure 6.4.: (a) Geometric setup of a bar of length L for a non-local approach. The coordinate system has its origin in the weakest point P_1. (b) Relationship between the plastic strain ε^p and the stress σ.

$\Delta\sigma = E\Delta\varepsilon^e$. The incremental post-critical stress-strain relationship reads $\Delta\sigma = hE\Delta\varepsilon$. Together with (6.16), these two equations deliver the incremental plastic strain in terms of incremental stress as

$$\Delta\varepsilon^p = \frac{h}{1-h} E\Delta\sigma\,. \tag{6.17}$$

Since $\sigma = \sigma_0$ at $\varepsilon^p = 0$, Equation (6.17) can be reformulated, resulting in the relationship between stress and plastic strain as

$$\varepsilon^p = \left(1 - \frac{\sigma}{\sigma_0}\right)\varepsilon^* \tag{6.18}$$

Above, the *ultimate plastic strain* $\varepsilon^* := -\frac{1-h}{h} E\sigma_0$ has been introduced. The linear function given in Equation (6.18) is visualized in Figure 6.4b. Note the considerations made so far are of general nature, and therefore are also valid for a local treatment.

In order to prevent localization of the softening zone inside an arbitrarily small domain, the local plastic strain is extended by an additional gradient-type term, yielding

$$\varepsilon^p_\nabla := \varepsilon_p + l^2 \left(\frac{d\varepsilon^p}{dx}\right)^2 . \tag{6.19}$$

In the previous equation, the *length scale parameter* $l \in \mathbb{R}^+$ has been introduced. It governs the size of the localization zone and has the dimension of a length. Inserting the gradient-extended plastic strain into Equation (6.18) results in the nonlinear first-order ordinary differential equation

$$\varepsilon_p + l^2 \left(\frac{d\varepsilon^p}{dx}\right)^2 = \left(1 - \frac{\sigma}{\sigma_0}\right)\varepsilon^* . \tag{6.20}$$

Its trivial solution is already shown in Equation (6.18). It is equivalent to the case $l = 0$, and thus corresponds to the local theory. In this case the plastic strain is constant over the whole softening region.

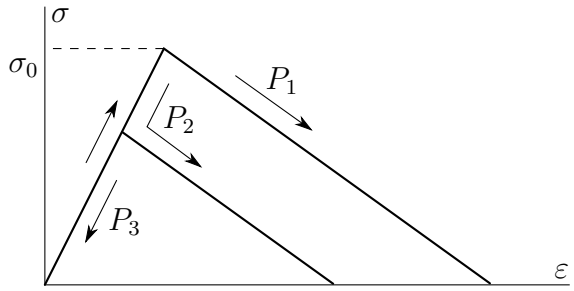

Figure 6.5.: Local constitutive behavior of the points P_1, P_2 and P_3. Plastification begins at P_1 immediately after the yield stress σ_0 is reached. P_2 unloads elastically until the local yield limit is reduced sufficiently for softening to occur. The point P_3 unloads elastically at all times.

The nontrivial, non-local solution for $l > 0$ reads

$$\varepsilon^p(x) = \left(1 - \frac{\sigma}{\sigma_0}\right)\varepsilon^* - \frac{x^2}{4l^2}\,. \tag{6.21}$$

In addition to the distribution of ε^p, the size of the softening zone is of interest. Since ε^p must not be negative, the condition $\varepsilon^p = 0$ is used to identify the domain in which the plastic strain is greater than zero as

$$-\tilde{x} < x < \tilde{x} \quad \text{with} \quad \tilde{x} = 2l\sqrt{\left(1 - \frac{\sigma}{\sigma_0}\right)\varepsilon^*}\,. \tag{6.22}$$

As expected, the localization zone $\tilde{x}$ is zero for a local approach with $l = 0$. For a non-local approach, softening starts at the weakest point P_1 with $\sigma = \sigma_0$ and $\tilde{x} = 0$. The softening zone then increases and reaches its maximum value

$$\tilde{x}_{max} = 2l\sqrt{\varepsilon^*} \tag{6.23}$$

at $\sigma = 0$.

The mechanism which lead to the spreading of the localization zone shall be explained by the example of three points P_1, P_2 and P_3, which are shown in Figure 6.4a. The first one, P_1, has the coordinate $x = 0$ and is located at the weakest position of the bar. Therefore, it is the point where plastification is initiated at $\sigma = \sigma_0$. The second point P_2, positioned inside the final localization zone $0 < x \leq \tilde{x}_{max}$, initially unloads elastically. The plastic strain increases due to the gradient-extended term, until at some point it reduces the local yield limit $\sigma_0\left(1 - \frac{\varepsilon^p_\nabla}{\varepsilon^*}\right)$ sufficiently for plastification to occur at a stress $\sigma < \sigma_0$. Any point P_3 with coordinate $x > \tilde{x}_{max}$ outside the final plastification zone unloads elastically until the stress goes back to zero. Figure 6.5 displays the process described above.

6.2. Background on Continuum Damage Mechanics

In this section, the theoretical basis for the damage model described in Section 6.3 is laid.

The first two Subsections 6.2.1 and 6.2.2 shortly summarize physical damage mechanisms and present various definitions of damage variables and their fields of application. For further information, the reader is referred to the book by Lemaitre & Desmorat [15].

Subsection 6.2.3 bases on the paper by Simo & Ju [21]. It addresses the two distinct concepts of effective stress and effective strain. The latter will be used in Section 6.3 in order to formulate the constitutive equations of the material model treated in this thesis.

6.2.1. Damage Mechanisms

Continuum damage mechanics provides the basis for predicting crack initiation in structures. It is fundamentally associated with the creation and growth of microscopic voids and cracks. These imperfections represent discontinuities inside a solid. In order to handle them with a continuum-based approach, a *Representative Volume Element* (RVE) is introduced at a scale of larger magnitude than the discontinuities. All quantities of interest are homogenized over the RVE and can therefore be viewed as continuous fields.

The various damage mechanisms are classified according to the length scale they can be observed on, as well as the frequency of the load cycle the structure is subjected to. Further factors, such as temperature, might as well influence the material behavior.

- On the scale of the RVE, also called mesolevel, *ductile damage* is the evolution of cavities under static loading. *Creep damage* is associated with decohesions in metals and occurs at elevated temperature. If mesoplasticity is induced under repeated high level loadings, one talks of *low cycle fatigue*.
- The scale of the discontinuities is called microlevel. *Brittle failure* is damage induced at this level under monotonic loading. *High cycle fatigue damage*, on the other hand, occurs under a large number of repeated load cycles.

6.2.2. Damage Variables

In order to capture the effects of damage within a continuum-based theory, a continuous damage variable is introduced. Its definition depends on the damage mechanism induced as well as on the material properties. For the isotropic case, the assumption of a scalar damage variable is reasonable. For the more complicated anisotropic case, a fourth-order tensor is used.

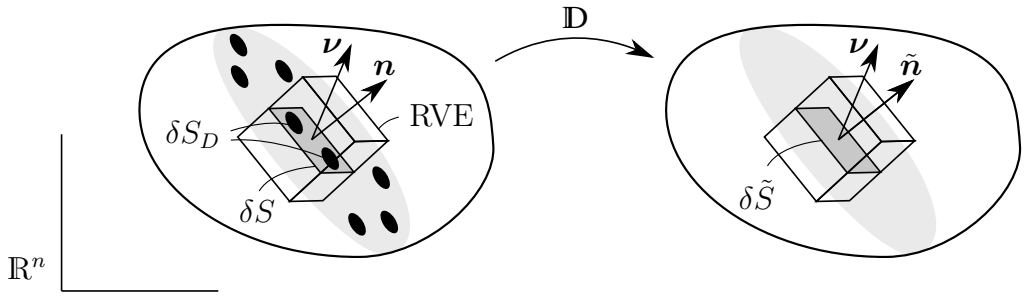

Figure 6.6.: On the left, the geometric reference configuration is displayed. The area δS is defined as the intersection of a plane with normal vector $\boldsymbol{n}$ and the RVE. The fourth-order tensor $\mathbb{D}$ transforms the reference configuration into the effective configuration, which can be viewed on the right.

Scalar Damage Variables

The simplest formulation bases on the assumptions that no microcracks are created inside the solid. It is then sufficient to define damage as the density of microvoids,

$$d_V \coloneqq \frac{\delta V_{\text{voids}}}{\delta V_{\text{RVE}}} \tag{6.24}$$

with δV_{voids} being the volume of all microcavities inside the RVE, and δV_{RVE} being the volume of the element itself.

If, additionally to cavities, microcracks may exist, a slightly more elaborate approach is used. Consider the intersection δS of a plane with normal vector $\boldsymbol{n}$ and the RVE, as depicted in Figure 6.6. The surface of all mickrocracks and intersections of microvoids is named δS_D. The damage variable is defined for the plane with normal $\boldsymbol{n}$ where the surface density

$$d\left(\boldsymbol{n}\right) \coloneqq \frac{\delta S_D}{\delta S} \tag{6.25}$$

reaches its maximum.

For isotropic materials the dependency on $\boldsymbol{n}$ can be dropped, since the damage variable does not depend on the direction of the plane in this case.

Tensorial Damage Variable

The most general representation of a damage variable is given by a fourth-order tensor $\mathbb{D}$. Again, consider a damage plane area δS with normal vector $\boldsymbol{n}$. Additionally, a reference vector $\boldsymbol{\nu}$ is introduced such that the second-order tensor $\boldsymbol{\nu} \otimes \boldsymbol{n}\delta S$ defines the geometric reference configuration. The effective configuration is characterized by the continuous effective damage area

$$\delta\tilde{S} \coloneqq \delta S - \delta S_D \tag{6.26}$$

and its normal vector $\tilde{\boldsymbol{n}}$. The described geometric setup is shown in Figure 6.6.

The damage variable $\mathbb{D}$ is defined as an operator which transforms the geometric reference configuration into the effective configuration. This can be written as

$$\boldsymbol{\nu} \cdot (\mathbb{I} - \mathbb{D})\, \boldsymbol{n} \delta S = \boldsymbol{\nu} \otimes \tilde{\boldsymbol{n}} \delta \tilde{S}\,, \tag{6.27}$$

where $\mathbb{I}$ is the fourth-order identity tensor. The fourth-order damage tensor possesses the major symmetry $\mathbb{D}_{ijkl} = \mathbb{D}_{klij}$ and the minor symmetries $\mathbb{D}_{ijkl} = \mathbb{D}_{jikl} = \mathbb{D}_{ijlk}$.

6.2.3. Effective State Concepts

The constitutive equations of damage mechanics characterize the plain material without volume or surface discontinuities. However, when damage occurs, the material configuration changes according to Equation (6.27). Any constitutive equations may still be derived in the same way as for a virgin material, if the underlying quantity is replaced by an effective counterpart. This quantity may be the stress or the strain, depending on the formulation of the constitutive equations.

Effective Stress Concept

The *effective stress concept* introduces the effective stress tensor $\tilde{\boldsymbol{\sigma}}$, which acts on the resisting area $\delta\tilde{S}$.

For the isotropic case, it can be determined formulating the force equilibrium

$$\tilde{\boldsymbol{\sigma}} \delta \tilde{S} = \boldsymbol{\sigma} \delta S\,. \tag{6.28}$$

Inserting the definition of the scalar damage variable (6.25) as well as Equation (6.26) yields

$$\tilde{\boldsymbol{\sigma}} = \frac{1}{1-d} \boldsymbol{\sigma}\,. \tag{6.29}$$

The treatment of anisotropic damage behavior is slightly more complicated. The effective stress tensor is now defined using the projection of the traction vector $\boldsymbol{t} = \boldsymbol{\sigma}\boldsymbol{n}$ on the reference vector $\boldsymbol{\nu}$, resulting in

$$\boldsymbol{\nu} \cdot \tilde{\boldsymbol{\sigma}} \tilde{\boldsymbol{n}} \delta \tilde{S} = \boldsymbol{\nu} \cdot \boldsymbol{\sigma} \boldsymbol{n} \delta S\,. \tag{6.30}$$

By inserting the definition of the damage tensor given in Equation (6.27) and exploiting its symmetries, the effective stress tensor can be expressed as

$$\tilde{\boldsymbol{\sigma}} = \mathbb{M} : \boldsymbol{\sigma} \quad \text{with} \quad \mathbb{M} \coloneqq (\mathbb{I} - \mathbb{D})^{-1}\,. \tag{6.31}$$

Note that Equation (6.31) can be converted into Equation (6.29) if damage and material behavior are isotropic.

The *hypothesis of strain equivalence*, postulated by Lemaitre, states that "the strain associated with a damaged state under the applied stress is equivalent to the strain associated with its undamaged state under the effective stress". This statement is of importance when it comes to the formulation of constitutive equations. See Lemaitre [14, p.13f] for further details.

Effective Strain Concept

An alternative effective state is provided by the *concept of effective strain*. Analogously to the effective stress, the effective strain is generally defined as

$$\tilde{\boldsymbol{\varepsilon}} = \mathbb{M}^{-1} : \boldsymbol{\varepsilon}\,, \tag{6.32}$$

where $\mathbb{M}$ is given in Equation (6.31). If the damage behavior is isotropic, this relationship can be reformulated as

$$\tilde{\boldsymbol{\varepsilon}} = (1-d)\,\boldsymbol{\varepsilon}\,. \tag{6.33}$$

In complete analogy to the the hypothesis of equivalent strain, the *hypothesis of equivalent stress* is postulated. It states that the stress associated with a damaged state under the applied strain is equivalent to the stress associated with its undamaged state under the effective strain.

6.3. Isotropic Gradient-Extended Damage Mechanics at Small Deformations

In the following section, the gradient-extended theory presented in Chapter 4 is applied to an isotropic model problem of damage mechanics proposed by Welschinger [25, p. 76ff]. In order to depict rate-dependent behavior, an extended three-field approach is chosen. The constitutive state and a precise definition of the damage variable is provided in the first subsection. The constitutive functions describing the material behavior are described in Section 6.3.2. Subsequently, the strong form of the governing balance equations is derived. Section 6.3.4 applies the time-discrete incremental variational principle displayed in Section 4.3 to the present material model, yielding a set of coupled nonlinear equations suited for a numerical treatment. Finally, the discretization of said equations with the finite element method is discussed.

6.3.1. Constitutive State and Damage Description

The general kinematic setup of a solid with microstructure is described in Section 4.1. It shall be specified for the used material model hereafter.

In addition to the macroscopic displacement $\boldsymbol{u}(\boldsymbol{x},t)$, a scalar-valued field $\alpha(\boldsymbol{x},t)$ is introduced. It represents the deterioration of the microstructure due to the creation and growth of microscopic cracks and cavities. Altogether, the generalized deformation vector reads

$$\mathfrak{u} \coloneqq \{\bar{\boldsymbol{u}}, \check{\boldsymbol{u}}\} \quad \text{with} \quad \bar{\boldsymbol{u}} \coloneqq \{\boldsymbol{u}\} \quad \text{and} \quad \check{\boldsymbol{u}} \coloneqq \{\alpha\}\,. \tag{6.34}$$

In conformity with the notation of Section 4.2.1, the constitutive state is given as

$$\mathfrak{c}(\mathfrak{u}) \coloneqq \{\boldsymbol{\varepsilon}, \alpha, \boldsymbol{\nabla}\alpha\}\,. \tag{6.35}$$

A depiction of rate-dependent behavior requires the usage of thermodynamic driving forces. They are described in a general manner in Section 4.2.5. Here, dissipative

macroscopic stresses represented by $\bar{\boldsymbol{\mathcal{F}}}$ are neglected. A scalar-valued field $\beta(\boldsymbol{x}, t)$ is introduced, which denotes the driving force

$$\check{\boldsymbol{f}} \coloneqq \{\beta\} \tag{6.36}$$

conjugate to the deterioration field α.

The quantities introduced above form the basis for the construction of the constitutive equations in Section 6.3.2. They are subsumed in the extended constitutive state

$$\mathfrak{c}^*(\mathfrak{u}^*) \coloneqq \{\boldsymbol{\varepsilon}, \alpha, \boldsymbol{\nabla}\alpha, \beta\} \quad \text{with} \quad \mathfrak{u}^* \coloneqq \{\boldsymbol{u}, \alpha, \beta\}\,. \tag{6.37}$$

In the following, a description of the damage variable is given. First, an additive decomposition of the macroscopic strain $\boldsymbol{\varepsilon} = \boldsymbol{\nabla}^S \boldsymbol{u}$ into an elastic part $\boldsymbol{\varepsilon}^e$ and an inelastic part $\boldsymbol{\varepsilon}^d$ is conducted, yielding

$$\boldsymbol{\varepsilon} = \boldsymbol{\varepsilon}^e + \boldsymbol{\varepsilon}^d\,. \tag{6.38}$$

The elastic, stress producing part $\boldsymbol{\varepsilon}^e$ is identified with the effective strain $\tilde{\boldsymbol{\varepsilon}}$ introduced in Section 6.2.3. For isotropic damage behavior, the exploitation of the equivalent stress hypothesis leads to a representation of the elastic strain tensor as

$$\boldsymbol{\varepsilon}^e = \mathbb{M} : \boldsymbol{\varepsilon} = \big(1 - d(\alpha)\big) \quad \text{with} \quad \mathbb{M} = \big(1 - d(\alpha)\big)\mathbb{I}^S\,, \tag{6.39}$$

where the fourth-order symmetric identity tensor $\mathbb{I}^S_{ijkl} \coloneqq \frac{1}{2}\left(\delta_{ik}\delta_{jl} + \delta_{il}\delta_{jk}\right)$ has been used.

The function $d(\alpha)$ introduced in Equation (6.39) establishes a connection between the microstructural deterioration α and the *scalar damage variable* d. In order to depict damage behavior reliably, $d(\alpha)$ must be monotonically increasing and smooth. Furthermore, all values of $\alpha \in [0, \infty)$ must be mapped onto the interval $d \in [0, 1]$. This arises as a result from the definition of the damage variable given in Section 6.2.2, where $d = 0$ describes the virgin state of the material, and $d = 1$ the fully damaged state.

A mapping which fulfills all of the criteria mentioned above can be written as

$$d(\alpha) = 1 - (1 + \alpha)^{-\nu}\,, \tag{6.40}$$

where the dimensionless parameter $\nu \in \mathbb{R}^+$ determines the rate of damage evolution. Figure 6.7 displays the graph of the damage function given in Equation (6.40) for various values of ν.

6.3.2. Constitutive Functions

As mentioned at the beginning of Section 4.2.2, the constitutive response of a material is defined by the energy storage function ψ and the dissipation function ϕ. For the rate-dependent three-field formulation at hand, the latter one is derived from a constitutive yield function φ.

The free energy stored inside the solid is connected to the effective strain, which in turn is associated with the macroscopic strain and the deterioration α. Additional energy storage mechanisms are taken into account which depend on the gradient of the

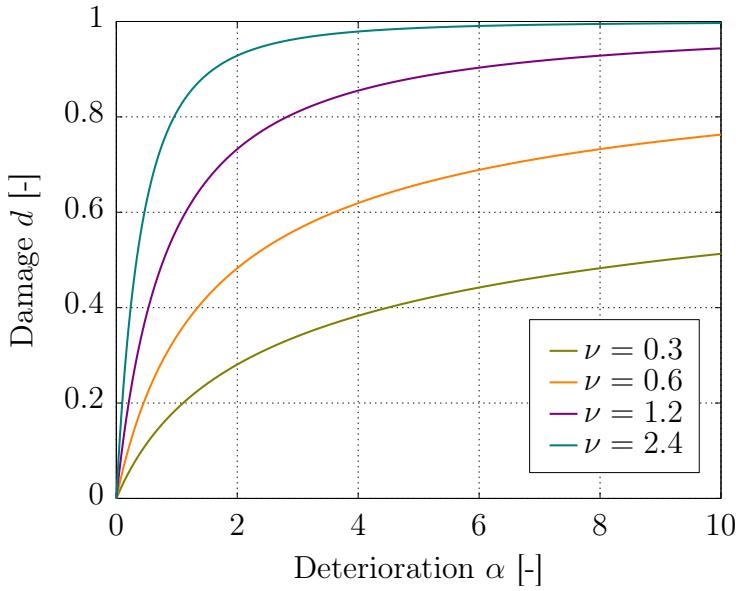

Figure 6.7.: The relationship between the deterioration α and the damage variable d is shown for various damage parameters ν. A higher value of ν causes a more rapid damage evolution.

deterioration field $\boldsymbol{\nabla}\alpha$. Thus, the energy storage function is given in the decoupled representation

$$\psi(\mathfrak{c}) = \psi_{loc}(\boldsymbol{\varepsilon}^e(\boldsymbol{\varepsilon}, \alpha)) + \psi_{non}\left(\boldsymbol{\nabla}\alpha\right) . \tag{6.41}$$

While the first term ψ_{loc} denotes the energy storage mechanisms treated in a classical local theory, ψ_{non} describes the non-local influence of microstructural cracks and cavities specific for a gradient-type damage formulation. For the material model in use, the two components of Equation (6.41) take the form

$$\begin{aligned} \psi_{loc}(\boldsymbol{\varepsilon}^e(\boldsymbol{\varepsilon}, \alpha)) &= \frac{1}{2} \parallel \boldsymbol{\varepsilon}^e(\boldsymbol{\varepsilon}, \alpha) \parallel^2_{\mathbb{C}} = \frac{1}{2} \left(1 - d(\alpha)\right)^2 \parallel \boldsymbol{\varepsilon} \parallel^2_{\mathbb{C}} \\ \psi_{non}(\boldsymbol{\nabla}\alpha) &= \frac{1}{2} \mu l^2 \parallel \boldsymbol{\nabla}\alpha \parallel^2 . \end{aligned} \tag{6.42}$$

In the above equation, the term $\parallel \boldsymbol{\varepsilon} \parallel^2_{\mathbb{C}}$ stands for the expression

$$\parallel \boldsymbol{\varepsilon} \parallel^2_{\boldsymbol{C}} \coloneqq \boldsymbol{\varepsilon} : \mathbb{C} : \boldsymbol{\varepsilon} \quad \text{with} \quad \mathbb{C} \coloneqq \lambda \boldsymbol{I} \otimes \boldsymbol{I} + 2\mu \mathbb{I}^S \tag{6.43}$$

Again, $\mathbb{I}^S$ and $\boldsymbol{I}$ are the fourth-order and second-order identity tensors, respectively. The fourth-order elasticity tensor $\mathbb{C}$ is defined via Lamés first parameter λ and the shear modulus μ.

For the description of the dissipative behavior, the concept of maximum dissipation outlined in Section 4.2.5 is applied. For the present material model it reads

$$\phi(\dot{\mathfrak{c}}, \mathfrak{c}) = \phi_{loc}(\dot{\alpha}, \alpha) = \sup_{\beta \in \mathbb{E}} \left[\beta \dot{\alpha} \right] \quad \text{with} \quad \mathbb{E} \coloneqq \{\beta \mid \varphi(\beta) \leq 0\} . \tag{6.44}$$

Note that the dissipation function ϕ is assumed to depend only on homogeneously distributed microscopic distortions characterized by α. The constitutive yield function is given in terms of the thermodynamic dissipative driving force β as

$$\varphi(\beta) = \beta - \psi_c \,, \tag{6.45}$$

where the *threshold energy* ψ_c represents the yield limit. Using the Lagrangian functional $\mathcal{L}(\alpha, \beta, \lambda) = \beta\dot{\alpha} - \lambda\varphi(\beta)$ with the Lagrange multiplier $\lambda \in \mathbb{R}$, the optimization problem given in Equation (6.44) is transformed into

$$\phi(\dot{\alpha}, \alpha) = \sup_{\beta,\, \lambda \geq 0} \left[\beta\dot{\alpha} - \lambda\varphi(\beta) \right] . \tag{6.46}$$

Since the first derivative of the yield function with respect to β evaluates as $\partial_\beta \varphi(\beta) = 1$, the Lagrange multiplier can be identified as $\lambda = \dot{\alpha}$. The *Karush–Kuhn–Tucker conditions* necessary for the existence of a solution to Equation (6.46) can be formulated as

$$\dot{\alpha} \geq 0 \,, \quad \varphi(\beta) \leq 0 \quad \text{and} \quad \dot{\alpha}\varphi(\beta) = 0 \,. \tag{6.47}$$

The fact that $\dot{\alpha}$ is non-negative implies that also the temporal change of the damage variable $\dot{d}(\dot{\alpha}, \alpha) = \nu \, (1 + \alpha)^{-\nu - 1} \, \dot{\alpha}$ is greater than zero at all times. This is in line with the assumption that reversible processes and self-healing are not considered within the present material model.

The next step towards a rate-dependent description is a viscous regularization of the yield function in the same way as in Section 4.2.5, leading to

$$\phi(\dot{\alpha}, \alpha) = \sup_{\beta} \left[\, \beta\dot{\alpha} \, - \frac{1}{2\eta} \left\langle \beta - \psi_c \right\rangle_+^2 \right] . \tag{6.48}$$

The evolution equation for α is obtain via differentiation with respect to β and reads

$$\dot{\alpha} = \frac{1}{\eta} \left\langle \beta - \psi_c \right\rangle_+ \,. \tag{6.49}$$

The definition of the ramp function $\langle (\cdot) \rangle_+ \coloneqq \frac{|(\cdot)| + (\cdot)}{2}$ indicates that the irreversibility constraint $\dot{\alpha} \geq 0$ stays fulfilled at all times.

6.3.3. Governing Balance Equations

The aim of this section is the derivation of the governing balance equations for a three-field rate-dependent damage formulation. They are obtained by exploiting the principle of virtual power introduced in Section 4.2.4.

The geometric and kinematic setup of a three-dimensional body is extensively described in Section 4.1.1. The solid under consideration occupies the domain $\mathcal{B} \subset \mathbb{R}^3$ with piece-wise smooth boundary $\partial\mathcal{B}$. The surface of the body is decomposed into two parts $\partial\mathcal{B}_{\boldsymbol{u}}$ and $\partial\mathcal{B}_{\boldsymbol{t}}$, where $\partial\mathcal{B}_{\boldsymbol{u}} \cap \partial\mathcal{B}_{\boldsymbol{t}} = \emptyset$. On the first one, Dirichlet boundary conditions $\boldsymbol{u} = \boldsymbol{u}_D$ are applied. On the latter, the macroscopic traction vector $\boldsymbol{t}_N$ is prescribed

Table 6.2.: Strong form of the governing balance equations for a three-field rate-dependent damage formulation

Macroscopic Balance Equations:

$$\begin{aligned} \boldsymbol{\nabla}\left(\left(1-d\left(\alpha\right)\right)^2\mathbb{C}:\boldsymbol{\varepsilon}\right)+\boldsymbol{\gamma}&=\boldsymbol{0} && \text{in } \mathcal{B}\\ \boldsymbol{u}&=\boldsymbol{u}_D && \text{on } \partial\mathcal{B}_{\boldsymbol{u}}\\ \left(\left(1-d\left(\alpha\right)\right)^2\mathbb{C}:\boldsymbol{\varepsilon}\right)\boldsymbol{n}&=\boldsymbol{t}_N && \text{on } \partial\mathcal{B}_{\boldsymbol{t}} \end{aligned}$$

Microscopic Balance Equations:

$$\begin{aligned} \mu l^2\Delta\alpha+\left(\left(1-d\left(\alpha\right)\right)d'(\alpha)\parallel\boldsymbol{\varepsilon}\parallel_{\mathbb{C}}^2-\beta\right)&=0 && \text{in } \mathcal{B}\\ \mu l^2\boldsymbol{\nabla}\alpha\cdot\boldsymbol{n}&=0 && \text{on } \partial\mathcal{B} \end{aligned}$$

Evolution Equation for the deterioration α:

$$\begin{aligned} \tfrac{1}{\eta}\left\langle\beta-\psi_c\right\rangle_+&=\dot{\alpha} && \text{in } \mathcal{B}\\ \alpha(\boldsymbol{x},t=t_0)&=0 && \text{in } \mathcal{B} \end{aligned}$$

in the form of a Neumann boundary condition. Regarding the deterioration α, the homogenous Neumann condition $\boldsymbol{\nabla}\alpha\cdot\boldsymbol{n}=0$ is applied on the whole boundary $\partial\mathcal{B}$. Hence, there is no need to prescribe microscopic displacements.

The principle of virtual power, generally given in Equation (4.24), is specified for the extended constitutive state (6.37) as

$$\mathcal{E}(\dot{\boldsymbol{u}},\dot{\alpha},\boldsymbol{u},\alpha)+\mathcal{D}(\dot{\alpha},\beta)-\mathcal{P}_{ext}(\dot{\boldsymbol{u}})=0 \tag{6.50}$$

The power of energy storage mechanisms $\mathcal{E}$ is given in a universal manner in Equation (4.19). Inserting the function ψ from Equation (6.41) leads to

$$\begin{aligned} \mathcal{E}(\dot{\boldsymbol{u}},\dot{\alpha},\boldsymbol{u},\alpha)&=\int_{\mathcal{B}}\partial_{\boldsymbol{\mathfrak{c}}}\psi\cdot\dot{\boldsymbol{\mathfrak{c}}}\,dV\\ &=\int_{\mathcal{B}}\left(-\boldsymbol{\nabla}\left[\left(1-d(\alpha)\right)^2\mathbb{C}:\boldsymbol{\varepsilon}\right]\cdot\dot{\boldsymbol{u}}\right)\,dV\\ &-\int_{\mathcal{B}}\left[\left(1-d(\alpha)\right)d'(\alpha)\parallel\boldsymbol{\varepsilon}\parallel_{\mathbb{C}}^2+\mu l^2\Delta\alpha\right]\dot{\alpha}\,dV\\ &+\int_{\partial\mathcal{B}_{\boldsymbol{t}}}\left[\left(1-d(\alpha)\right)^2\mathbb{C}:\boldsymbol{\varepsilon}\right]\boldsymbol{n}\cdot\dot{\boldsymbol{u}}\,dA+\int_{\partial\mathcal{B}}\mu l^2\boldsymbol{\nabla}\alpha\cdot\boldsymbol{n}\dot{\alpha}\,dA\,. \end{aligned} \tag{6.51}$$

The dissipation functional introduced in Equation (4.20) reads

$$\mathcal{D}(\dot{\alpha},\beta)=\int_{\mathcal{B}}\mathfrak{f}\cdot\dot{\boldsymbol{\mathfrak{c}}}\,dV=\int_{\mathcal{B}}\beta\dot{\alpha}\,dV\,. \tag{6.52}$$

Note that the thermodynamic dissipative driving forces $\bar{\boldsymbol{\mathcal{F}}}$ and $\check{\boldsymbol{\mathcal{F}}}$ dual to the variables $\dot{\boldsymbol{\varepsilon}}$ and $\boldsymbol{\nabla}\dot{\alpha}$ are neglected. The external mechanical power is characterized by the volume force field $\boldsymbol{\gamma}$ and the macroscopic traction vector $\boldsymbol{t}_N$. Since microstructural force fields and traction vectors are not considered, it can be written as

$$\mathcal{P}_{ext}(\dot{\boldsymbol{u}}) = \int_{\mathcal{B}} \boldsymbol{\gamma} \cdot \dot{\boldsymbol{u}} \, dV + \int_{\partial\mathcal{B}_t} \boldsymbol{t}_N \cdot \dot{\boldsymbol{u}} \, dA \,. \tag{6.53}$$

The governing balance Equations for a three-field rate-dependent damage formulation are obtained by inserting Equations (6.51)–(6.53) into the principle of virtual power (6.50). They are depicted in Table 6.2. The initial condition $\alpha(\boldsymbol{x}, t = 0) = 0$ follows from the fact that the material is undamaged at the beginning of the computation.

6.3.4. Incremental Variational Principle

An alternative formulation is provided by applying the incremental variational principle introduced in Section 4.3.3. It is well-suited for a numerical treatment with the finite element method. Again, a three-field rate-dependent approach is chosen. The time interval $\mathcal{T} = [t_0, t_m] \in \mathbb{R}_0^+$ under consideration is divided into m equidistant time steps of length

$$\tau = \frac{t_m - t_0}{m} \,. \tag{6.54}$$

All quantities of interest are evaluated at discrete points $t_0, t_1, \ldots, t_n, t_{n+1}, \ldots, t_m$ only. The state of any variable at the current time t_n is written as

$$(\cdot)_n \coloneqq (\cdot)(\boldsymbol{x}, t_n) \tag{6.55}$$

and is assumed to be known.

The extended incremental internal work density $\pi_\eta^{*\tau}$ is defined in a general manner in Equation (4.47). For the present material model it is obtained by inserting the energy storage function ψ from Equation (6.41) and the yield function ϕ from Equation (6.45), leading to

$$\begin{aligned} \pi_\eta^{*\tau}(\mathfrak{c}^*, \mathfrak{c}_n^*) = \frac{1}{2}\left(1 - d(\alpha)\right)^2 \| \boldsymbol{\varepsilon} \|_{\mathbb{C}}^2 + \frac{1}{2}\mu l^2 \| \boldsymbol{\nabla}\alpha \|^2 - \psi\left(\mathfrak{c}_n\right) \\ + \beta\left(\alpha - \alpha_n\right) - \frac{\tau}{2\eta}\left\langle \beta - \psi_c \right\rangle_+^2 \,. \end{aligned} \tag{6.56}$$

Inserting this expression into Equation (4.48) results in the extended incremental potential

$$\Pi_\eta^{*\tau}(\mathfrak{u}^*) = \int_{\mathcal{B}} \left[\pi_\eta^{*\tau}(\mathfrak{c}^*, \mathfrak{c}_n^*) - \boldsymbol{\gamma} \cdot (\boldsymbol{u} - \boldsymbol{u}_n)\right] dV - \int_{\partial\mathcal{B}_t} \boldsymbol{t}_N \cdot (\boldsymbol{u} - \boldsymbol{u}_n) \, dA \,. \tag{6.57}$$

Note that, as in the previous section, microscopic volume forces and tractions vectors are neglected. The unknown generalized deformation vector $\mathfrak{u}^* = \{\boldsymbol{u}, \alpha, \beta\}$ is now obtained

Table 6.3.: Time-discrete Euler equations for a variational three-field rate-dependent damage formulation

Macroscopic Balance Equations:

$$\begin{aligned} \boldsymbol{\nabla}\left(\left(1-d\left(\alpha\right)\right)^2\mathbb{C}:\boldsymbol{\varepsilon}\right)+\boldsymbol{\gamma}&=\boldsymbol{0} && \text{in } \mathcal{B}\\ \boldsymbol{u}&=\boldsymbol{u}_D && \text{on } \partial\mathcal{B}_{\boldsymbol{u}}\\ \left(\left(1-d\left(\alpha\right)\right)^2\mathbb{C}:\boldsymbol{\varepsilon}\right)\boldsymbol{n}&=\boldsymbol{t}_N && \text{on } \partial\mathcal{B}_{\boldsymbol{t}} \end{aligned}$$

Microscopic Balance Equations:

$$\begin{aligned} \mu l^2\Delta\alpha+\left(\left(1-d\left(\alpha\right)\right)d'(\alpha)\parallel\boldsymbol{\varepsilon}\parallel_{\mathbb{C}}^2-\beta\right)&=0 && \text{in } \mathcal{B}\\ \mu l^2\boldsymbol{\nabla}\alpha\cdot\boldsymbol{n}&=0 && \text{on } \partial\mathcal{B} \end{aligned}$$

Evolution Equation for the deterioration α:

$$\begin{aligned} \alpha_n+\tfrac{\tau}{\eta}\left\langle\beta-\psi_c\right\rangle_+&=\alpha && \text{in } \mathcal{B}\\ \alpha_0&=0 && \text{in } \mathcal{B} \end{aligned}$$

by applying the extended rate-dependent incremental stationary principle

$$\{\boldsymbol{u},\alpha,\beta\}=\arg\left\{\inf_{\boldsymbol{u}}\inf_{\alpha}\sup_{\beta}\,\Pi_\eta^{*\tau}(\boldsymbol{u},\alpha,\beta)\right\}. \tag{6.58}$$

Since Equation (6.58) represents a saddle point problem, the linear system of equations resulting from a finite element discretization will be indefinite. This has to be considered when a solver for said system of equations is chosen, since many iterative solvers require positive-definiteness. The necessary condition associated with Equation (6.58) reads

$$D\Pi_\eta^{*\tau}[\delta\mathbf{u}^*]=D\Pi_\eta^{*\tau}[\delta\boldsymbol{u}]+D\Pi_\eta^{*\tau}[\delta\alpha]+D\Pi_\eta^{*\tau}[\delta\beta]=0\,. \tag{6.59}$$

The individual terms of the above equations are identified as

$$\begin{aligned} D\Pi_\eta^{*\tau}[\delta\boldsymbol{u}]&=\int_{\mathcal{B}}\left[\left(1-d(\alpha)\right)^2\boldsymbol{\varepsilon}:\mathbb{C}:\delta\boldsymbol{\varepsilon}-\boldsymbol{\gamma}\cdot\delta\boldsymbol{u}\right]\,dV-\int_{\partial\mathcal{B}_{\boldsymbol{t}}}\boldsymbol{t}_N\cdot\delta\boldsymbol{u}\,dA\\ D\Pi_\eta^{*\tau}[\delta\alpha]&=\int_{\mathcal{B}}\left[\mu l^2\boldsymbol{\nabla}\alpha\cdot\boldsymbol{\nabla}\delta\alpha-\left(\left(1-d\left(\alpha\right)\right)d'(\alpha)\parallel\boldsymbol{\varepsilon}\parallel_{\mathbb{C}}^2-\beta\right)\cdot\delta\alpha\right]\,dV\\ D\Pi_\eta^{*\tau}[\delta\beta]&=\int_{\mathcal{B}}\left[\alpha-\alpha_n-\frac{\tau}{\eta}\left\langle\beta-\psi_c\right\rangle_+\right]\delta\beta\,dV\,, \end{aligned} \tag{6.60}$$

where the admissible variations $\delta\boldsymbol{u}\in\mathcal{W}_{\boldsymbol{u}}^0$, $\delta\alpha\in\mathcal{W}_\alpha^0$ and $\delta\beta\in\mathcal{L}_2$ come from the function spaces introduced in Equation (4.26). The according Euler equations can be obtained by applying Gauß' integration theorem and are displayed in Table 6.3.

6.3.5. Finite Element Discretization

The variational problem defined in the previous section is discretized using the finite element method. A general approach for gradient-type dissipative solids is performed in Section 5.2.

In a three-dimensional setting, the generalized deformation vector reads

$$\mathfrak{u}^* \coloneqq \{u_1,\ u_2,\ u_3,\ \alpha,\ \beta\}\,. \tag{6.61}$$

The extended generalized constitutive state is written in Voigt notation as

$$\mathfrak{c}^* \coloneqq \{u_{1,1},\ u_{2,2},\ u_{3,3},\ u_{2,3}{+}u_{3,2},\ u_{3,1}{+}u_{1,3},\ u_{1,2}{+}u_{2,1},\ \alpha,\ \alpha_{,1},\ \alpha_{,2},\ \alpha_{,3},\ \beta\}\,. \tag{6.62}$$

The nodal values of the extended generalized deformation vector are summarized in the vector $\mathfrak{d}_i^* \coloneqq \begin{bmatrix} d_1 & d_2 & d_3 & a & b \end{bmatrix}_i^T$. The displacements $\boldsymbol{u}$ and the deterioration α are interpolated using the shape functions $N_i = \bar{N}_i = \check{N}_i$. The extended interpolation matrix $[\mathfrak{N}^*]_i^e$ is then given on element level in accordance with Equation (5.24), yielding

$$\mathfrak{u}^{*h} = \mathfrak{N}^*(\boldsymbol{x})\mathfrak{d}^* \quad \text{with} \quad [\mathfrak{N}^*]_i^e = \begin{bmatrix} N\boldsymbol{I}_{3\times 3} & \boldsymbol{0} & \boldsymbol{0} \\ \boldsymbol{0} & N & 0 \\ \boldsymbol{0} & 0 & M \end{bmatrix}_i . \tag{6.63}$$

For a hexahedral Lagrange element of order one, the shape functions result from an extension of Equation (5.8) by the third dimension, leading to

$$\begin{aligned} N_1(\boldsymbol{\xi}) &= \frac{1}{8}(1+\xi_1)(1+\xi_2)(1+\xi_3) & N_5(\boldsymbol{\xi}) &= \frac{1}{8}(1-\xi_1)(1+\xi_2)(1+\xi_3) \\ N_2(\boldsymbol{\xi}) &= \frac{1}{8}(1+\xi_1)(1+\xi_2)(1-\xi_3) & N_6(\boldsymbol{\xi}) &= \frac{1}{8}(1-\xi_1)(1+\xi_2)(1-\xi_3) \\ N_3(\boldsymbol{\xi}) &= \frac{1}{8}(1+\xi_1)(1-\xi_2)(1+\xi_3) & N_7(\boldsymbol{\xi}) &= \frac{1}{8}(1-\xi_1)(1-\xi_2)(1+\xi_3) \\ N_4(\boldsymbol{\xi}) &= \frac{1}{8}(1+\xi_1)(1-\xi_2)(1-\xi_3) & N_8(\boldsymbol{\xi}) &= \frac{1}{8}(1-\xi_1)(1-\xi_2)(1-\xi_3) \end{aligned} \tag{6.64}$$

where $\boldsymbol{\xi} = \begin{bmatrix} \xi_1 & \xi_2 & \xi_3 \end{bmatrix}^T$ are the natural coordinates of the reference cell. Here, the thermodynamic driving force β is also approximated with these functions, meaning $M_i = N_i$. The extended constitutive state is interpolated as

$$\mathfrak{c}^{*h} = \mathfrak{B}^*\mathfrak{d}^* \quad \text{with} \quad [\mathfrak{B}^*]_i^e = \begin{bmatrix} N_{,1} & 0 & 0 & 0 & N_{,3} & N_{,2} & 0 & 0 & 0 & 0 & 0 \\ 0 & N_{,2} & 0 & N_{,3} & 0 & N_{,1} & 0 & 0 & 0 & 0 & 0 \\ 0 & 0 & N_{,3} & N_{,2} & N_{,1} & 0 & 0 & 0 & 0 & 0 & 0 \\ 0 & 0 & 0 & 0 & 0 & 0 & N & N_{,1} & N_{,2} & N_{,3} & 0 \\ 0 & 0 & 0 & 0 & 0 & 0 & 0 & 0 & 0 & 0 & M \end{bmatrix}_i^T . \tag{6.65}$$

The extended generalized stresses $\boldsymbol{S}^*$ and extended generalized moduli $\boldsymbol{C}^*$ introduced in Section 5.2 remain to be determined. They are calculated by taking the first and

second derivative of the $\pi_\eta^{*\tau}$ given in Equation (6.56) with respect to the constitutive state, resulting in

$$\boldsymbol{S}^* = \begin{bmatrix} \partial_{\boldsymbol{\varepsilon}} \pi_\eta^{*h} \\ \partial_\alpha \pi_\eta^{*h} \\ \partial_{\boldsymbol{\nabla}\alpha} \pi_\eta^{*h} \\ \partial_\beta \pi_\eta^{*h} \end{bmatrix} \quad \text{and} \quad \boldsymbol{C}^* = \begin{bmatrix} \partial^2_{\boldsymbol{\varepsilon}\boldsymbol{\varepsilon}} \pi_\eta^{*h} & \partial^2_{\boldsymbol{\varepsilon}\alpha} \pi_\eta^{*h} & \mathbf{0} & \mathbf{0} \\ \partial^2_{\boldsymbol{\varepsilon}\alpha} \pi_\eta^{*h} & \partial^2_{\alpha\alpha} \pi_\eta^{*h} & \mathbf{0} & 1 \\ \mathbf{0} & \mathbf{0} & \partial^2_{\boldsymbol{\nabla}\alpha\boldsymbol{\nabla}\alpha} \pi_\eta^{*h} & \mathbf{0} \\ \mathbf{0} & 1 & \mathbf{0} & \partial^2_{\beta\beta} \pi_\eta^{*h} \end{bmatrix} . \tag{6.66}$$

Their respective entries read

$$\begin{aligned} \partial_{\boldsymbol{\varepsilon}} \pi_\eta^{*h} &= (1 - d(\alpha))^2 \, \mathbb{C} : \boldsymbol{\varepsilon} \\ \partial_\alpha \pi_\eta^{*h} &= -(1 - d(\alpha)) \, d'(\alpha) \, \| \boldsymbol{\varepsilon} \|^2_{\mathbb{C}} + \beta \\ \partial_{\boldsymbol{\nabla}\alpha} \pi_\eta^{*h} &= \mu l^2 \boldsymbol{\nabla} \alpha \\ \partial_\beta \pi_\eta^{*h} &= \alpha - \alpha_n - \frac{\tau}{\eta} \langle \beta - \psi_c \rangle_+ \end{aligned} \tag{6.67}$$

and

$$\begin{aligned} \partial^2_{\boldsymbol{\varepsilon}\boldsymbol{\varepsilon}} \pi_\eta^{*h} &= (1 - d(\alpha))^2 \, \mathbb{C} \\ \partial^2_{\alpha\alpha} \pi_\eta^{*h} &= \left[d'^2(\alpha) - (1 - d(\alpha)) \, d''(\alpha) \right] \| \boldsymbol{\varepsilon} \|^2_{\mathbb{C}} \\ \partial^2_{\boldsymbol{\varepsilon}\alpha} \pi_\eta^{*h} &= -2 (1 - d(\alpha)) \, d'(\alpha) \mathbb{C} : \boldsymbol{\varepsilon} \\ \partial^2_{\boldsymbol{\nabla}\alpha\boldsymbol{\nabla}\alpha} \pi_\eta^{*h} &= \mu l^2 \boldsymbol{I} \\ \partial^2_{\beta\beta} \pi_\eta^{*h} &= -\frac{\tau}{2\eta} \left(1 + \operatorname{sign}(\beta - \psi_c) \right) . \end{aligned} \tag{6.68}$$

7. Numerical Examples

In this chapter, two numerical examples are computed in order to show the benefits of the introduced gradient-extended method. Both of them are taken from WELSCHINGER [25].

For each problem numerical solutions are obtained at three different mesh densities. Subsequently, the results of the local and the non-local approach are compared regarding mesh size dependency. In the first example, a shear test is performed on a three-dimensional rectangular specimen. The second one is a tensile test of a two-dimensional rectangular plate. In both cases, the test is driven by Dirichlet boundary conditions with constant increment. The parameters of the material are given in Table 7.1. The finite

Table 7.1.: Material parameters used for the numerical computations.

λ	First Lamé parameter	121.15	$\mathrm{kN/mm^2}$
μ	Shear modulus	80.77	$\mathrm{kN/mm^2}$
ψ_c	Threshold energy	8.08×10^{-3}	$\mathrm{kN/mm^2}$
η	Viscosity	1×10^{-6}	$\mathrm{kN\,s/mm^2}$

element interpolation is conducted using the hexahedral Lagrange elements of order one described in Section 6.3.5.

The implementation mainly bases on the C++ software library deal.II developed by BANGERTH et al. [1]. The linear systems of equations were solved using an LU factorization provided by the UMFPACK software library.

7.1. Shear Test of Squared Specimen

The first numerical example is a three-dimensional rectangular solid under shear load. The geometric setup is shown in Figure 7.1. In z-direction – perpendicular to the drawing plane – the body is discretized using one layer of elements with a thickness of 1 mm. In the xy-plane, three different discretizations with 9×9, 19×19 and 29×29 spatial elements are examined. This leads to meshes with 200, 800 and 1800 nodes respectively.

The boundary conditions are depicted in Figure 7.1. In addition to the visualized constraints, the displacements in y-direction are set to zero at all nodes to obtain a state of pure shear. Furthermore, all displacements in z-direction are locked in order to mimic plane strain behavior. At the uppermost row of nodes, displacements in x-direction are prescribed with a constant increment of $\Delta u = 1 \times 10^{-3}\,\mathrm{mm}$. The time increment is set to a constant value of $\tau = 5 \times 10^{-6}\,\mathrm{s}$. Altogether, 500 time increments are performed, resulting in a final displacement of the top boundary of $u_{fin} = 0.5\,\mathrm{mm}$ after

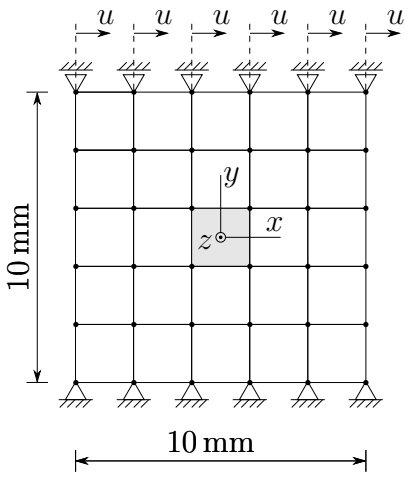

Figure 7.1.: Finite element mesh of a squared specimen under shear load. Localization is triggered in the central cell, where the threshold energy ψ_c is reduced by 5 %. Additionally to the visualized constraints, the displacements in y- and z-direction are locked at all nodes.

2.5×10^{-3} seconds. The material parameters are given in Table 7.1. The parameter of the damage function $d(\alpha) = 1 - (1 + \alpha)^{-\nu}$ is set to $\nu = 1.2$. Furthermore, the threshold energy ψ_c is reduced by 5 % in the central cell in order to trigger localization.

The results of the numerical computations are shown in Figure 7.2, where the resulting force in x-direction at the bottom boundary is plotted over the displacement in x-direction on the top boundary. The outcome of the local calculations with length scale parameter $l = 0.000\,\text{mm}$ are displayed in Figure 7.2a. Clearly, the solution depends on the number of elements. The non-local simulations with $l = 0.012\,\text{mm}$, on the contrary, deliver results independent of the mesh size.

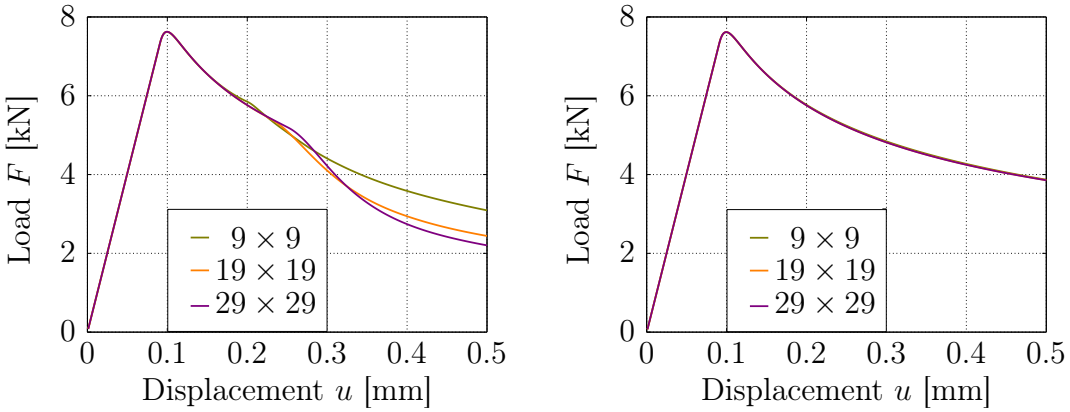

Figure 7.2.: Load-displacement curve for (a) the local theory with $l = 0.000\,\text{mm}$ and (b) the non-local theory with $l = 0.012\,\text{mm}$ for 9×9, 19×19 and 29×29 elements respectively.

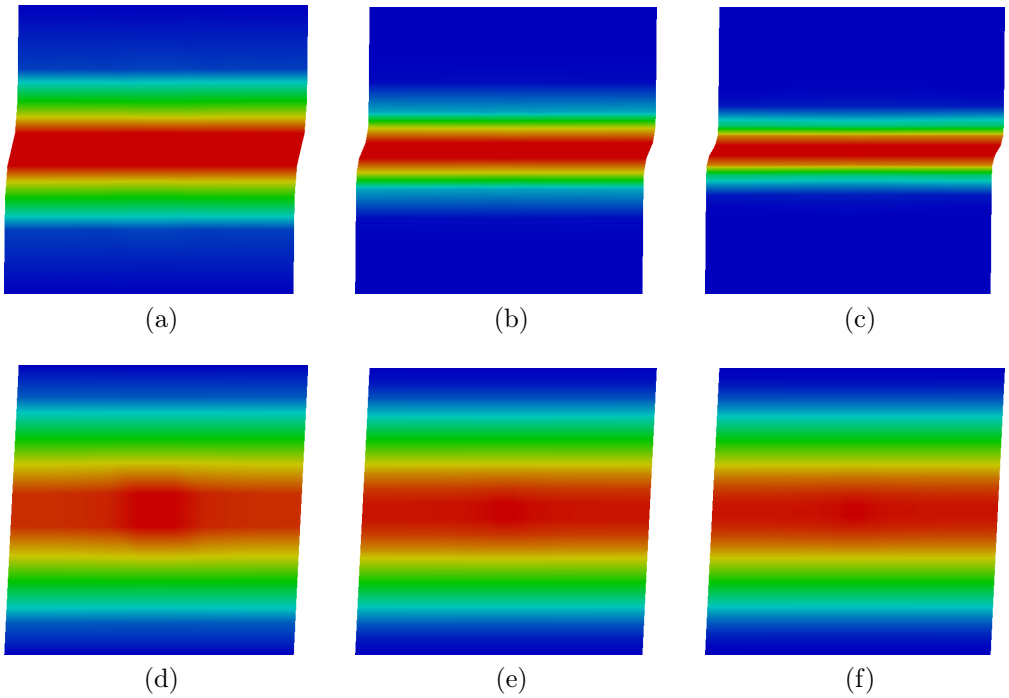

Figure 7.3.: Contour plots of the damage variable d at $u = 0.5\,\text{mm}$ over the squared specimen for (a)-(c) $l = 0.000\,\text{mm}$ and (d)-(f) $l = 0.012\,\text{mm}$. The number of elements is (a)(d) 9×9, (b)(e) 19×19 and (c)(f) 29×29 respectively.

The distribution of the damage variable d for the local approach is shown in Figures 7.3a–7.3c. Obviously, the width of the shear bands depends on the mesh size and localization occurs. This can also be seen in Figures 7.4a–7.4c, where the deformed meshes at the end of the simulation are illustrated.

Remark. While the local solution shown in Figure 7.2a behaves as expected at the final state $u = u_{fin} = 0.5\,\text{mm}$, the course of the curves between $u = 0.1\,\text{mm}$ and $u = 0.3\,\text{mm}$ must be looked at critically. An advanced simulation using an arc-length method (Riks method) would be able to describe snap-back behavior and may deliver more accurate results.

Remark. The strong gradient $\partial u/\partial y$ in the localization zones of the solutions shown in Figures 7.3a–7.3c indicates that the assumption of small deformations is, in fact, not valid. A quantitatively exact investigation must consider geometric nonlinearities.

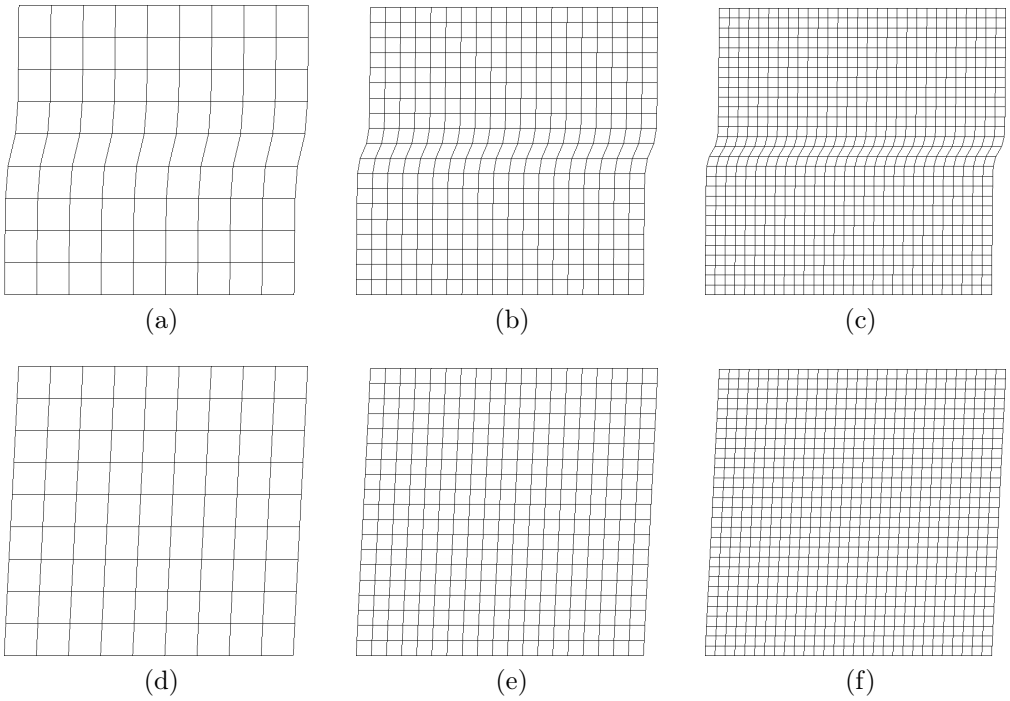

Figure 7.4.: Deformed meshes of the squared specimen under shear load at $u = 0.5\,\text{mm}$ for (a)-(c) $l = 0.000\,\text{mm}$ and (d)-(f) $l = 0.012\,\text{mm}$. The number of elements is (a)(d) 9×9, (b)(e) 19×19 and (c)(f) 29×29 respectively.

7.2. Tensile Test of Rectangular Specimen

The second example is a two-dimensional rectangular plate under tensile load as displayed in Figure 7.5a. Because of the symmetries of the solid, only the upper right quarter system shown in Figure 7.5b is considered. Three different discretizations using 9×20, 18×40 and 36×80 spatial elements are examined.

The boundary conditions are visualized in Figure 7.5b. At the uppermost row of nodes, displacements in y-direction are prescribed with a constant increment $\Delta u = 5 \times 10^{-3}\,\text{mm}$. A constant time increment $\tau = 1 \times 10^{-4}\,\text{s}$ is chosen, leading to a total number of 400 increments after $4 \times 10^{-2}\,\text{seconds}$. Hence, the final displacement of the top boundary is $u_{fin} = 2.0\,\text{mm}$. The material parameters are given in Table 7.1. The parameter controlling the damage function $d(\alpha)$ is set to $\nu = 0.6$. Since the entire body shall be weakened in its center, the threshold energy ψ_c is reduced by 5 % in the lower left cell of the discretized quarter system.

The results of the numerical computations are depicted in Figure 7.6, where the resulting force in y-direction at the bottom boundary is plotted over the displacement in y-direction on the top boundary. The outcome of the local calculations with length scale parameter $l = 0.000\,\text{mm}$ are displayed in Figure 7.6a. Again, the solution depends on the mesh size. The results of the non-local simulations with $l = 0.003\,\text{mm}$ do not indicate mesh size dependency.

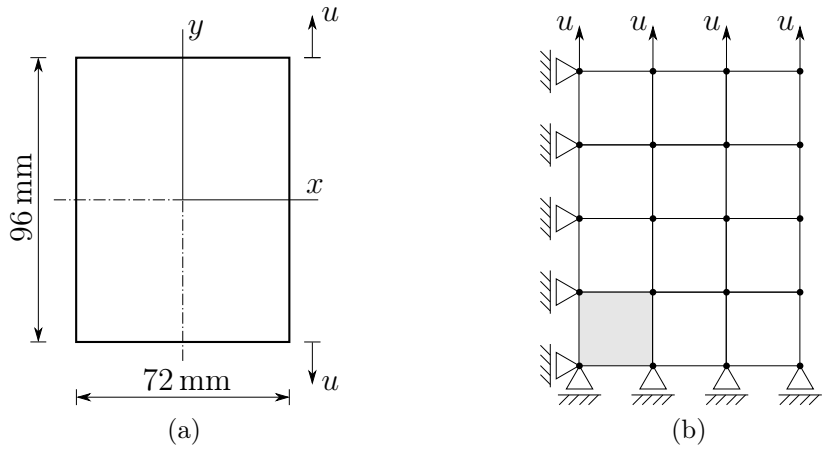

Figure 7.5.: (a) Geometry of a rectangular specimen under tensile load and (b) finite element mesh of the upper right quarter system. The threshold energy ψ_c is reduced by 5 % in the bottom left cell in order to trigger localization.

The distribution of the damage variable d for the local approach is shown in Figures 7.7a–7.7c. The width of the shear bands depends on the mesh size and localization occurs. This is also shown in Figures 7.8a–7.8c, where the deformed meshes are illustrated for $u = u_{fin} = 2.0\,\text{mm}$.

Remark. As in the previous example, the local solution shown in Figure 7.6a behaves as expected at the final state $u = u_{fin} = 2.0\,\text{mm}$. However, the course of the curves between $u = 0.35\,\text{mm}$ and $u = 0.7\,\text{mm}$ seems to be unrealistic. Again, an advanced simulation using an arc-length method would be able to describe snap-back behavior and deliver more accurate results.

Remark. The orientation of the shear bands is not well-aligned with the finite element mesh orientation. This results in an unphysical solution, as indicated by the zig-zag patterns visible in the contour plots of the damage variable d (Figure 7.7). An advanced simulation using strain-enhanced finite elements would be able to describe a more realistic behavior.

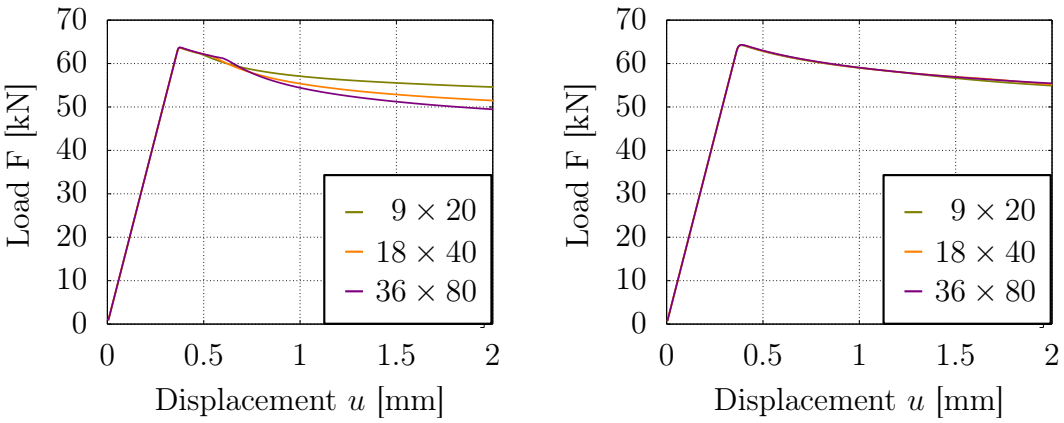

Figure 7.6.: Load-displacement curve for (a) the local theory with $l = 0.000\,\text{mm}$ and (b) the non-local theory with $l = 0.003\,\text{mm}$ for 9×20, 18×40 and 36×80 elements respectively.

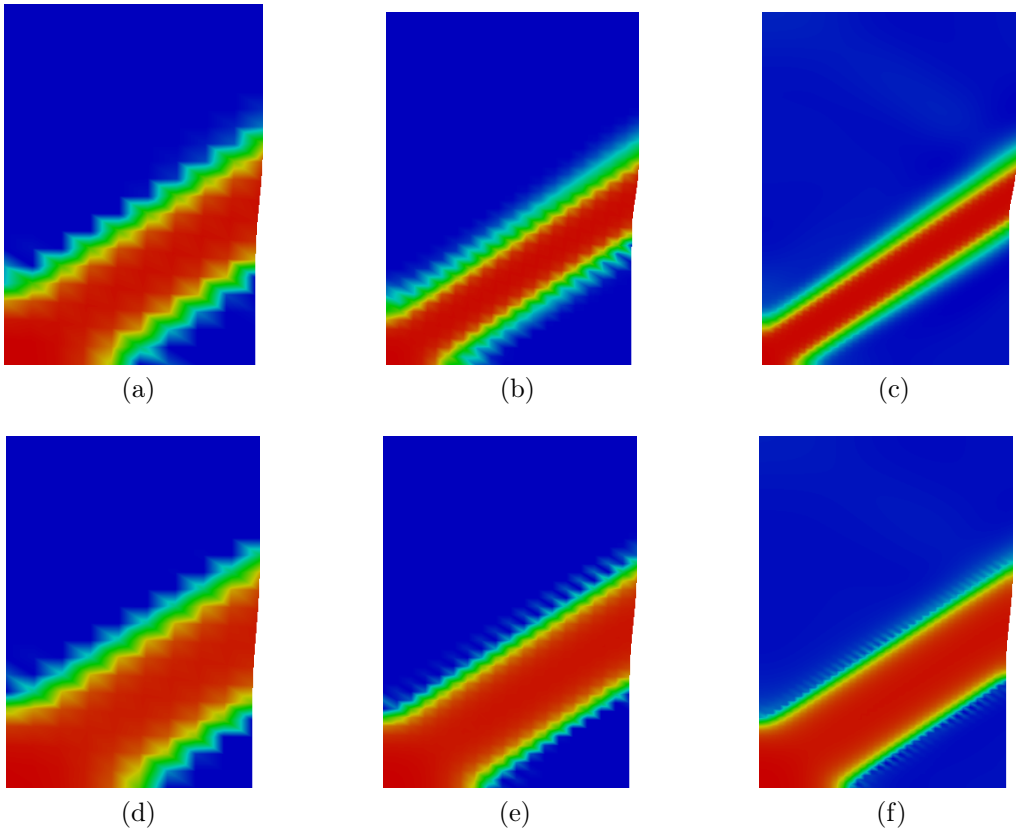

Figure 7.7.: Contour plots of the damage variable d at $u = 2.0\,\text{mm}$ over the rectangular quarter system for (a)-(c) $l = 0.000\,\text{mm}$ and (d)-(f) $l = 0.003\,\text{mm}$. The number of elements is (a)(d) $9{\times}20$, (b)(e) $18{\times}40$ and (c)(f) $36{\times}80$ respectively.

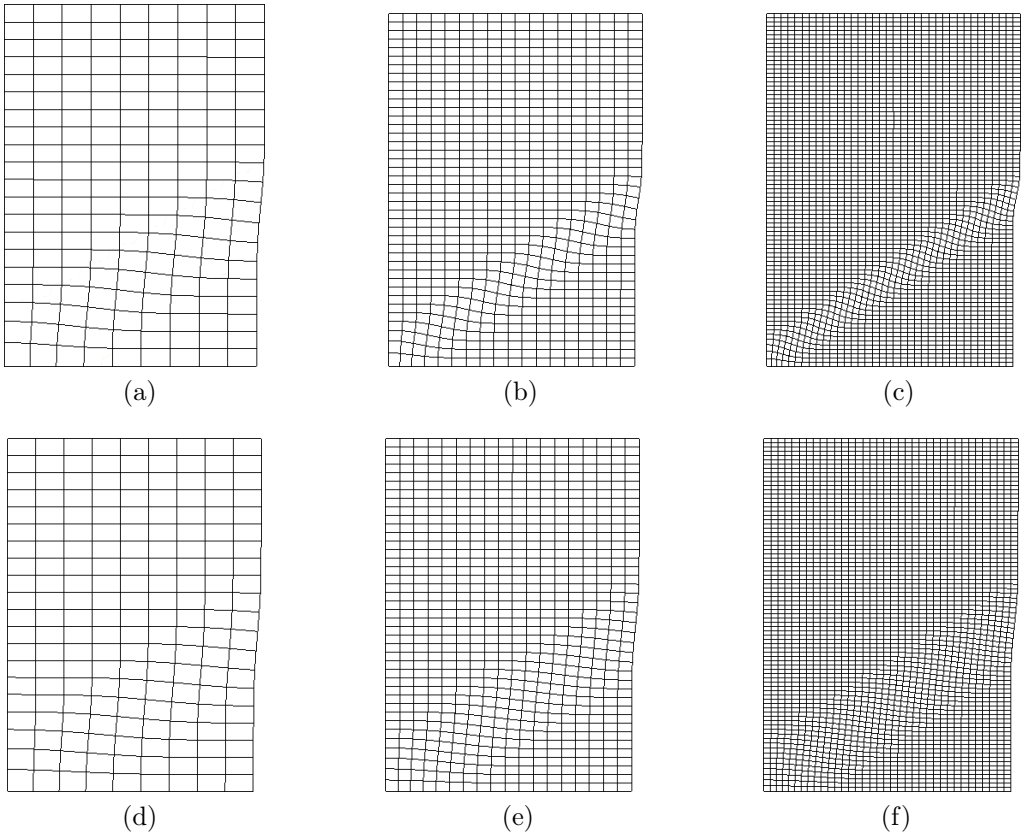

Figure 7.8.: Deformed meshes of the rectangular quarter system under tensile load at $u = 2.0\,\text{mm}$ for (a)-(c) $l = 0.000\,\text{mm}$ and (d)-(f) $l = 0.003\,\text{mm}$. The number of elements is (a)(d) 9×20, (b)(e) 18×40 and (c)(f) 36×80 respectively.

A. Mathematical Complements

Section A.1 represents an excerpt from Braess [6, p. 28f] and introduces the Sobolev spaces needed for weak formulations of partial differential equations, for example the variational principle.

A.1. Function Spaces in Finite Element Methods

Let the set $\Omega \in \mathbb{R}^n$ be an open subset of the n-dimensional Euclidean space. The function space $\mathcal{L}_2(\Omega)$ contains all functions $u(x) : \Omega \mapsto \mathbb{R}$ with $x \in \Omega$ for which the $\mathcal{L}_2$ norm

$$\| u \|_2 \coloneqq \left(\int_\Omega |u(x)|^2 \, dx \right)^{1/2} \tag{A.1}$$

exists and is finite. $\mathcal{L}_2$ represents a Hilbert space with respect to the norm $\| (\cdot) \|_2$. A scalar product between $u(x)$ and a second function $v(x) : \Omega \mapsto \mathbb{R}$ is defined as

$$(u, v)_0 \coloneqq \int_\Omega u(x) v(x) \, dx \, . \tag{A.2}$$

The *weak derivative* $w = \partial_\alpha u$ in $\mathcal{L}_2$ is defined via the relationship

$$(\phi, u)_0 = (-1)^{|\alpha|} (\partial_\alpha \phi, u)_0 \quad \text{for all} \quad \phi \in \mathcal{C}_0^\infty(\Omega) \, , \tag{A.3}$$

with $\mathcal{C}^\infty(\Omega)$ being the space of infinitely differentiable functions, $\mathcal{C}_0^\infty(\Omega)$ the subspace of these functions which are nonzero only on a compact subset of Ω, and $\partial_\alpha(\phi)$ the classic derivative of ϕ of order α. If $u(x)$ is differentiable, its classic derivative coincides with the introduced weak derivative.

The *Sobolev space* $\mathcal{H}^m$ with $m \geq 0$ is defined as the set of all functions $u \in \mathcal{L}_2(\Omega)$ which possess weak derivatives $\partial_\alpha u$ for all $|\alpha| \leq m$. A scalar product on $\mathcal{H}^m$ can be defined as

$$(u, v)_m \coloneqq \sum_{|\alpha| \leq m} (\partial_\alpha u, \partial_\alpha v)_0 \, . \tag{A.4}$$

$\mathcal{H}^m$ is complete with respect to the norm

$$\| u \|_m \coloneqq \left(\sum_{|\alpha| \leq m} \| \partial_\alpha u \|^2_{\mathcal{L}_2(\Omega)} \right)^{1/2} , \tag{A.5}$$

and therefore is a Hilbert space.

Note that all considerations of this section can be made for general Lebesgue spaces $\mathcal{L}_p$ with $p \neq 2$, as well as for vector-valued functions $\boldsymbol{u}(x), \boldsymbol{v}(x) : \mathbb{R}^n \mapsto \mathbb{R}^d$ with $d > 1$, analogously.

Bibliography

[1] Bangerth, W., Hartmann, R. & Kanschat, G. "deal.II – a General Purpose Object Oriented Finite Element Library". In: *ACM Trans. Math. Softw.* 33.4 (2007), pp. 24/1–24/27.

[2] Başar, Y. & Weichert, D. *Nonlinear Continuum Mechanics of Solids*. Springer, 2000.

[3] Bathe, K.-J. *Finite Element Procedures*. Prentice-Hall, Inc., 1996.

[4] Biot, M. A. *Mechanics of Incremental Deformations*. John Wiley & Sons, Inc., 1965.

[5] Bonet, J. & Wood, R. D. *Nonlinear Continuum Mechanics for Finite Element Analysis*. 2nd ed. Cambridge University Press, 2008.

[6] Braess, D. *Finite Elements. Theory, Fast Solvers, and Applications in Elasticity Theory*. Cambridge University Press, 2007.

[7] Burg, K., Haf, H., Wille, F. & Meister, A. *Höhere Mathematik für Ingenieure. Band I: Analysis*. 2nd ed. Springer, 2013.

[8] Cosmol, P. *Methoden zur numerischen Behandlung nichtlinearer Gleichungen und Optimierungsaufgaben*. 2nd ed. Teubner, 1993.

[9] De Borst, R. "Computation of Post-Bifurcation and Post-Failure Behavior of Strain-Softening Solids". In: *Computers & Structures* 25.2 (1986), pp. 211–224.

[10] De Borst, R. "Damage, Material Instabilities, and Failure". In: *Encyclopedia of Computational Mechanics*. Ed. by Stein, E., De Borst, R. & Hughes, T. J. R. Vol. 2. John Wiley & Sons, 2004, pp. 335–373.

[11] Gurtin, M. E., Fried, E. & Anand, L. *The Mechanics and Thermodynamics of Continua*. 3rd ed. Cambridge University Press, 2010.

[12] Hill, R. "A general theory of uniqueness and stability in elastic-plastic solids". In: *Journal of the Mechanics and Physics of Solids* 6 (1958), pp. 236–249.

[13] Hughes, T. J. R. *The Finite Element Method. Linear Static and Dynamic Finite Element Analysis*. Prentice-Hall, Inc., 1987.

[14] Lemaitre, J. *A Course on Damage Mechanics. Ductile, Creep, Fatigue and Brittle Fractures*. Springer, 2005.

[15] Lemaitre, J. & Desmorat, R. *Engineering Damage Mechanics*. Springer, 1996.

[16] Marsden, J. E. & Hughes, T. J. R. *Mathematical Foundations of Elasticity*. Prentice-Hall, Inc., 1983.

[17] Miehe, C. "A multi-field incremental variational framework for gradient-extended standard dissipative solids". In: *Journal of the Mechanics and Physics of Solids* 59 (2010), pp. 898–923.

[18] Neilsen, M. K. & Schreyer, H. L. "Bifurcations in elastic-plastic materials". In: *International Journal of Solids and Structures* 30.4 (1992), pp. 521–544.

[19] Nguyen, Q.-S. & Andrieux, S. "The non-local generalized standard approach: a consistent gradient theory". In: *Comptes Rendus Mecanique* 333 (2005), pp. 139–145.

[20] Schreyer, H. L. & Chen, Z. "One-Dimensional Softening With Localization". In: *International Journal of Solids and Structures* 53 (1986), pp. 791–797.

[21] Simo, J. C. & Ju, J. W. "Strain- and Stress-Based Continuum Damage Models - I. Formulation". In: *International Journal of Solids and Structures* 23.7 (1987), pp. 821–840.

[22] Sokolnikoff, I. S. *Mathematical Theory of Elasticity*. McGraw-Hill Book Company, Inc., 1946.

[23] Szabò, B. & Babuška, I. *Introduction to Finite Element Analysis. Formulation, Verification and Validation*. John Wiley & Sons, Ltd, 2011.

[24] Truesdell, C. & Noll, W. *The Non-Linear Field Theories of Mechanics*. 3rd ed. Springer, 2004.

[25] Welschinger, F. R. "A Variational Framework for Gradient-Extended Dissipative Continua. Application to Damage Mechanics, Fracture, and Plasticity". Dissertation. University of Stuttgart, 2011. URL: `http://elib.uni-stuttgart.de/bitstream/11682/371/1/diss_welschinger.pdf`.

[26] Zienkiewicz, O. C. & Taylor, R. L. *The Finite Element Method. Volume 1: The Basis*. 5th ed. Butterworth-Heinemann, 2000.